



ALMA MATER STUDIORUM
UNIVERSITÀ DEGLI STUDI DI BOLOGNA
Facoltà di Scienze Matematiche Fisiche e Naturali

Dottorato di Ricerca in Geofisica

XXII Ciclo

Settore scientifico disciplinare: GEO / 10

DEVELOPMENT OF THE OPTIMAL ESTIMATION
METHOD FOR INVERSION OF STRATOSPHERIC
EMISSION SPECTRA AND VALIDATION OF HNO₃
PROFILES

Dott.ssa Irene Fiorucci

Coordinatore:

Prof. Michele Dragoni

Relatore:

Dott. Cesidio Bianchi

2010

Contents

INTRODUCTION		1
CHAPTER 1	NITRIC ACID IN THE ATMOSPHERE	5
1.1	CLIMATOLOGY	5
1.2	SOURCE AND SINKS	9
1.2.1	GAS-PHASE REACTIONS	9
1.2.2	POLAR STRATOSPHERIC CLOUDS AND HETEROGENEOUS CHEMISTRY	10
1.3	EFFECTS ON OZONE DEPLETION	13
CHAPTER 2	GROUND-BASED MILLIMETER-WAVE SPECTROMETER HNO ₃ MEASUREMENTS	15
2.1	RADIATIVE TRANSFER AT MILLIMETER WAVELENGTH	17
2.2	OBSERVING SETUP	22
CHAPTER 3	OPTIMAL ESTIMATION METHOD FOR INVERSION OF MILLIMETER-WAVE EMISSION SPECTRA	26
3.1	THE OPTIMAL ESTIMATION METHOD: THEORETICAL BACKGROUND	27
3.2	HNO ₃ RETRIEVALS	31
3.2.1	FORWARD MODEL	31
3.2.2	A PRIORI PROFILE	32
3.2.3	COVARIANCE MATRICES	36

3.2.4	RETRIEVAL CHARACTERIZATION	42
3.2.5	COMPARISON BETWEEN OE AND MATRIX INVERSION TECHNIQUES	44
3.3	PRELIMINARY APPLICATION OF THE OE TO O ₃ AND N ₂ O SPECTRA	46
3.3.1	OZONE RETRIEVALS	47
3.3.2	NITROUS OXIDE RETRIEVALS	53
CHAPTER 4	COMPARISON OF HNO ₃ RETRIEVALS WITH SATELLITE MEASUREMENTS	57
4.1	MEASUREMENTS OF LOW AMOUNTS OF PRECIPITABLE WATER VAPOR BY MM-WAVE SPECTROSCOPY: AN INTERCOMPARISON WITH RADIOSONDE, RAMAN LIDAR AND FTIR DATA	60
4.2	COMPARISONS BETWEEN GBMS AND UARS MLS HNO ₃ RETRIEVALS (1993-1995)	110
4.3	COMPARISONS BETWEEN GBMS AND AURA MLS HNO ₃ RETRIEVALS	118
4.3.1	TESTA GRIGIA (2004-2007)	121
4.3.2	THULE (2008-2009)	124
4.4	UARS MLS – AURA MLS CROSS-CALIBRATION	126
	SUMMARY AND CONCLUSIONS	127
	APPENDIX A	131
	APPENDIX B	156
	BIBLIOGRAPHY	165

Introduction

This doctoral thesis focuses on ground-based measurements of stratospheric nitric acid (HNO_3) concentrations obtained by means of a microwave spectrometer. Pressure broadened HNO_3 emission spectra are analyzed using a new inversion algorithm developed as part of this thesis work and the retrieved vertical profiles are extensively compared to satellite-based data. This comparison effort I carried out has a key role in establishing a long-term (1991-2010), global data record of stratospheric HNO_3 , with an expected impact on studies concerning ozone decline and recovery.

Starting from the early 80's, microwave spectroscopy has been widely employed to study the extremely weak signals emitted from various atmospheric "trace gases" (as for instance O_3 , H_2O , CO , ClO , HNO_3) (*Parrish et al.*, 1987, 1992, , *de Zafra et al.*, 1987 *Solomon et al.*, 2000). Trace gases are present in the middle atmosphere with very low mixing ratio values (on the order of parts per billion to parts per million) but, despite of their low concentrations, they are of great interest in determining the chemical and physical conditions of the atmosphere. HNO_3 is one of these minor constituents and plays a pivotal role in the processes controlling stratospheric ozone depletion. It is a key component of the Polar Stratospheric Clouds (PSCs) which form in the very low temperatures of polar winter, removing HNO_3 from the gas phase and often subtracting it permanently from the stratosphere in a process known as denitrification. PSC particles provide surfaces on which heterogeneous chemical reactions occur, converting chlorine from its reservoir species to the highly reactive forms that participate in the catalytic cycles of ozone destruction. On the other hand, photolysis of HNO_3 vapor releases NO_2 , enabling a major pathway for the deactivation of chlorine. Therefore, as a central participant in both the activation and the deactivation of chlorine species, HNO_3 indirectly regulates the extent, duration, and magnitude of stratospheric ozone loss. As a result of international regulations controlling the production of ozone-depleting substances, the ozone layer is expected to recover back to preindustrial level in the next 60 years (*Newman et al.*, 2006). However potential changes in Earth's climate, driven by rising concentrations of greenhouse gases, may significantly influence the future ozone levels. Variations in the stratospheric circulation and temperature, including possible cooling and moistening, may increase the prevalence and duration of PSCs activity and

lead to more severe denitrification, exacerbating chemical ozone loss (WMO, 2007). Monitoring HNO_3 and its long term variability, especially in polar region, is then critical for better understanding these issues.

Nitric acid measurements presented in this study have been carried out by means of the Ground-Based Millimeter-wave Spectrometer (GBMS), built at the State University of New York at Stony Brook in the early 90's and operated in the past 20 years at a variety of sites at polar and mid-latitudes (*McDonald et al.*, 2000, *de Zafra and Muscari*, 2004, *Muscari et al.*, 2007). Its main characteristics and operating principles are described in Chapter 2 of this thesis. GBMS observes a cluster of weak emission lines centered at ~ 269.111 GHz, which appears as a single signature in the spectrometer pass band due to the pressure broadening of spectral lines. The frequency window sampled by GBMS for measuring HNO_3 contains also the signature of a background ozone line. Taking advantage of the pressure broadening of the observed lines, a deconvolution algorithm allows to retrieve concentration vertical profiles of the emitting molecules. Until recently, GBMS spectra were deconvolved using an iterative Matrix Inversion technique. This method can handle the inversion of multiple lines spectra, but the retrieval of spectra containing signatures of different atmospheric constituents is unfeasible. Thus, the ozone line observed as a background in the HNO_3 spectrum had to be subtracted from the measured data in a pre-processing phase, introducing a significant uncertainty in the whole retrieval process. For this and other reasons discussed in Chapter 3, I decided to investigate a different deconvolution algorithm, based on the Optimal Estimation Method. This technique, developed by *Rodgers* (1976, 2000), has been found to be useful for the analysis of spectra in which signatures of different atmospheric constituents significantly overlap (*Kuntz et al.*, 1999 and reference therein).

The first part of my thesis work is focused on the development of an *ad hoc* version of the OEM in order to retrieve HNO_3 spectra observed by means of GBMS. Many sensitivity tests were performed in order to extract the maximum information from the spectral measurements without introducing ambiguous oscillation in the retrievals. To further investigate capabilities and limits of the new method I also performed a comparison between HNO_3 vertical profiles retrieved with the OEM and those obtained with the old iterative Matrix Inversion method. A sample of this

comparison is presented in this thesis. Results show no significant differences in retrieved profiles and error estimates, with the OEM providing however additional information needed to better characterize the retrievals. A final section of Chapter 3 is dedicated to a brief review on the application of the OEM to other trace gases observed by GBMS, namely O_3 and N_2O , and further results are illustrated in a paper “*Evolution of temperature, O_3 , CO , and N_2O profiles during the exceptional 2009 Arctic major stratospheric warming as observed by lidar and mm-wave spectroscopy at Thule (76.5°N, 68.8°W), Greenland*” recently submitted to *Journal of Geophysical Research* and presented in Appendix A.

A validation of the HNO_3 profiles obtained with the new inversion method is then presented in Chapter 4. The first step is the validation of the tropospheric opacity τ_z which accounts for the fraction of the stratospheric radiation absorbed in troposphere before reaching the ground based instrument. In the 230 - 280 GHz spectral region sampled by GBMS the atmospheric opacity arises almost entirely from water vapor and the conversion from τ_z to the total amount of water vapor contained in the column of air (precipitable water vapor, or PWV) can be obtained by means of a simple linear relationship. An extensive validation of GBMS opacity measurements has therefore been obtained comparing the GBMS PWV with correlative measurements carried out by means of Vaisala RS92k radiosondes, a Raman Lidar and a Fourier Transform Infrared Spectroradiometer (FTIR) during the primary field campaign of the ECOWAR (Earth COoling by WAter vapour Radiation) project (Bhawar *et al.*, 2008). This intercomparison is presented in the paper: *Measurements of low amounts of precipitable water vapor by millimeter wave spectroscopy: An intercomparison with radiosonde, Raman lidar, and Fourier transform infrared data*, published on the *Journal of Geophysical Research*. Additional results obtained comparing GBMS and FTIR measurements are illustrated in the paper “*Water vapor sounding with the far infrared REFIR-PAD spectroradiometer from a high-altitude ground-based station during the ECOWAR campaign*”, submitted to *Atmospheric Chemistry and Physics* and presented in Appendix B. These two manuscripts show that GBMS PWV measurements are in good agreement with the other three data sets exhibiting a mean difference between observations of ~9%.

After this initial validation, GBMS HNO_3 retrievals have been compared to two

sets of satellite data produced by the two NASA/JPL Microwave Limb Sounder (MLS) experiments (aboard the Upper Atmosphere Research Satellite (UARS) from 1991 to 1999, and on the Earth Observing System (EOS) Aura mission from 2004 to date). This part of my thesis is inserted in GOZCARDS (Global Ozone Chemistry and Related Trace gas Data Records for the Stratosphere), a multi-year MEaSUREs project, aimed at developing a long-term data record of stratospheric constituents relevant to the issues of ozone decline and expected recovery. This data record will be based mainly on satellite-derived measurements but ground-based observations will be pivotal for assessing offsets between satellite data sets. Since the GBMS has been operated for more than 15 years, its nitric acid data record offers a unique opportunity for cross-calibrating HNO_3 measurements from the two MLS experiments. I compare GBMS HNO_3 measurements obtained from the Italian Alpine station of Testa Grigia (45.9°N , 7.7°E , elev. 3500 m), during the period February 2004 - March 2007, and from Thule Air Base, Greenland (76.5°N 68.8°W), during polar winter 2008/09, and Aura MLS observations. Since Aura is in a near polar orbit, co-located measurements are available for both these sites. A similar intercomparison is made between UARS MLS HNO_3 measurements with those carried out from the GBMS at South Pole, Antarctica (90°S), during the most part of 1993 and 1995. I assess systematic differences between GBMS and both UARS and Aura HNO_3 data sets at seven potential temperature levels. Results show that, except for measurements carried out at Thule, ground based and satellite data sets are consistent within the errors, at all potential temperature levels.

Chapter 1

Nitric Acid in the atmosphere

This research work is focused on measurements of nitric acid (HNO_3) in the stratosphere. Despite of its low concentration, HNO_3 is a very important constituent of the middle atmosphere being a major reservoir for nitrogen species (e.g., NO and NO_2), and playing a major role in processes that control stratospheric ozone depletion. Mixing ratio vertical profiles retrieved by ground-based measurements carried out in both hemispheres at polar and mid-latitudes, and correlative satellite observations, are presented. HNO_3 vertical profiles are characterized by a mixing ratio peak, whose altitude and intensity show a significant latitudinal and seasonal dependence. This chapter starts off introducing the HNO_3 concentration global distribution, as inferred from UARS MLS and Odin/SMR satellite observations (the longest and most comprehensive HNO_3 dataset available). The main sources and sinks of HNO_3 in the middle atmosphere are presented as well. Finally, the direct and indirect effects of HNO_3 variability on the stratospheric ozone loss process are illustrated.

1.1 Climatology

The first measurements of HNO_3 in the stratosphere were carried out by *Murcray et al.* (1968), and were followed by the first space-based measurements taken by the Limb Infrared Monitor of the Stratosphere (LIMS) on Nimbus 7 (*Gille and Russel*, 1984, *Gille et al.*, 1984). Quasi continuous observations of nitric acid mixing ratio vertical profiles, covering a full annual cycle in the Antarctic region, were obtained for the first time by means of the Ground Based Millimeter-wave Spectrometer in 1993 (*de Zafra et al.*, 1997, *McDonald et al.*, 2000, *Muscari et al.*, 2002). Since then, stratospheric nitric acid has been measured from the ground and from space by a variety of passive sensors,

operating at infrared and millimeter wavelengths. Until recently the longest data set is based on measurements made between 1991 and 1999 by the Microwave Limb Sounder (MLS) on the Upper Atmosphere Research Satellite (UARS) (Santee et al., 2004). In 2001, HNO_3 observations by means of two new space based instruments started: the advanced successor to the MLS experiment on UARS, aboard of the new EOS Aura satellite (Santee et al., 2007), and the Sub-Millimeter Radiometer (SMR) on the Odin satellite (Urban et al., 2009). MLS and SMR together provide a global data set from 1991 to 2009, with a short gap between 1999 and 2001, which gives comprehensive information on the global distribution and the variability of nitric acid in the stratosphere.

Above a given altitude layer, (upper troposphere or lower stratosphere, depending on the chemical species considered) the effect of surface sources and sinks on the concentration of trace gases is negligible, and this concentration is fully determined by chemical and dynamical processes. It is then convenient to introduce spatial coordinates that account for the vertical stratification and the horizontal dynamics of the atmosphere. The vertical coordinate chosen is the potential temperature, that is the temperature a given air parcel would have if adiabatically moved to sea level altitude. Surfaces where the potential temperature has the same value are called isentropic surfaces, because an air parcel can move along them without spending energy.

The main dynamical feature determining meridional trace gas distributions in the stratosphere is the formation of polar vortices. These are strong cyclonic circulations centered around both polar regions, which extend from the middle troposphere to the stratosphere, and are stronger in polar winter. Because of the high pressure gradients and high wind velocities, vortex air is prevented from mixing with air outside the vortex. This leads to a strong difference in atmospheric composition between air masses inside and outside the vortex. This leads to the definition of a dynamical horizontal coordinate, called equivalent latitude, that accounts for the penetration of airmasses in and out of the vortex. According to *Lary et al.* (1995), potential latitude is “the latitude of a latitude circle which encloses the same area as the potential-vorticity (PV) contour”, where PV is a dynamical conserved quantity expressing the distance from the edge of the vortex.

HNO_3 exhibits little vertical, seasonal and interannual variability at the tropics.

Mixing ratio values increase from low to high equivalent latitudes throughout the lower and the middle stratosphere. A pronounced seasonal cycle is present at middle and high equivalent latitudes in both hemispheres, with a winter maximum and a summer minimum, as expected from gas-phase chemistry (e.g. *Austin et al.*, 1986; *Santee et al.*, 2004). Large interannual variability in the timing, magnitude, and duration of enhanced wintertime HNO₃ abundances is seen in both hemispheres, and the variability increases with increasing equivalent latitude. The peak in the vertical profile occurs around 700–750 K potential temperature (~27–29 km) near the equator and moves steadily down in altitude to ~550 K (~23 km) in the vortex core in midwinter. Vortex mixing ratios near the peak are comparable in the two hemispheres. Above the peak, maximum abundances are larger in the Antarctic than in the Arctic, whereas below the peak maximum abundances are larger in the North. In the Southern Hemisphere, Polar Stratospheric Clouds formation and denitrification starts to reverse the seasonal increase in HNO₃ abundances in early winter, namely in May (for a discussion on PSC formation, see section 1.2.2.). Virtually complete removal of gas-phase HNO₃ occurs at the highest southern equivalent latitude by July in every year throughout the lower stratosphere. In contrast, even in the coldest Arctic winters, HNO₃ depletion is modest and more limited in both horizontal and vertical extent. Middle and upper stratospheric nitric acid enhancement, characterized by a considerable inter annual variability, is observed in midwinter. This high altitude HNO₃ rich air gradually descends during winter, eventually joining the main layer in the late winter

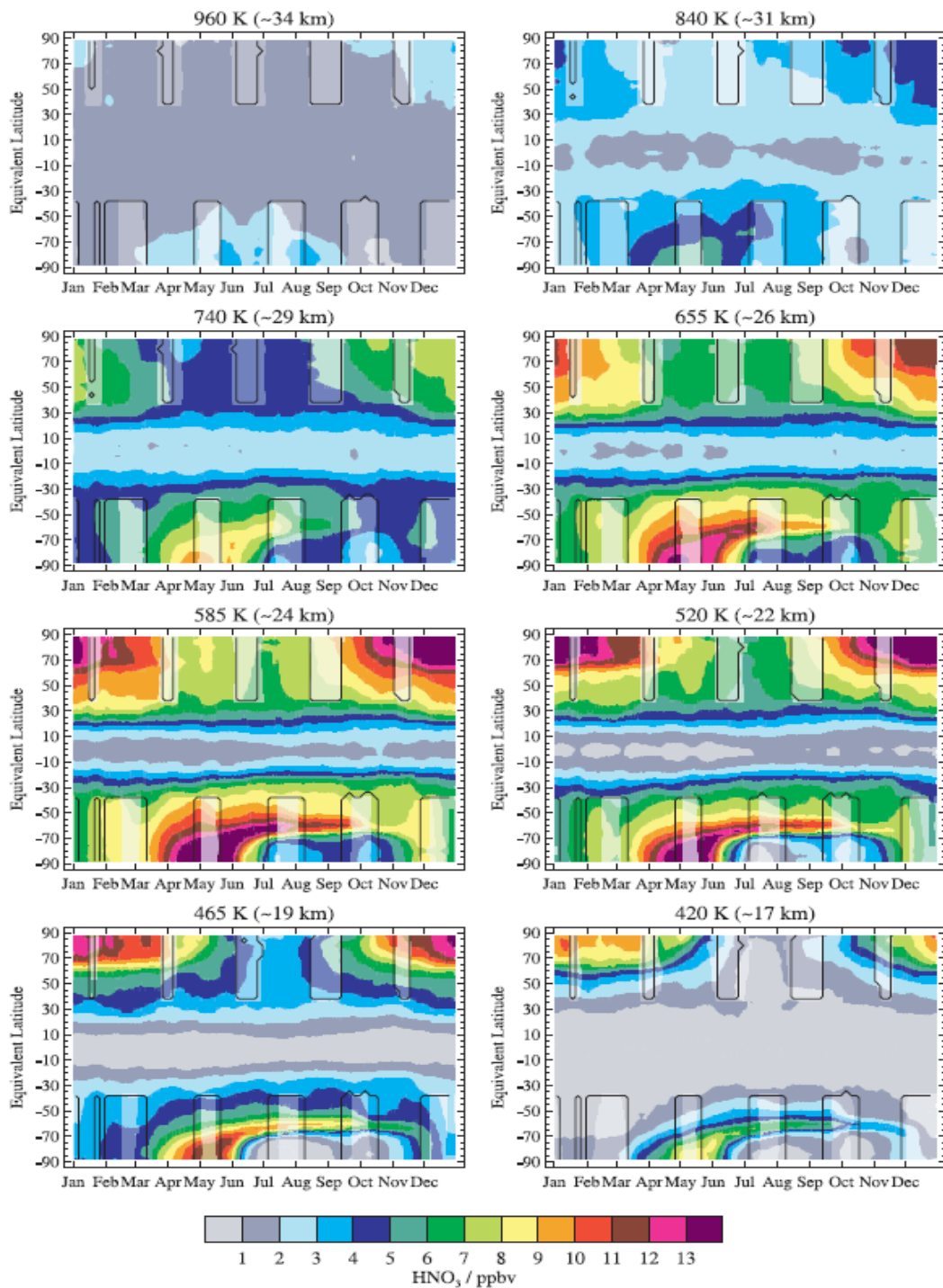


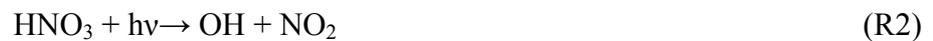
Figure 1.1 Seasonal evolution of the global distribution of UARS MLS HNO_3 as a function of equivalent Latitude at eight potential temperature levels between 960 and 420 K. Values are obtained by averaging together the results for seven individual years. Paler colors denote the regions in which the estimated precision of the interpolated values is poor. Overlaid in black are contours delimiting the regions in which data from fewer than three distinct years contributed to the averaged values. (from *Santee et al.*, 2004)

1.2 Source and sinks

chemistry that generates stratospheric HNO₃ can be divided into gas phases and heterogeneous reactions. The first take place at any latitude and their equilibrium alone determines the nitric acid concentration at low and mid-latitudes. The latter, instead, taking place on aerosol particles and ice crystals forming the so-called Polar Stratospheric Clouds (PSC), are relevant mostly in the polar stratosphere. The main features of polar stratospheric chemistry and the role of nitric acid in the ozone depletion mechanism will be outlined in section 1.2.2.

1.2.1 Gas-phase reactions

The main chemical source of nitric acid is the three-body gas-phase reaction while major sinks are photolysis



and the oxidation by OH:



(e.g. *Austin et al.*, 1986; *Brasseur et al.*, 1999).

Both processes make comparable contributions to HNO₃ loss in the lower stratosphere. Reaction R3 dominates the HNO₃ loss mechanism in the upper stratosphere (*Dessler*, 2000). During darkness, the highly reactive OH molecules is rapidly depleted, stopping reactions R1 and R3. Night of course also stops the photolytic destruction reaction R2. Thus, in the polar winter darkness, the lifetime of HNO₃ governed by gas phase reactions becomes extremely long (*Brasseur and Solomon*, 1984) and heterogeneous reactions become more important. Nitrogen species are heterogeneously converted to HNO₃ on background aerosol through a variety of less direct pathways. Conversion of NO and NO₂ to N₂O₅ takes place rapidly through the gas phase reactions:



followed by hydrolysis of N_2O_5 on water containing aerosols:



(*Garcia and Solomon, 1994; Santee et al., 1999; de Zafra and Smyshlyaev, 2001*). Therefore, a strong increase in the HNO_3 mixing ratio is observed to start shortly after polar sunset, as the photolytic chemistry stops, and to go on during fall and winter; in this period nitric acid represents almost 100% of NO_y at altitudes up to 23-25 km (*Garcia and Solomon, 1994; Schneider et al., 1999; Michelsen et al., 1999*)

1.2.2 Polar Stratospheric Clouds and heterogeneous chemistry

In the winter polar stratosphere, the liquid or solid surfaces needed for heterogeneous reactions to take place consist of polar stratospheric cloud (PSC) particles. PSC form between 20 and 30 km altitude, when temperatures are very low. At temperatures under 78°C , nitric acid can either freeze in a compound called NAT (Nitric Acid Trihydrate), resulting in solid aerosol particles (PSC type 1a), or coalesce in liquid form with water on sulphuric acid nuclei in supercooled ternary solution droplets (PSC type 1b). Both have a particle diameter around $1 \mu\text{m}$.

Type-2-PSC consist of pure crystals of frozen water, forming at even lower temperatures between -95°C and -90°C . Their diameter being about $10 \mu\text{m}$, they tend to sink down into the troposphere, leading to extended dehydration of the stratosphere.

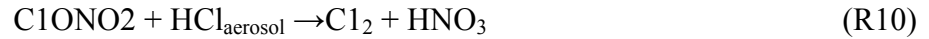
The chlorine disabling reaction is a relevant pathway leading to HNO_3 formation in the polar night:



followed by



or



[e.g. *Hanson et al.*, 1994; *Kondo et al.*, 1997]

Reactions R7, R9 and R10 take place on either sulfate aerosols or PSC particles. Sulfate aerosols provide an important pathway for the heterogeneous creation of HNO_3 in regions with temperatures above the Polar Stratospheric Clouds threshold. Reaction R7 is dominant, with a reaction probability of ~ 0.1 , at least an order of magnitude higher than the probability for reactions R9 and R10 at temperatures above approximately 200 K [Lefevre et al., 1994]. Reaction R8 is thought to be relatively insensitive to the composition of the aerosols, temperature and particle size, and will operate efficiently over the full range of conditions experienced in the polar stratosphere (*Rodriguez et al.*, 1991). Because of their inverse temperature dependence, reactions R9 and R10 will only contribute to HNO_3 production during the cold polar winter (*Hanson et al.*, 1994, and references therein). In particular, reaction R9 becomes important at temperatures below 200 K, as its reaction probability increases exponentially with decreasing temperature.

As soon as stratospheric temperatures reach a critical range, condensation of HNO_3 on PSC particles causes a rapid withdrawal of gas-phase HNO_3 from the polar stratosphere. Several studies (*McDonald et al.*, 2000, *Santee et al.*, 1998) suggest a condensation temperature close to 195K at ~ 20 km, indicating that the first PSCs to form are composed of ternary solutions of HNO_3 , H_2O and H_2SO_4 . After prolonged exposure to low temperatures nitric acid trihydrate or nitric acid dihydrate particles begin to nucleate, and a mixed cloud results. Meanwhile, a transfer of HNO_3 vapor from the ternary solution droplets to the more stable crystalline particles takes place, with eventual complete conversion. According to *Tabazadeh et al.* (1994a, 1995, 1996) this PSCs formation mechanism dominates if the preexisting sulfate aerosols are liquid. On the contrary, if the majority of the background aerosols are frozen, the growth of ternary solutions is inhibited and the initial formation of a metastable water-rich solid phase containing HNO_3 is promoted. In polar midwinter most lower stratospheric HNO_3 is incorporated into PSC particles and very little is left in the gas phase. In contrast to this scenario in the lower stratosphere, a rapid increase of HNO_3 mixing ratio is observed in

the middle and upper stratosphere (*Austin et al.*, 1986, *McDonald et al.*, 2000). Several mechanisms have been proposed to explain these high-altitude HNO₃ enhancements in the polar winter, which results in a second mixing ratio peak in the middle stratosphere. Gas phase reactions involving nitrogen species lead to the formation of N₂O₅, which is then converted into HNO₃ by heterogeneous reactions. The high altitudes preclude such reactions occurring on polar stratospheric clouds. Conversely *Kawa et al.* (1995) proposed that heterogeneous reactions on hydrated ion clusters could speed up the conversion of N₂O₅ into HNO₃. They concluded that the ion concentration needed to generate the second peak in HNO₃ was too large. *Bekki et al.* (1997) invoked heterogeneous chemistry on aerosol sulfate particles to explain the HNO₃ enhancements, but the sulfate aerosol layer extends only up to near 30–35 km. *de Zafra and Smyshlyaev* (2001) successfully modeled high-altitude mid-winter enhancements by combining these two mechanisms, with ion cluster chemistry playing a dominant role in the mid and upper stratosphere. Their study required a large, but not unrealistic, downward flux of NO_x from the polar winter mesosphere. Energetic particle precipitation is known to create NO_x in the mesosphere and thermosphere, and hence to strongly influence its flux into the upper stratosphere. First predicted by *Solomon et al.* (1982), observational evidence for stratospheric NO_x enhancements during and after periods of high geomagnetic activity has been extensively documented (e.g., *Callis and Lambeth*, 1998; *Randall et al.*, 2001; *Siskind et al.*, 2000, and references therein). More recently two studies by *Natarajan et al.* (2004) and *Orsolini et al.* (2005) have shown the link between the solar storm of 2003 and strong stratospheric NO_x enhancements observed during winter and spring 2004.

After the return of warmer temperature following the polar winter, HNO₃ incorporated into PSC aerosols which have not gravitationally settled out of the stratosphere return in the gas phase and are reduced by photolysis to other species in the family of NO_y. The enduring depression of HNO₃ abundance extensively observed in the Antarctic polar spring proves that a significant amount of nitric acid is irreversibly removed from the lower stratosphere through denitrification, and is not only temporarily sequestered in PSC particles (*Santee et al.*, 2004).

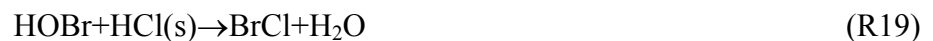
1.3 Effects on Ozone depletion

Nitric acid (HNO_3) plays several pivotal roles in the processes controlling stratospheric ozone depletion (Solomon et al., 1999, WMO 2003). It is a primary reservoir for reactive odd nitrogen which is responsible for the main catalytic cycle:



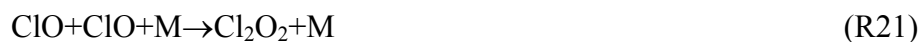
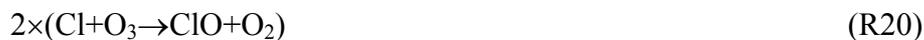
directly depleting ozone in the middle stratosphere (Brasseur and Solomon, 1984).

HNO_3 is also a major player in both the activation and the deactivation of chlorine and bromine species and thus indirectly regulates the extent and the duration of ozone loss. As seen in section 1.1, the presence of HNO_3 in polar regions promotes the formation of PSC particles through co-condensation with H_2O on sulfate aerosols. Heterogeneous reactions, taking place on the surface of these particles, convert chlorine and bromine from the reservoir species ClONO_2 , BrONO_2 and HCl , which are typically the dominant forms in the lower stratosphere, to the reactive species Cl_2 , HOCl , ClNO_2 , HOBr , and BrCl during the winter darkness. Such heterogeneous reactions are



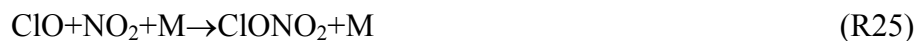
When sunlight returns to the polar regions, Cl_2 , HOCl , ClNO_2 , HOBr , and BrCl are

rapidly photolysed to produce Cl and Br, which deplete O₃ primarily through the ClO dimer cycle [Molina and Molina, 1987]:



and the analogous BrO cycle.

On the other hand, photolysis of HNO₃ vapor releases NO₂ enabling a major pathway for the deactivation of chlorine and bromine via the reformation of ClONO₂ and BrONO₂ through reactions:



Thus, when denitrification takes place during winter, little NO₂ can be produced after sunrise by photolysis of HNO₃, causing a delay in the deactivation of chlorine and bromine through R25, R26 and leading to extended ozone depletion.

Chapter 2

Ground-Based Millimeter-Wave

Spectrometer HNO₃ measurements

The most important data sets used in this thesis are HNO₃ mixing ratio vertical profiles obtained by means of the Ground-Based Millimeter-wave Spectrometer (GBMS). The GBMS was designed and built at the Physics and Astronomy Department of the State University of New York at Stony Brook, in the early 90's, and has been regularly upgraded and operated at polar and mid-latitudes since then. It allows the retrieval of mixing ratio vertical profiles of stratospheric and mesospheric trace gases (O₃, HNO₃, N₂O, CO, HCN and HDO) by measuring their emission spectra between 230 and 280 GHz, with a pass band of 600 MHz and a resolution of ~1 MHz.

Emission of radiation in the millimeter-wave range corresponds to transitions between rotational energy levels of molecules. When a molecule undergoes a transition between two discrete energy states, E_1 and E_2 , a photon is emitted or absorbed at the frequency $\nu = \frac{(E_2 - E_1)}{h}$, where h is Planck's constant. Since molecular transitions involve discrete energies, each emission line indicates a specific transition of a specific molecule. The discrete emission lines are broadened by different processes. The first one is the natural broadening, due to the Heisenberg uncertainty principle, which can be neglected in the microwave frequency region. The second broadening process is the Doppler broadening, accounting for the movement of the molecules relative to the observer and hence for the Doppler shift of the emitted radiation. The third and most important broadening mechanism in respect to microwave remote sensing is the pressure broadening, due to collisions of the emitting molecule with air molecules. As the pressure decreases exponentially with height, the pressure broadening is altitude

dependent and the measured spectrum allows to retrieve information on the vertical distribution of the emitting species (*Janssen, 1993*). Therefore, measurements of atmospheric constituents vertical profiles are possible up to altitudes where the pressure broadening is dominant respect to the Doppler broadening.

HNO₃ has a complex millimeter-wave spectrum, characterized by a large number of relatively weak rotational lines, hard to detect individually. The strongest emission lines are enclosed in the frequency range 269.172 - 269.452 GHz, and are all within 30 to 100 MHz from one another. The Ground-Based Millimeter-Wave Spectrometer (GBMS) observes a cluster of lines centered at 269.211 GHz which appears as a single signature in the spectrometer pass band, due to the pressure broadening. In the spectral window sampled by GBMS for measuring HNO₃ also the signature of a background ozone line is observed. Figure 2.1 shows two HNO₃ representative spectra measured from the GBMS at South Pole in 1993. The blue line is a typical spectrum observed during fall, when the highest concentrations of Nitric Acid are recorded. The green spectrum is measured during polar winter, when HNO₃ has been significantly depleted from the lower stratosphere and, at the same time, replenished at higher altitudes through descent from the upper stratosphere. As result of these processes the pressure broadening of each emission line is strongly reduced and single emission lines become visible in the second spectrum. The individual line positions are indicated in white.

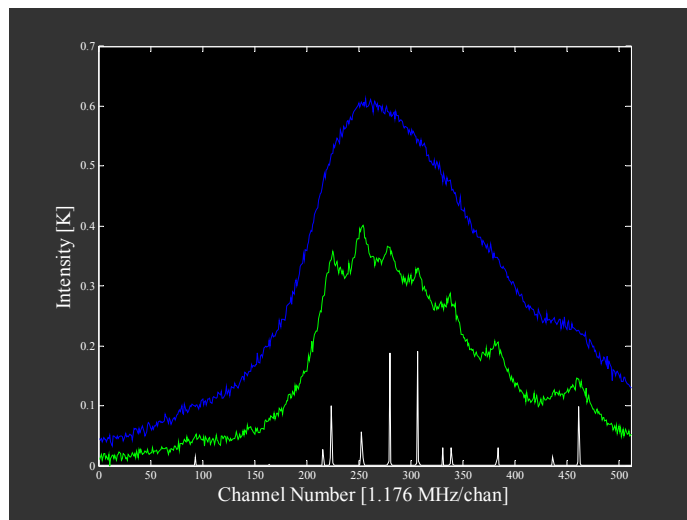


Figure 2.1 Two sample HNO₃ spectra recorded by means of the GBMS at South Pole, in 1993. Individual lines position is indicated in white. See text for details.

2.1 Radiative transfer at millimeter wavelength

The equation of radiative transfer for the nonscattering, nonrefractive atmosphere in thermal equilibrium between a point $z = z_0$ and another point $z = z_{obs}$, where a ground-based instrument could be located, is given by (Chandrasekhar, 1960):

$$I_\nu(z_{obs}) = I_\nu(z_0)e^{-\tau_\nu(z_0, z_{obs})} + \int_{z_0}^{z_{obs}} B_\nu(T)\kappa(\nu, z')e^{-\tau_\nu(z', z_{obs})} dz' \quad (2.1)$$

where $I_\nu(z_{obs})$ is the intensity of radiation at frequency ν measured at $z = z_{obs}$, $B_\nu(T)$ is the Planck function for a blackbody at temperature T , $\kappa(\nu, z)$ is the absorption coefficient per unit length, and $\tau_\nu(z, z_{obs})$ is the optical depth between z and z_{obs} . The optical depth represents the total absorption experienced by the signal before reaching the observing instrument, due to the presence of the atmospheric layer between z_0 and z_{obs} :

$$\tau_\nu(z, z_{obs}) = \int_z^{z_{obs}} \kappa(\nu, z') dz' \quad (2.2)$$

The first term on the right side of equation (2.1) can be interpreted as the attenuation of the background radiation by the factor $e^{-\tau_\nu(z_0, z_{obs})}$ and for emission lines with no background radiation present the term is neglected.

At stratospheric temperatures and for millimeter wavelengths, the Rayleigh-Jeans limit, $h\nu \ll kT$, is valid and the Planck function for a blackbody at temperature T simplifies to:

$$B_\nu(T) = \frac{2k\nu^2 T}{c^2} \quad (2.3)$$

where k is Boltzman's constant and c the speed of light. Thus, the intensity of a stratospheric spectral line can be expressed in units of brightness temperature, defined by:

$$T^*(\nu, z_{obs}) = \int_{z_{obs}}^{z_{max}} T(z) \kappa(\nu, z) e^{-\tau_{\nu}(z_{obs}, z)} dz \quad (2.4)$$

where the limits of integration have been reversed, so as to go from the ground (z_{obs}) to the maximum altitude of emission (z_{max}).

The absorption coefficient $\kappa(\nu, z)$ is the sum of the coefficients κ_{lm} relative to all the possible transitions in the frequency range observed by the GBMS, l and m being two generic states. Each coefficient is given by (Gordy and Cook, 1970):

$$k_{lm}(\nu, z) = \frac{8\pi^3\nu}{3hc} f_l [1 - \exp(-h\nu_{lm}/kT)] |\mu_{lm}|^2 \rho(z) f(\nu, \nu_{lm}) \quad (2.5)$$

where f_l is the fraction of molecules in the lower energy state, μ_{lm} is the total dipole moment matrix element for the transition, $\rho(z)$ is the number density of the emitting or absorbing molecule, ν_{lm} is the frequency of the transition and $f(\nu, \nu_{lm})$ is the line shape function. The molecular fraction f_l is given by:

$$f_l = g_l e^{E_l/kT} / Q \quad (2.6)$$

where

$$Q = \sum_j g_j e^{-E_j/kT} \quad (2.7)$$

is the partition function and g_l is the degeneracy of the lower state. The term f_l can be conveniently expressed as the product of the fraction of molecules in rotational, spin, vibrational and electronic states:

$$f_l = f_{rot} f_{spin} f_{vib} f_{elec} \quad (2.8)$$

Incorporating explicitly the fraction for rotational and spin states into equation (2.5) results in:

$$k_{lm}(\nu, z) = \frac{8\pi^3\nu}{3hcQ_{rs}} g_{rs} \left[e^{-E_l/kT} - e^{-E_m/kT} \right] f_{vib} f_{elec} |\mu_{lm}|^2 \rho(z) f(\nu, \nu_{lm}) \quad (2.9)$$

Where Q_{rs} is the combined rotational and spin partition function, g_{rs} is the degeneracy of the lower rotation-spin energy state and E_l , E_m are the lower and upper state rotational energies. Integrated line intensities $I_{lm}(T_0)$, for $T_0=300$ K are given in the Jet Propulsion Laboratory (JPL) catalog (available at <http://spec.jpl.nasa.gov>) (Petkie *et al.*, 2003):

$$I_{lm}(T_0) = \frac{8\pi^3 {}^x S_{lm} \mu_x^2 \nu_{lm}}{3hc Q_{rs}} \left[e^{-E_l/kT_0} - e^{-E_m/kT_0} \right] \quad (2.10)$$

where ${}^x S_{lm}$ is the line strength and μ_x^2 is the projection of the molecular dipole on the molecular radiation field.

For determining the line intensity at other temperatures, the temperature dependence of the rotation-spin partition function can be well approximated by:

$$Q_{rs} \propto T^{3/2} \quad (2.11)$$

Thus the line intensity at any temperature is obtained from the JPL catalog according to:

$$I_{lm}(T) = I_{lm}(T_0) \frac{Q_{rs}(T_0) \left[e^{-E_l/kT_0} - e^{-E_m/kT_0} \right]}{Q_{rs}(T) \left[e^{-E_l/kT} - e^{-E_m/kT} \right]} \quad (2.12)$$

For many molecules emitting in the millimeter-wave region, included HNO₃, only the ground state is populated at stratospheric temperatures, transitions are purely rotational and f_{vib} and f_{elec} can be approximated to 1.

Thus the total absorption coefficient in term of the JPL catalog line intensities can be written:

$$k_{lm}(\nu, z) = I_{lm}(T) \rho(z) f(\nu, \nu_{lm}) \quad (2.13)$$

The line shape function $f(\nu, \nu_{lm})$ accounts for the broadening of the line and looks different depending on the underlying broadening process. The pressure-broadened line shape can be well approximated by a Lorentzian:

$$f(\nu, \nu_{lm}) = \frac{\Delta \nu_c}{\pi(\nu - \nu_{lm})^2 + \Delta \nu_c^2} \quad (2.14)$$

The pressure-broadened half-width, $\Delta \nu_c$, is given by:

$$\Delta \nu_c = \gamma(T_0) \left[\frac{P(z)}{P_0} \right] \left[\frac{T_0}{T(z)} \right]^\chi \quad (2.15)$$

where the pressure broadening coefficient at the reference temperature, $\gamma(T_0)$, is expressed in MHz/mbar, and the temperature exponent χ is an adimensional coefficient.

As pressure decreases with altitude, the pressure broadening becomes less important and the Doppler broadening begins to dominate the line shape. The Doppler half width is given by

$$\Delta \nu_D = \frac{\nu_{lm}}{c} \sqrt{\frac{2kT}{m} \ln 2} \quad (2.16)$$

where m is the mass of the molecule. Note that the Doppler line width doesn't depend on the pressure and is proportional to the frequency. Hence, the observation of lines at lower frequencies allows generally to reach higher altitudes. For the observed HNO₃ lines the Doppler broadening starts to dominate on the pressure broadening at around 50-60 km, and these altitudes are therefore close to the upper limit for the retrieval of vertical profile.

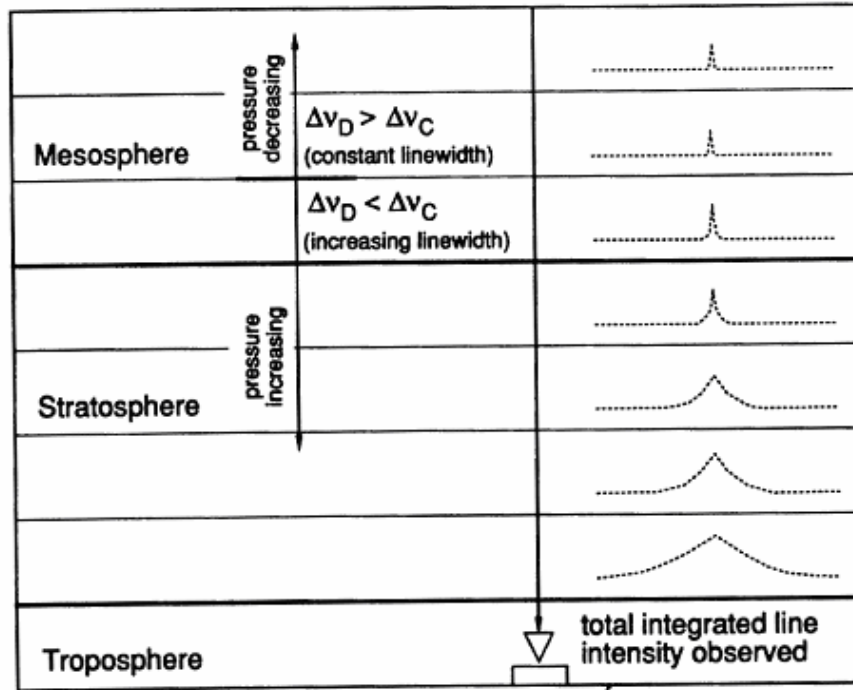


Figure 2.2 Line shapes due to emission from different altitudes. In the stratosphere and lower mesosphere the pressure broadening is dominant ($\Delta v_c > \Delta v_D$) and the line width decrease with altitudes. When pressure broadening becomes negligible with respect to Doppler broadening ($\Delta v_c \ll \Delta v_D$) the line width doesn't depend on atmospheric pressure anymore.

2.2 Observing setup

The GBMS is a high sensitivity cryogenically cooled heterodyne receiver, followed by a back-end spectrometer. For the measurement made in 1993 and 1995 filter banks were used, later replaced by an Acousto-Optical Spectrometer (AOS). The receiver converts millimeter wave signals, arising from molecular rotational transitions, to lower «Intermediate» Frequencies (IF) by mixing them with the signal emitted from a local oscillator. The mixing occurs by means of a SIS (Superconductor-Insulator-Superconductor) tunnel junction double side band mixer. The IF output contains all the spectral information of the incoming signal but is shifted to much lower frequencies where it can be amplified. This output is then sent to the filter banks, or to the AOS, which produce the intensity vs. frequency spectrum that is eventually analyzed. Both the filter banks and the Acousto-Optical Spectrometer have 512 read-out channels, with a resolution of 1 MHz and 1.2 MHz, respectively.

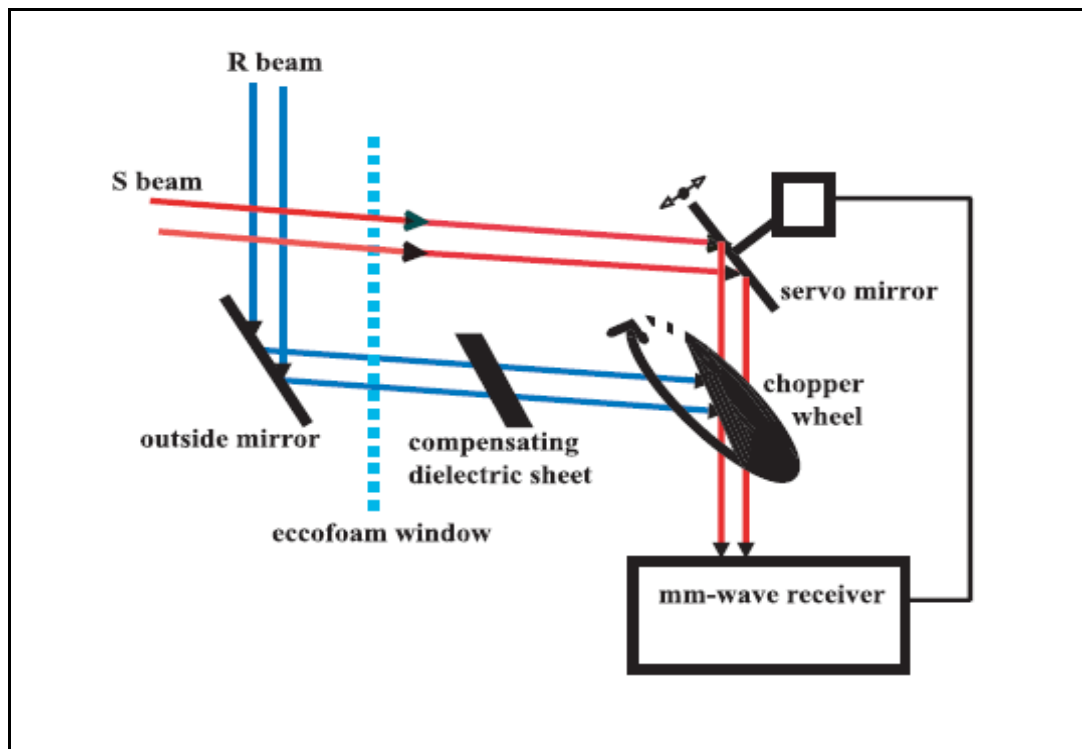


Figure 2.3 Schematic diagram of the GBMS front end . See text for details.

A schematic diagram of the observing setup is shown in Figure 2.3. During normal data taking operations the GBMS observes radiation from two different directions, switched by a rotating reflective semicircular chopper wheel at ~1 Hz frequency. This technique of beam-switching allows a small atmospheric signal to be recovered from large background temperatures. One observing direction is near the zenith (reference beam, or R) while the other points between 10° and 15° above the horizon (signal beam, or S). Since the signal beam travels a longer path through the lower atmosphere, it will have a greater emission intensity than the reference. A dielectric sheet made of Plexiglas (weakly emitting at millimeter wavelength) is placed in the R beam to balance the power between the two signals. This power balance is maintained by a servo mechanism which adjusts the elevation angle of the signal beam if the (S-R) power level deviates from zero, as atmospheric conditions change. Atmospheric radiation from both beam directions enters through a window made of Eccofoam, characterized by a very small opacity at millimeter wavelengths. The total power (expressed in temperature units) observed in the S direction at the frequency ν is expressed by:

$$T_s(\nu) = T_z^*(\nu)A'_s e^{-A_s \tau_z} e^{-\tau_w} + 2T_{atm}(1 - e^{-A_s \tau_z})e^{-\tau_w} + 2T_w(1 - e^{-\tau_w}) + T_{rec}(\nu) \quad (2.17)$$

where A'_s , and A_s are the stratospheric and tropospheric air mass factors for signal direction, $T_z^*(\nu)$ is the stratospheric emission signal of interest in the zenith direction (which we assume can be transformed to the molecular emission along any other line of sight by multiplying by A_x , i.e., we assume the atmospheric homogeneity), τ_z is the opacity of the atmosphere in the zenith direction (which, again, we assume can be transformed to the opacity along any other line of sight by multiplying by A_x). $T_{rec}(\nu)$ is the receiver noise, and T_w and τ_w are the physical temperature and opacity of the window material, respectively. T_{atm} is the mean physical temperature of the noise-radiating atmosphere, typically that of the first few km within the troposphere containing most of the water vapor. In this equation, terms involving $exp(-\tau_x)$ represent attenuation of signal by some entity along the path whose total opacity is τ_x , while terms involving $T_x(1 - exp(-\tau_x))$ represent emission by the same entity, assumed to be at a mean physical temperature T_x . An expression similar to equation (2.17) gives the output power from the R direction

$$T_r(\nu) = T_z^*(\nu) A_r' e^{-A_r \tau_z} e^{-\tau_w} e^{-\tau_p} + 2T_{atm} (1 - e^{-A_r \tau_z}) e^{-\tau_w} e^{-\tau_p} + 2T_w (1 - e^{-\tau_w}) e^{-\tau_p} + 2T_p (1 - e^{-\tau_p}) e^{-\tau_p} + T_{rec}(\nu) \quad (2.18)$$

where terms have been added to represent signal attenuation by the compensating sheet and its broadband emission for a given opacity τ_p and physical temperature T_p .

The air mass factors are the ratio between the slant path and the zenith path at a particular altitude. Assuming a plane-parallel atmosphere for the tropospheric air mass factors, we have $A_s = A_r \sim 1/\sin\theta$. For the stratospheric air mass factor A' instead, the plane-parallel approximation is not sufficient, and in either beam we have:

$$A' = \frac{R_e + Z_{source}}{\sqrt{(R_e + Z_{source})^2 - (R_e + Z_{obs})^2 \cos^2 \theta}}, \quad (2.19)$$

where R_e is the radius of the earth, Z_{source} is the altitude of the emitting molecules, Z_{obs} is the altitude of the observer, and θ is the observing angle of the beam. In the reference beam, θ is typically 90° , so this factor is 1.

At power balance, the frequency averaged emission intensities for signal and reference directions are equal: $\bar{T}_s = \bar{T}_R$. Since terms due to molecular emission from stratospheric trace gases (those involving T_z^*) are negligible compared to other terms, we have:

$$T_{atm} (1 - e^{-A_s \tau_z}) e^{-\tau_w} + T_w (1 - e^{-\tau_w}) \approx T_{atm} (1 - e^{-A_r \tau_z}) e^{-\tau_w} e^{-\tau_p} + T_w (1 - e^{-\tau_w}) e^{-\tau_p} + T_p (1 - e^{-\tau_p}) \quad (2.20)$$

Thus the observed signal, given by the difference between the signal and the reference beams normalized by the reference signal, can be written as:

$$\frac{T_s(\nu) - T_r(\nu)}{T_r(\nu)} = \frac{T_z^*(\nu) \left(A_s' e^{-A_s \tau_z} - A_r' e^{-A_r \tau_z - \tau_p} \right) e^{-\tau_w}}{2T_{atm} (1 - e^{-A_s \tau_z}) e^{-\tau_w} + 2T_w (1 - e^{-\tau_w}) + T_{rec}(\nu)} \quad (2.21)$$

Equation (2.21) can be rearranged to obtain T_z^* explicitly:

$$T_z^*(\nu) = SF(\nu) \times \frac{T_s(\nu) - T_r(\nu)}{T_r(\nu)}, \quad (2.22)$$

with the scale factor SF(ν) given by:

$$SF(\nu) = \frac{2T_{\text{atm}}(1 - e^{-A_s \tau_z})e^{-\tau_w} + 2T_w(1 - e^{-\tau_w}) + T_{\text{rec}}(\nu)}{(A'_s e^{-A_s \tau_z} - A'_r e^{-A_r \tau_z - \tau_p})e^{-\tau_w}} \quad (2.23)$$

The result of scaling by SF(ν) is to compensate for geometrical path length in the actual observing direction, receiver sensitivity, and time-varying tropospheric attenuation. In the retrieval process of some atmospheric trace gases (e.g., ozone), SF(ν) needs to be corrected to take into account self absorption (absorption by molecules of the same species as emission signals pass through the stratosphere), but for HNO₃ this effect is negligible. A detailed discussion on the calibration of the receiver using hot and cold temperature loads to derive the values needed to calculate the scale factor is given by *de Zafrá* (1995) and Parrish et al.(1988).

Chapter 3

Optimal Estimation Method for inversion of millimeter-wave emission spectra

For the retrieval of HNO_3 profiles considered in this study an *ad hoc* version of the Optimal Estimation Method (OEM) has been developed. The OEM is a generic algorithm, formulated by *Rodgers* (1976, 2000), for solving atmospheric inversion problems, that is inverting a known equation which express radiation as a function of the atmospheric state. This type of problem is usually under-constrained and so the solution space contains many possible outcomes. The OEM uses an a priori profile to constrain this space. One of the main advantage of this technique is that no assumptions are made about the nature of state vector; it may contain altitude profiles of different atmospheric constituents, as any set of instrumental and atmospheric parameters (*Kuntz et al.*, 1999). As seen in Chapter 2, the spectral window sampled by GBMS for measuring HNO_3 contains also the signature of a background ozone line. In our implementation we consider both the HNO_3 and the O_3 profile as quantities to be retrieved.

The Optimal Estimation Method is discussed in great detail by *Rodgers* (1976, 1990, 2000) and will be illustrated only briefly in the first section of this chapter. The adaptation of the general theory to GBMS measurements will be presented here, with particular emphasis on the parameter selection and the retrieval characterization. A sample comparison of HNO_3 vertical profiles retrieved with the OEM and with an

iterative matrix inversion method (used in the past for GBMS HNO₃ retrievals) will be also shown. The last section of this chapter is dedicated to a brief review on the application of the OEM to other trace gases observed by GBMS.

3.1 The Optimal estimation Method: theoretical background

In any atmospheric remote measurements, the measured quantity, \mathbf{y} , is a vector valued function \mathbf{F} of the unknown state of the atmosphere \mathbf{x} and of a set of additional parameters \mathbf{b} . The relationship between the measurement vector and the state vector can be expressed as:

$$\mathbf{y} = \mathbf{F}(\mathbf{x}, \mathbf{b}) + \boldsymbol{\varepsilon} \quad (3.1)$$

where $\mathbf{F}(\mathbf{x})$ is the Forward model, describing the complete physics of the problem, and $\boldsymbol{\varepsilon}$ represents the measurement noise.

Equation (3.1) can be re-formulated into a simplified form by linearizing the forward model about some reference state \mathbf{x}_0 :

$$\mathbf{y} - \mathbf{F}(\mathbf{x}_0) = \frac{\partial \mathbf{F}(\mathbf{x})}{\partial \mathbf{x}} (\mathbf{x} - \mathbf{x}_0) + \boldsymbol{\varepsilon} = \mathbf{K}(\mathbf{x} - \mathbf{x}_0) + \boldsymbol{\varepsilon} \quad (3.2)$$

\mathbf{K} is the Weighting Function matrix in which each element is the partial derivative of a Forward Model element with respect to a state vector element:

$$K_{i,j} = \frac{\partial F_i(x)}{\partial x_j} \quad (3.3)$$

Each row of \mathbf{K} corresponds to a different measurement and the elements along the row represent the sensitivity of each measurement to the different profile elements.

Neglecting the noise term, equation (3.2) is well-determined only if the Weighting Function matrix is square and if it has maximum rank. In real atmospheric problems it doesn't happen very often. Moreover, because of the noise present in all physical measurements, there is a nonuniqueness in the observation which leads to a

nonuniqueness in the solution. Some a priori information are necessary to constrain the solution. The approach used in the OEM is combining the measurements vector and the a priori profile information together, with weights given from the respective inverse covariances. In practice any a priori information can be regarded as a “virtual measurement”, providing an estimate of the state vector \mathbf{x}_a , with covariance \mathbf{S}_a . As long as the problem is linear, $\mathbf{x}=\mathbf{K}^{-1}\mathbf{y}$ provides another estimate of \mathbf{x} . If the measurement vector \mathbf{y} has a covariance matrix \mathbf{S}_ϵ , than the inverse covariance of this second estimate of \mathbf{x} is given by $\mathbf{K}^T\mathbf{S}_\epsilon^{-1}\mathbf{K}$. So combining these independent information, coming from “actual” and “virtual” measurements, we obtain an estimate of \mathbf{x} :

$$\hat{\mathbf{x}} = \frac{\mathbf{S}_a^{-1}\mathbf{x}_a + \mathbf{K}^T\mathbf{S}_\epsilon^{-1}\mathbf{y}}{\mathbf{S}_a^{-1} + \mathbf{K}^T\mathbf{S}_\epsilon^{-1}\mathbf{K}} \quad (3.4)$$

with covariance:

$$\hat{\mathbf{S}} = (\mathbf{S}_a^{-1} + \mathbf{K}^T\mathbf{S}_\epsilon^{-1}\mathbf{K})^{-1} \quad (3.5)$$

The diagonal elements of \mathbf{S}_a and \mathbf{S}_ϵ (designated with σ_a^2 and σ_ϵ^2) are the variances of the single elements of the a priori profile and of the measurement vector, respectively. The-off diagonal elements contain information about the cross-correlation between the different elements of the vector. If they are nonzero a correlation exists and we can have more information about the vector than is the case if the off-diagonal elements are negligible.

Given equation (3.4) we can calculate the sensitivity of the retrieved profile $\hat{\mathbf{x}}$ to changes in the measurement \mathbf{y} :

$$\frac{\partial \hat{\mathbf{x}}}{\partial \mathbf{y}} = \mathbf{G} = \mathbf{S}_a \mathbf{K}^T (\mathbf{K} \mathbf{S}_a \mathbf{K}^T + \mathbf{S}_\epsilon)^{-1} \quad (3.6)$$

and the sensitivity of the retrieval $\hat{\mathbf{x}}$ to changes in the true profile \mathbf{x} :

$$\frac{\partial \hat{\mathbf{x}}}{\partial \mathbf{x}} = \mathbf{G} \mathbf{K} = \mathbf{A} \quad (3.7)$$

The last quantity, known as the Averaging Kernels matrix, is a key quantity in the characterization of the retrieval process, providing pivotal information about the

resolution and the altitude range in which the retrieved profile is sensitive to the true profile.

Using the matrices defined in equation (3.6) and (3.7), the retrieval solution can be rewritten in the following form:

$$\hat{\mathbf{x}} = \mathbf{x}_a + \mathbf{GK}(\mathbf{x} - \mathbf{x}_a) = \mathbf{x}_a + \mathbf{A}(\mathbf{x} - \mathbf{x}_a) \quad (3.8)$$

This expression shows that the retrieved profile at a given altitude can be expressed as the sum of the a priori value at the corresponding altitude and the deviation of the true profile from the a priori profile, smoothed with the associated row of the Averaging Kernels matrix. For an ideal observing system \mathbf{A} is a unit matrix. In fact, the rows of \mathbf{A} are peaked functions with the full width at half maximum (FWHM) which is a measure of the vertical resolution of the retrieved profile. However, this definition of resolution is meaningful only if the kernels are well peaked and centered fairly closely on their nominal altitude. When the actual altitude of the kernels peaks starts to deviate from their nominal altitude, the retrieval is no longer sensitive to changes in the true profile and the main part of the information comes from the a priori rather than from the measurement.

The smoothing of the averaging kernels introduces an error, which accounts for the fact that fine vertical structure cannot be resolved in the retrieved profile. This error will be important in any comparison between measurements with different vertical resolutions and its magnitude can only be estimated if the statistical variability of the true atmospheric state is known. However, if the higher-resolution measurement profile \mathbf{x}_{hr} is smoothed with the lower-resolution measurement Averaging Kernels, \mathbf{A}_{lr} , this error has not to be considered in the comparison. According to equation (3.8) the smoothed (or convolved) profile is given by:

$$\hat{\mathbf{x}}_{conv} = \mathbf{x}_a + \mathbf{A}_{lr}(\mathbf{x}_{hr} - \mathbf{x}_a) \quad (3.9)$$

A further characterization of the retrieval method capability can be obtained, in a simple and fast way, performing an information content analysis. With Information Content I indicate in this case the degree of freedom for signals, D_s , which represents the number of unknown quantities that can be independently retrieved from the measurement:

$$D_s = \sum_{i=1}^m \frac{\lambda_i^2}{(1 + \lambda_i^2)} \quad (3.10)$$

where λ_i are the singular value of the matrix $\tilde{\mathbf{K}} = \mathbf{S}_\varepsilon^{-1/2} \mathbf{K} \mathbf{S}_a^{-1/2}$. If n is the dimension of the state vector, we have $D_s=n$ if the measurement completely determines the state, and $D_s=0$ if the measurement doesn't contain any information on the unknown state (*Corradini et al.*, 2005).

3.2 HNO₃ retrievals

3.2.1 Forward model

The radiative transfer model for millimeter-wave spectra observed by means of GBMS has been extensively described in Chapter 2 and can be summarized by the equation:

$$T_{z_{obs}}^*(\nu) = \int_{z_{obs}}^{\infty} K(\nu, z) \rho(z) dz \quad (3.11)$$

where

$$K(\nu, z) = \frac{1}{\mu} T(z) \alpha(\nu, z) e^{-\tau_{\nu}(z_{obs}, z)} \quad (3.12)$$

are the Weighting Functions.

For calculation of absorption coefficient of a single molecule $\alpha(\nu, z)$, spectroscopic data from the Jet propulsion Laboratory (JPL) catalog (available at <http://spec.jpl.nasa.gov>) (Petkie *et al.*, 2003) and pressure broadening coefficients from HITRAN2008 database (<http://www.cfa.harvard.edu/hitran>) (Rothman *et al.*, 2009) are employed; a Lorentzian line shape is used. Pressure and temperature vertical profiles are computed using data from the NCEP (National Center for Environmental Prediction) reanalysis

The term

$$\tau_{\nu}(z_{obs}, z) = \int_{z_{obs}}^z \alpha(\nu, z') \rho(z') dz' \quad (3.13)$$

represents the stratospheric signal self absorption and introduce a slight dependence of the Weighting Functions on the emitting species vertical distributions. In practice it is possible to neglect this dependence and consider a linear problem with the Weighting Functions evaluated at $\rho(z) = \rho_a(z)$. To check whether this approximation is adequate, a determination of the degree of nonlinearity of the problem has been performed. The

error due to nonlinearity, introduced on the retrieval solution using a linear approximation, is about (Rodgers, 2000):

$$\delta\hat{x} = G[F(\hat{x}) - F(x_a) - K(\hat{x} - x_a)] \quad (3.14)$$

In this implementation this error is ~1% of the retrieved profile and is therefore negligible.

3.2.2 A priori profile

In the classical formulation of the Optimal Estimation method developed by Rodgers the a priori profile represents the whole knowledge of the atmospheric state before the measurement is made.

As seen in Chapter 1 HNO₃ vertical profile is characterized by a single peak, which altitude and intensity shows a significant latitudinal and seasonal dependence. Near the equator the peak occurs at around 700-750 K of potential temperature (with mixing ratio values as low as 2-3 ppbv) and moves down in altitude to 550 K in the vortex core in midwinter (with values up to 15-20 ppbv) (Santee *et al.*, 2004). Moreover, a strong denitrification process is normally observed during the austral winter in the Antarctic vortex region. In this work HNO₃ measurements carried out at different sites, in both hemispheres, at polar and mid-latitudes, has been considered. Thus, following the approach suggested by Rodgers and considering the strong latitudinal and seasonal variability in the HNO₃ distribution, a different a priori profile should be used for the retrieval of each data set.

In order to determine the influence of the used a priori on the retrieved profile, retrieval tests have been performed. I have inverted three spectra measured at as many GBMS observing sites (South Pole, Thule, Greenland and Testa Grigia, on the Italian Alps) using concurrent measurements from the NASA JPL Microwave Limb Sounder (MLS) experiment as a priori profiles. For each inversion the contribution of the a priori to the *j*th altitude of the retrieved profile, has been estimated as $(\mathbf{I} - \mathbf{A})_j \mathbf{x}_a / \hat{\mathbf{x}}_j$, following Connor (2000). For a contribution of the a priori of 100% the retrieved profile contains only a priori information, for 0% no a priori information is stored in the retrieved profile. Results are shown in Figure 3.1

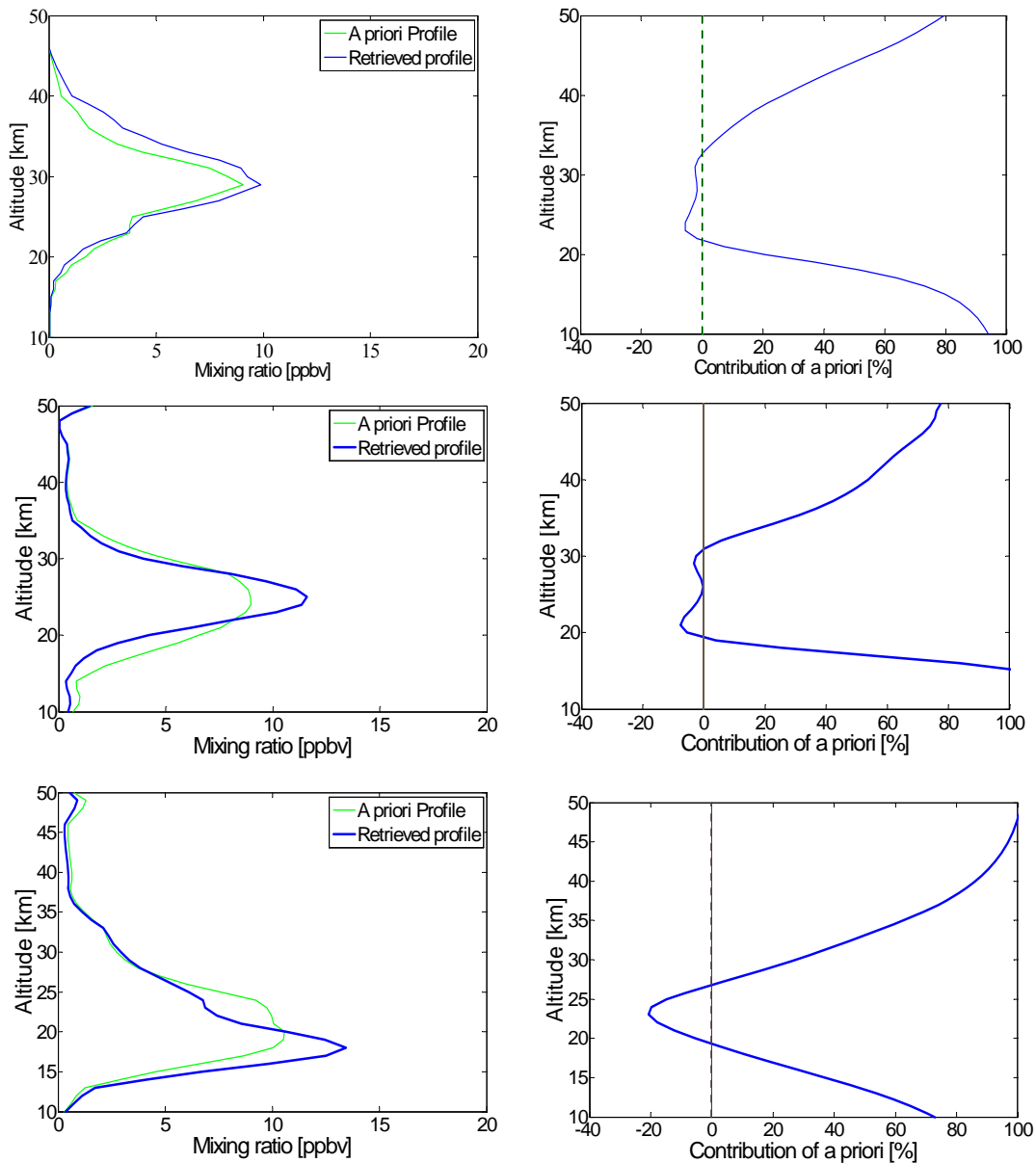


Figure 3.1 Retrieved profiles (left panels) and relative contribution of a priori profiles to the retrievals (right panels). Measurements carried out at South Pole (top panels), Testa Grigia (middle panels) and Thule (bottom panels).

Plots with the contribution of the a priori profile show that the choice of a particular a priori can have a strong influence on the retrieval performance. For the purpose of this work I am interested in having the same sensitivity in the analysis of the different data sets and this approach obviously doesn't satisfy this requirement. Thus I decided to consider alternative methods.

In some modified version of the Optimal Estimation technique (*Solomon et al., 2000, Coe et al., 2002*) the a priori profile is somewhat determined utilizing the data

themselves. In this approach the observed spectrum is retrieved using as a priori the result of a first inversion. The first inversion is performed using an a priori with very poor information on the real vertical distribution of the atmospheric constituent (for example a broad Gaussian). The inversion performed with this method presents the advantage of being independent from any other dataset but, on the other hand, it is equivalent to using the measurements more than once in the analysis. This is inappropriate since the a priori represents our knowledge of the state before the measurements are made and should not be replaced by something that is the result of using the measurements.

Another option consists of using a standard a priori profile, built *ad hoc* for the retrieval with some generic information on the shape of the vertical profile and on the altitude of the peak. This is the technique I eventually adopted because it proved to be the best suited for my goal, providing several advantages: the same a priori for all the different HNO₃ data sets, no dependence on other measurements or models, good sensitivity to the true profile. Therefore, I synthesized a Gaussian profile with a peak of 8 ppbv at 25 km. Then, this profile was modified introducing a “plateau” instead of the peak, in order to increase the retrieval sensitivity to the true profile peak altitude. The same GBMS spectra considered in the retrieval tests of Figure 3.1 were inverted using this standard a priori (Figure 3.2).

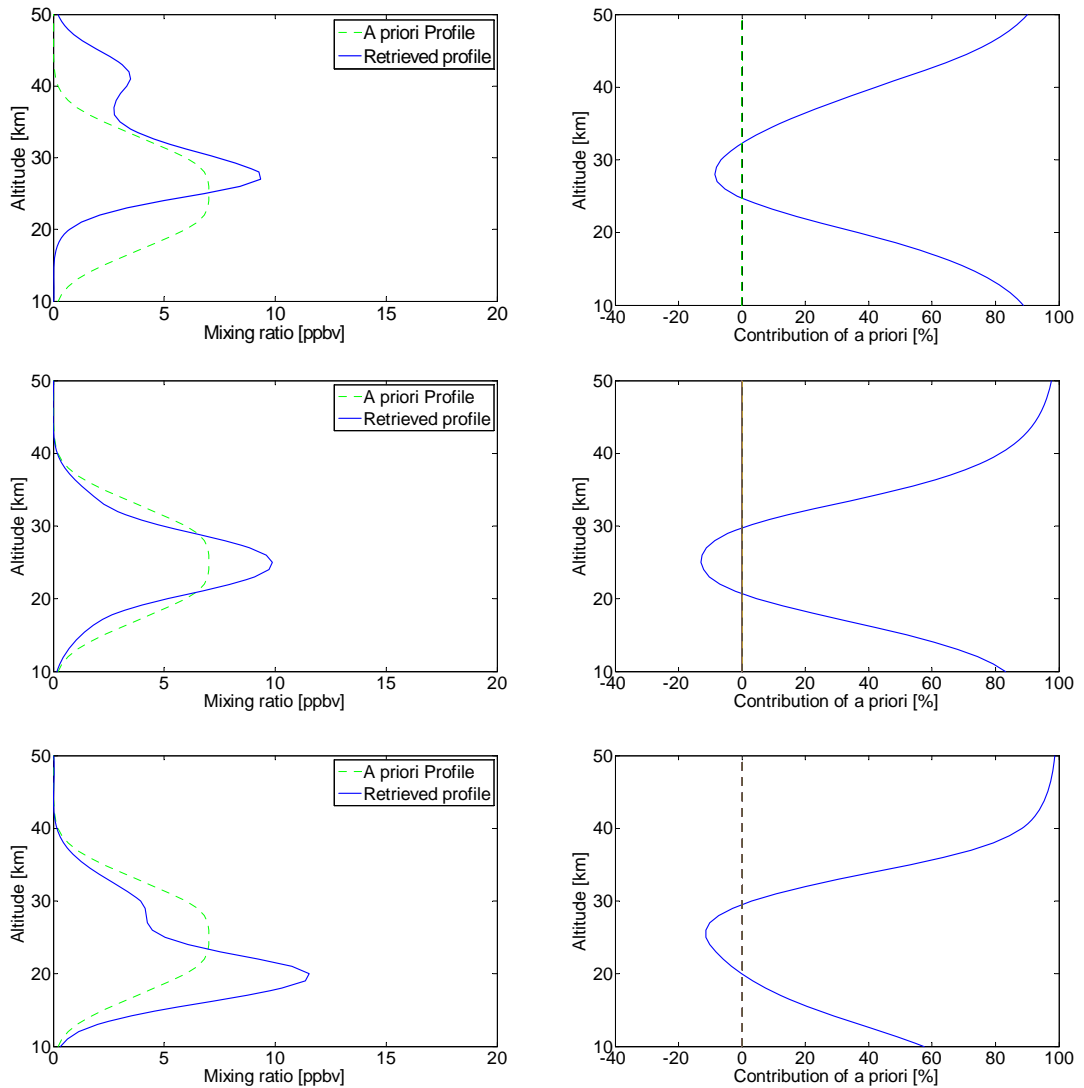


Figure 3.2 Same as figure 3.1. Here all spectra are retrieved using the standard a priori profile. See text for details.

Figure 3.2 shows that using the standard profile the contribution of the a priori to the retrieval is fairly similar for all three cases. Further tests were carried out to assess the retrieval sensitivity to the peak altitude. Two synthetic spectra were generated starting from as many HNO_3 vertical profiles (assumed as “true profiles”), with mixing ratio peak located at 23 km and 27 km, respectively. A random noise of 0.01 K was added and the simulated spectra were retrieved using the standard a priori profile. Figure 3.3 shows that the inversion algorithm is able to locate the altitude peak with an uncertainty of ± 1 km.

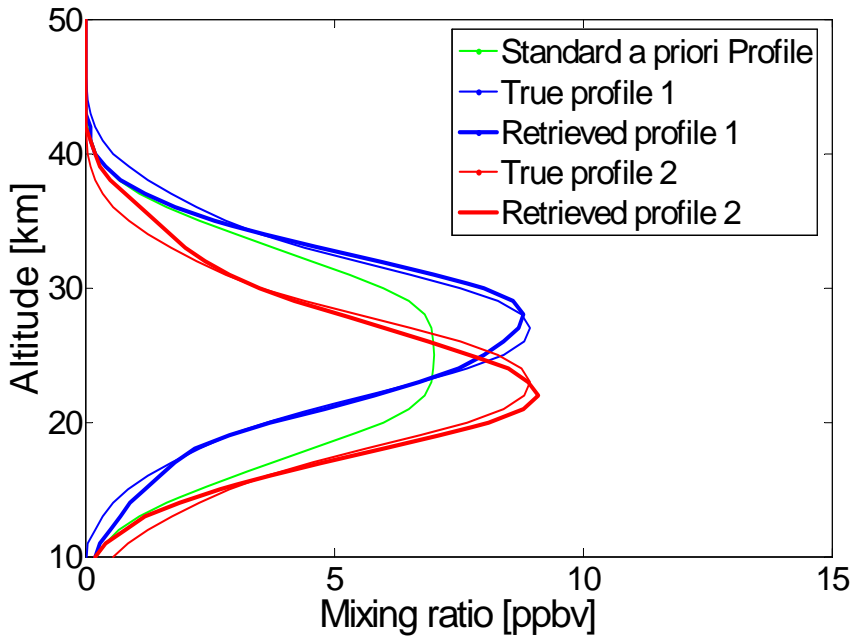


Figure 3.3 True profile used to generate synthetic spectra and corresponding retrieved profiles.

The a priori information for the ozone profile are obtained from ozonesonde data largely available for the locations where the GBMS has been operated. I need to use the most reliable a priori profile for the O₃ retrieval, since very few information about ozone vertical distribution are contained in the observed spectra and the great part of the information comes from the a priori itself. Although balloon profiles extend only up to 30 km, they are well-suited for my goal since the emission of the observed O₃ line wing arises entirely from O₃ molecules located at altitudes below 30 km. Several tests were performed to make sure that ozone molecules above 30 km have no impact on retrieval results.

3.2.3 Covariance matrices

Following the optimal estimation theory, S_{ϵ} is the covariance matrix of the spectral measurement, whose diagonal element should represent the variance of the observed spectrum thermal noise, while the off diagonal elements should give an estimate of the correlation between adjacent frequency channels. A theoretical estimate of the spectral thermal noise for a double side band receiver is given by:

$$\sigma_{\epsilon} = \frac{2T_{sys}}{\sqrt{\delta\nu \cdot \delta t}} \quad (3.15)$$

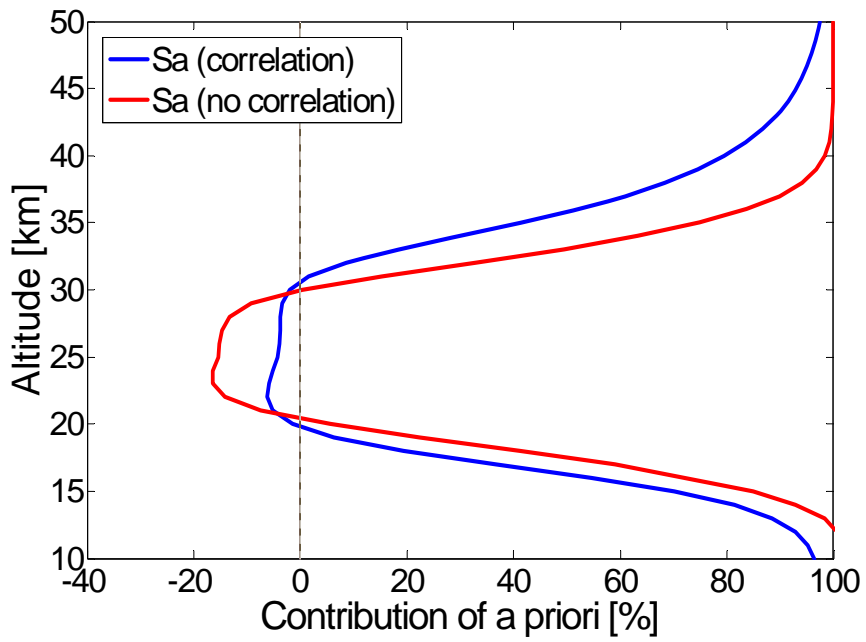
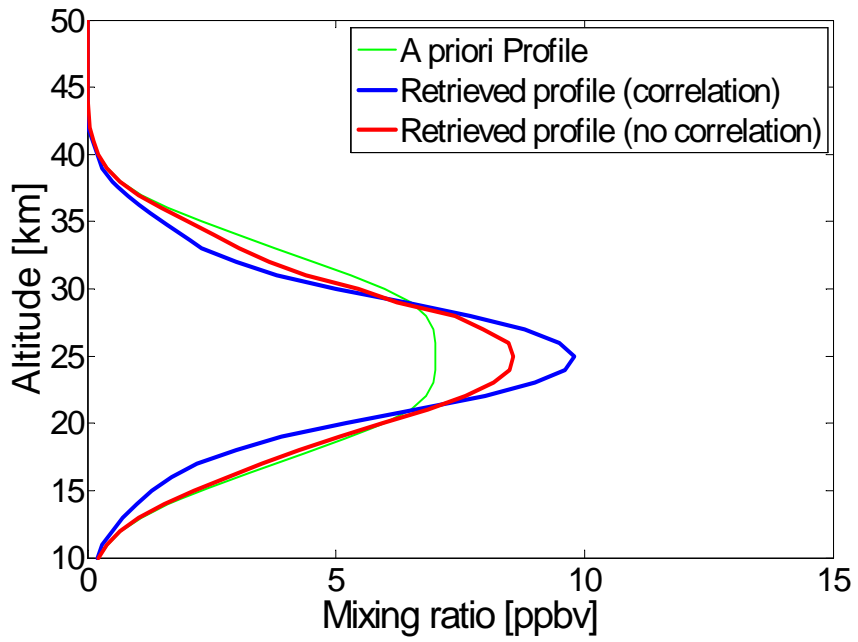
where T_{sys} is the noise temperature of the receiver system, $\delta\nu$ is the bandwidth of a given channel and δt is the integration time. However, this value often underestimates the actual spectral noise and a more realistic value is provided by the spectral residuals. The matrix \mathbf{S}_a should be an estimate of the real uncertainty in \mathbf{x}_a .

In practice, in many semiempirical versions of the method (*Parrish et al.*, 1992, *Naghama et al.*, 1999), both these matrices are treated as adjustable parameters whose values are set empirically by optimizing the performance of the retrieval process in order to have the best possible resolution without introducing ambiguous oscillation in the solution. In this implementation, I assumed constant values for the variances of the HNO_3 and O_3 a priori profiles and I use \mathbf{S}_e as an adjustable parameter for optimizing the retrieval sensitivity. In fact, as the retrieval solution in the OEM is a weighted mean of information coming from the a priori and from the measurement, larger values of σ_e lead to solution relieing mostly on the a priori profile and with very few information added from the measurement. Conversely, decreasing σ_e the a priori information loses importance; the retrieved profile has a better resolution but begins to display undesirable oscillation.

The standard deviation of the HNO_3 a priori profile is set at 40% at all altitudes. This large uncertainty has been chosen in order to have a small retrieval dependence on the standard a priori profile. On the other hand, since little extra information on the ozone distribution is expected to come from the spectrum, a 20% uncertainty was assumed for the O_3 a priori profile. An exponential correlation among stratospheric gases concentrations at different altitudes has been considered:

$$S_a(i, j) = \sigma_{a_i} \sigma_{a_j} \exp\left\{-\left|z_i - z_j\right| \frac{1}{h}\right\} \quad (3.16)$$

where z_i is the i th altitude level, $\sigma_{a_i}^2$ is the corresponding variance and h is the correlation length, which is assumed to be 5 km over the whole atmosphere (*Hoogen et al.*, 1999). Figure 3.4 shows a comparison between sample retrievals obtained assuming \mathbf{S}_a as a diagonal matrix and considering an exponential correlation among molecular concentrations at different altitudes. The Contribution of a priori and the Averaging Kernels plots show that the use of a correlation parameter improves the retrieval sensitivity to the true profile.



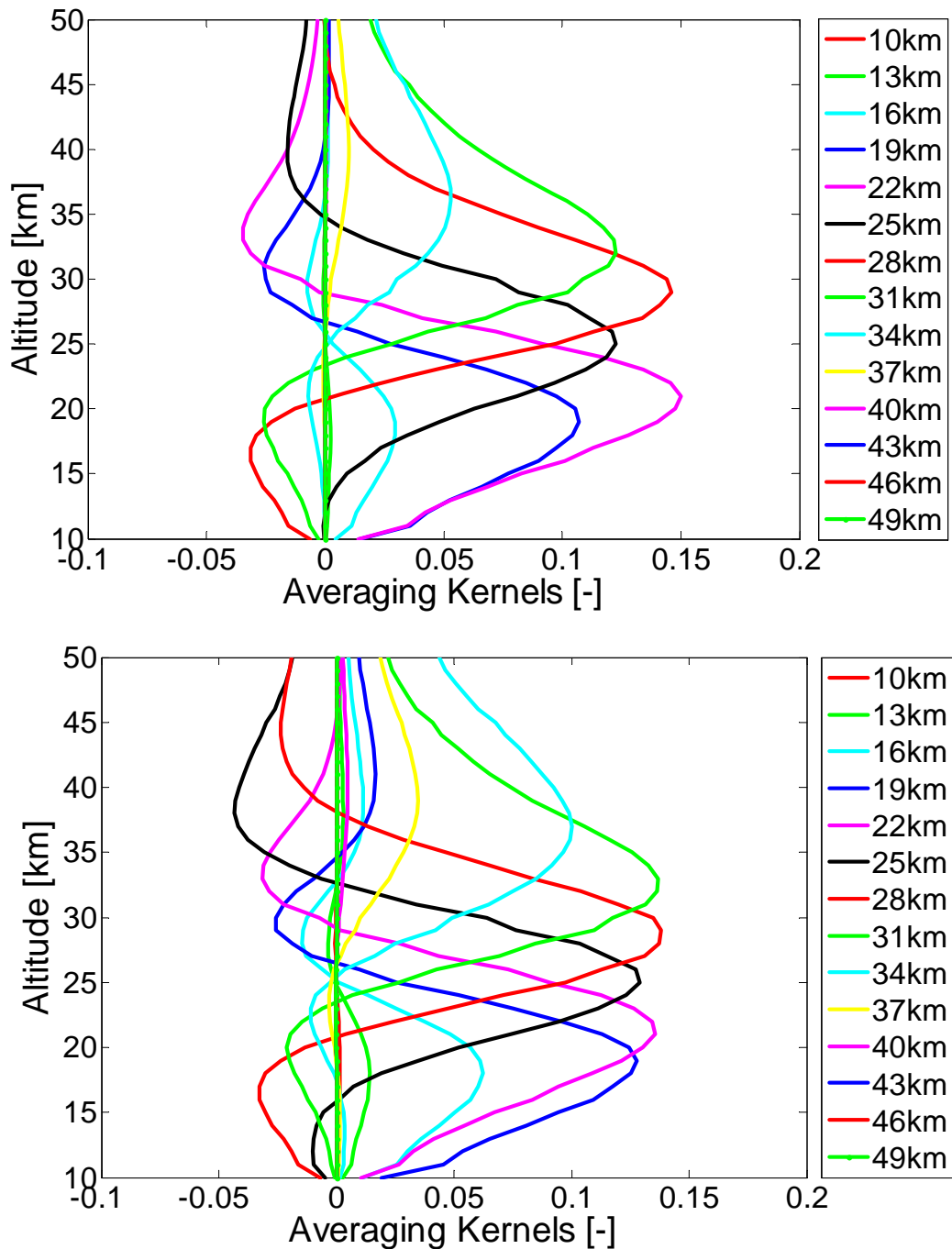


Figure 3.4 Retrieved profiles (top panel), A Priori Contribution (middle panel) and Averaging Kernels (bottom panels) obtained assuming S_a as a diagonal matrix and considering an exponential correlation between HNO_3 and O_3 concentrations at different altitude.

Since there is no significant channel to channel correlation in the spectrum and the thermal noise at each channel is expected to be the same, \mathbf{S}_ε is assumed to be a diagonal matrix with all the diagonal elements equals. The value of the diagonal elements (σ_ε^2) was determined empirically performing a set of inversions on observed and simulated spectra. First of all I retrieved several simulated spectra using different σ_ε values. Figure 3.5 (top panel) shows that a good sensitivity to the true profile is obtained for $\sigma_\varepsilon^2=0.00001$ and $\sigma_\varepsilon^2=0.0001$. Then, I used these σ_ε values to invert measured spectra. Figure 3.5 (bottom panel) shows that using the smallest σ_ε the retrieved profile displays unrealistic oscillations and some negative concentrations at altitudes below 18 km. A $\sigma_\varepsilon^2=0.0001$ value was therefore adopted in this implementation.

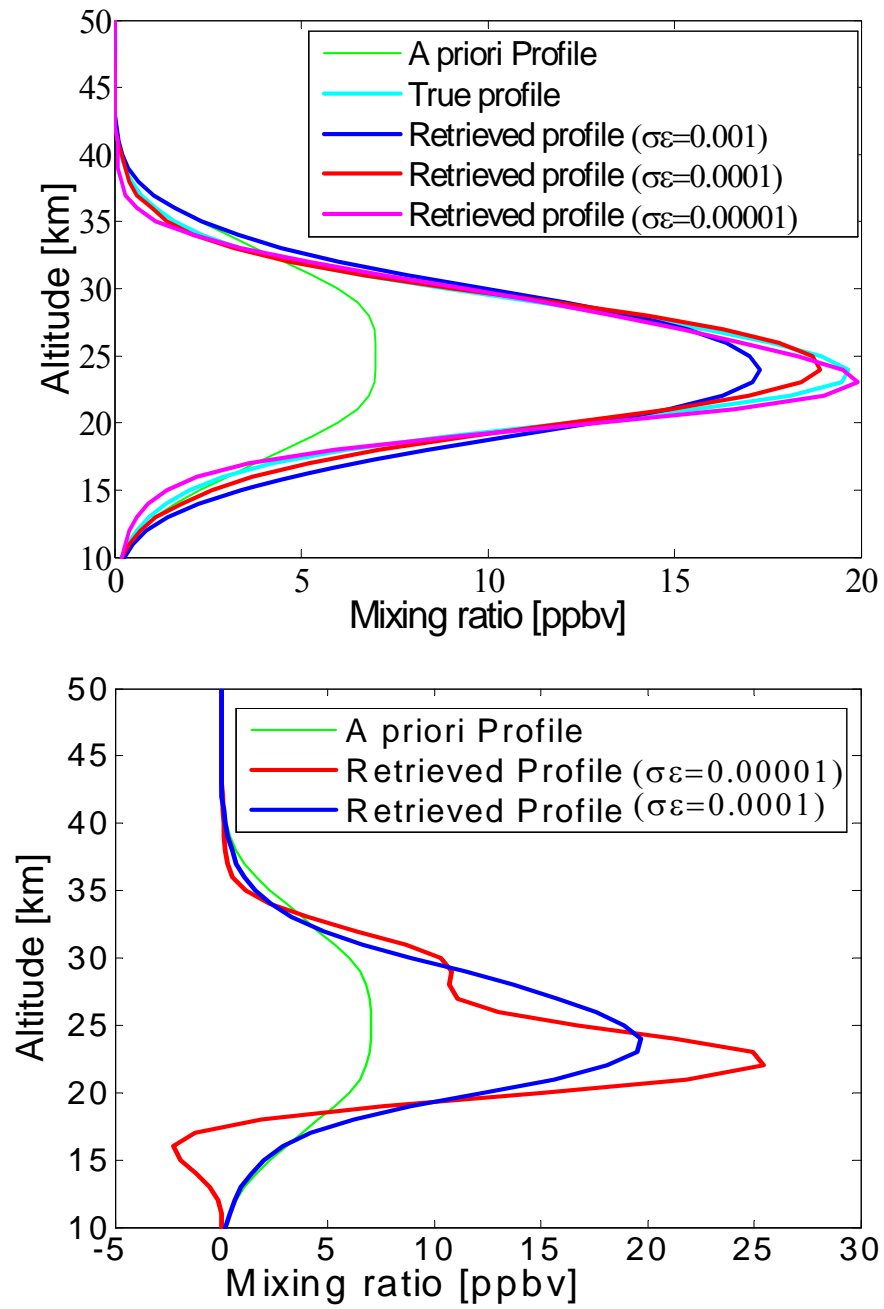


Figure 3.5 Retrieval of simulated (top panel) and measured (bottom panel) spectra using different σ_ϵ values.

3.2.4 Retrieval characterization

In this paragraph several plots, characterizing the inversion performance for a particular retrieved profile, are shown.

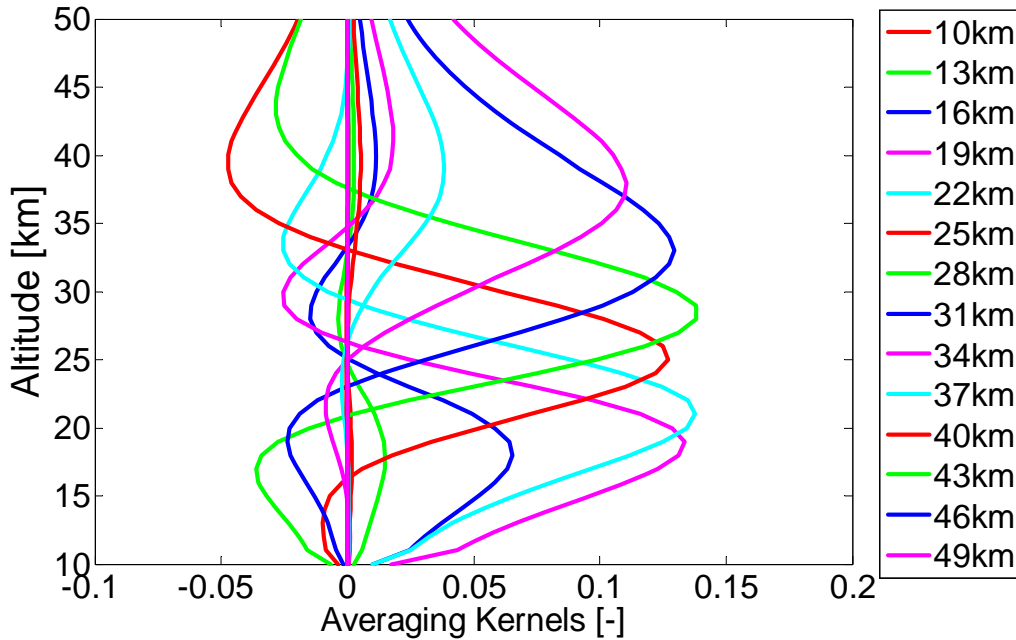


Figure 3.6 GBMS Averaging Kernels for a sample retrieval (measurements carried out in February 2005 at Testa Grigia)

Between 19 and 31 km the nominal and the actual altitudes of the Averaging Kernels peaks agree very well, and the FWHM is 7-9 km (Figure 3.6). This means that a perturbation of the true profile at a specific altitude will correspond to a variation of the retrieved profile at the same, correct, altitude. In this height range the retrieved profiles are most accurate and have the best vertical resolution. Below 18 km and above 32 km the vertical resolution cannot be identified with the averaging kernels FWHM anymore as the spectral measurement is progressively less responsive to variations of the true atmospheric vertical profile.

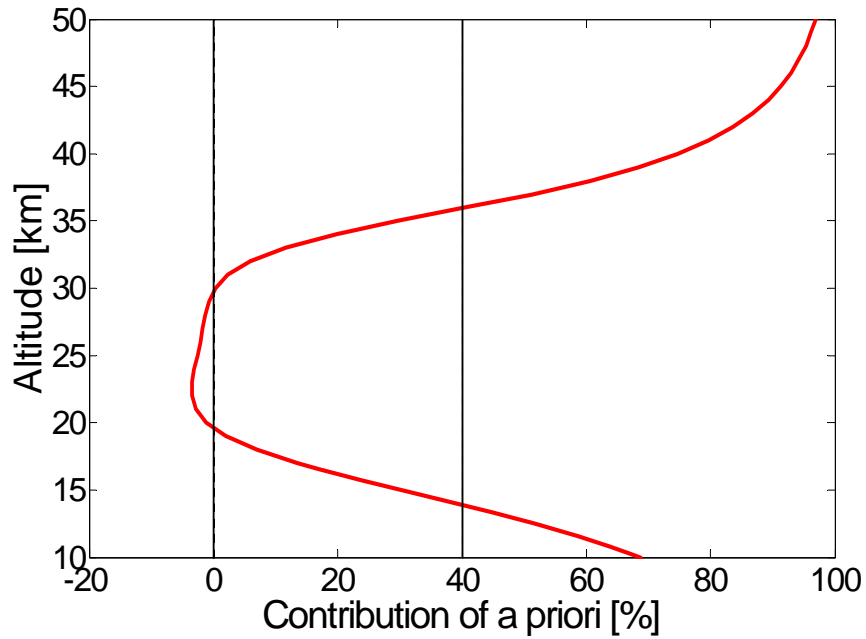


Figure 3.7 Contribution of the a priori profile, in percent, for a sample retrieval (February 2005, Testa Grigia)

The contribution of the a priori profile to the retrieval is typically within 40% between 14 and 36 km. The degree of freedom for signal for this retrieval is $D_s=3.5$.

Uncertainties in the retrieved profile are due to instrument calibration, forward parameters, measurements noise and the retrieval procedure. Those related to calibration procedure and forward parameters (such as spectroscopic parameters, pressure and temperature vertical profiles, etc.) have been estimated to be 15% (*de Zafra et al.*, 1997). Measurements noise have been calculated according to *Connor* (1995). The profile error covariance due to the error in spectral measurements has been calculated as:

$$\mathbf{S}_n = \mathbf{G}\mathbf{S}_\epsilon\mathbf{G}^T \quad (3.17)$$

Here the diagonal elements of \mathbf{S}_ϵ are estimated from the residual obtained subtracting the forward generated spectrum to the observed spectrum. The retrieval error has not been considered here since it arises from the smoothing due to the Averaging Kernels and it must be neglected when considering the comparison between GBMS data and any other data set if the latter is convolved using the GBMS Averaging Kernels.

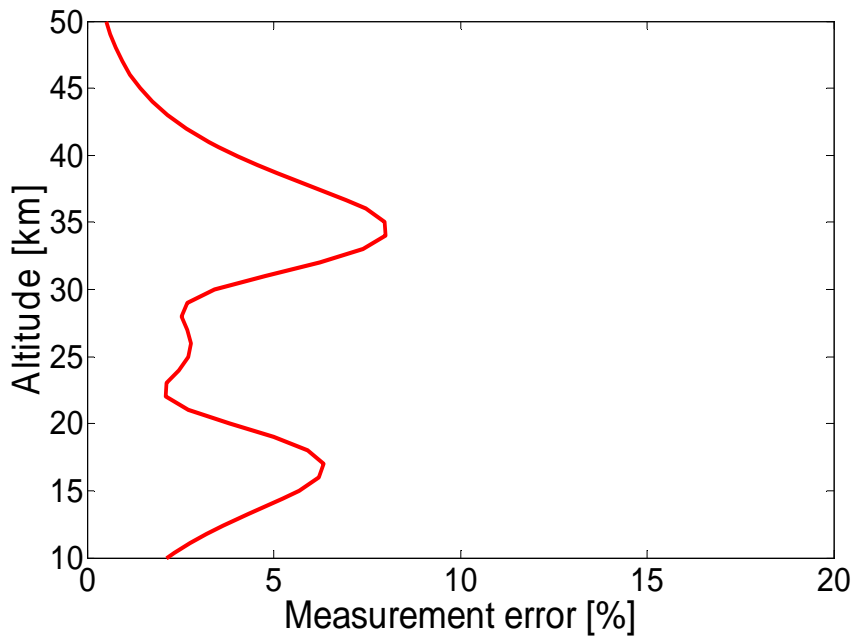


Figure 3.8 Retrieval error due to measurements noise (February 2005, Testa Grigia)

3.2.5 Comparison between OE and Matrix Inversion techniques

From 1993 to 2007, the GBMS HNO_3 spectra were processed using a matrix inversion method (MI) (Twomey, 1977). The MI is an iterative method, essentially immune to the choice of the vertical a priori profile used to start the iteration, employing a vertical smoothing algorithm to constraint the solution. This method can handle the inversion of multiple lines spectra, but the retrieval of spectra containing signatures of different atmospheric constituents is impractical. Therefore, before retrieving HNO_3 spectra, we had to calculate the expected emission intensity from the contaminating ozone line wing (using ozonsonde data) and subtract this background line from the measured spectrum. Errors in the subtraction process, due to the uncertainties in the ozone profile used to simulate the background line, can introduce an artificial slope in the HNO_3 residual spectrum. In order to achieve a good fit an additional parameter, accounting for this slope and allowing to rotate the simulated spectrum, has to be considered in the retrieval. This parameter is somewhat arbitrary and introduce uncertainty in the overall retrieval process. One of the main advantage of The Optimal Estimation Method respect to the MI is the possibility of retrieving the measured spectrum as a whole, avoiding this subtraction process. Another significant

disadvantage of the MI with respect to the OE is the lack of the Averaging Kernel matrix, pivotal for the characterization of the retrieval and for carrying out comparisons with other data sets. In Figure 3.9 HNO₃ profiles retrieved with the new OE and with the old MI method are compared. The overall shape of the profiles are very similar and they agree within error bars in most of the cases.

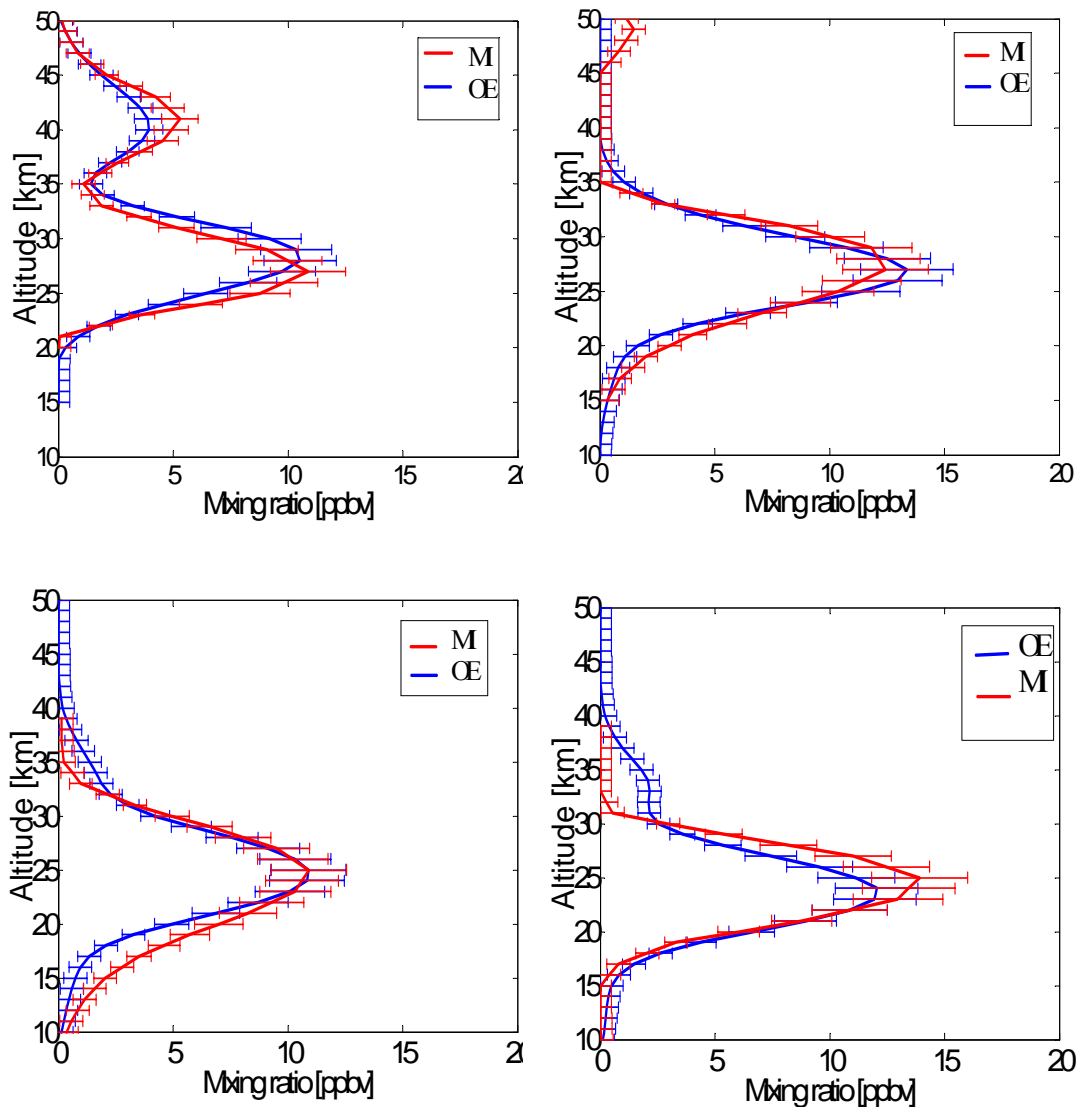


Figure 3.9 HNO₃ profiles retrieved using the Optimal Estimation (blue line) and the Matrix Inversion (red line) methods. Data are from South Pole (top panels) and Testa Grigia (bottom panels)

3.3 Preliminary application of the OE to O₃ and N₂O spectra

The GBMS observes molecular rotational lines of several trace gases that emit between 230 and 280 GHz, and is tunable in this frequency range. During most of the field campaigns carried out in the last 18 years the GBMS has measured emission lines of O₃ at 276.923 GHz, N₂O at 276.328 GHz and CO at 230.538 GHz, besides the HNO₃ lines cluster centered at 269.211 GHz. Ozone and CO spectra are measured with a ~1.5-hour integration. About 4 hours of integration are needed for HNO₃ and N₂O lines, which are weaker than those of O₃ and CO (*Muscari et al.*, 2007). In principle also HCN (at 265.886 GHz), and HDO (at 255.050 GHz) lines could be observed; in practice, excellent atmospheric conditions and very long integration times are required for measuring these extremely weak lines. Thus, very few HCN and HDO measurements have been taken along the years. The observed spectra have dissimilar features and, until now, have been deconvolved using two different algorithms. A modified Chahine-Twomey method (*Twomey et al.*, 1977) was adopted for retrievals of the single-line O₃, N₂O and CO spectra, whereas a constrained matrix inversion technique (*Twomey*, 1977) had to be used for HNO₃, owing to its more complex spectrum. Moreover, both O₃ and N₂O lines lie on the wing of strong ozone lines centered outside the 600 MHz spectral windows. In the C-T technique this ozone background had to be subtracted from the measured data in a pre-processing phase. One major advantage of the new Optimal Estimation Method, illustrated in previous sections for HNO₃ retrievals, is that it is extremely flexible and can be straightforwardly adapted to the different emission spectra observed by GBMS, without any pre-processing subtraction procedure. In this paragraph, I briefly present preliminary results of O₃ and N₂O retrievals obtained using the OE method. First I have considered noisy synthetic radiance spectra, generated starting from arbitrarily chosen concentration profiles and adding an appropriate level of random noise to the spectra. I inverted these simulated spectra in order to test the degree to which profiles retrieved from them match true profiles. Then the algorithm was applied to spectra actually measured by means of

GBMS. More retrieval results are illustrated in a paper recently submitted to *Journal of Geophysical Research* (see Appendix A), presenting ground-based measurements of middle atmospheric temperature, O₃, CO, and N₂O profiles obtained at Thule, Greenland, during the 2009 polar winter. O₃ and N₂O GBMS measurements presented in that paper are analyzed using the OE method I developed for use with GBMS spectra.

3.3.1 Ozone retrievals

3.3.1.1 Noisy synthetic data

Synthetic spectra of the ozone pure rotational transition at 276.923GHz were generated starting from two different O₃ profiles (characterized by a single and a double peak, respectively). A random noise with a standard deviation of 0.1 K was added (Figure 3.10). To invert these artificial data the measurement error covariance matrix S_{ϵ} was chosen as a diagonal matrix with the diagonal element set at 0.01 K. An uncertainty ranging from 0.5 ppmv to 1.3 ppmv (depending on the altitude) was used for the O₃ mixing ratio a priori profile. The same correlation between adjacent levels adopted for the HNO₃ profiles was considered. In Figure 3.11 retrieval results for the two different initial profiles are shown. The agreement between the retrieved and the original profile is very good for the first retrieval (left panel), whereas some deviations are observed in the inversion of the double peak profile (right panel). However, also in this second case the overall agreement is fairly good, with differences lower than 0.6 ppmv (~10%) mainly due to the limited GBMS vertical resolution.

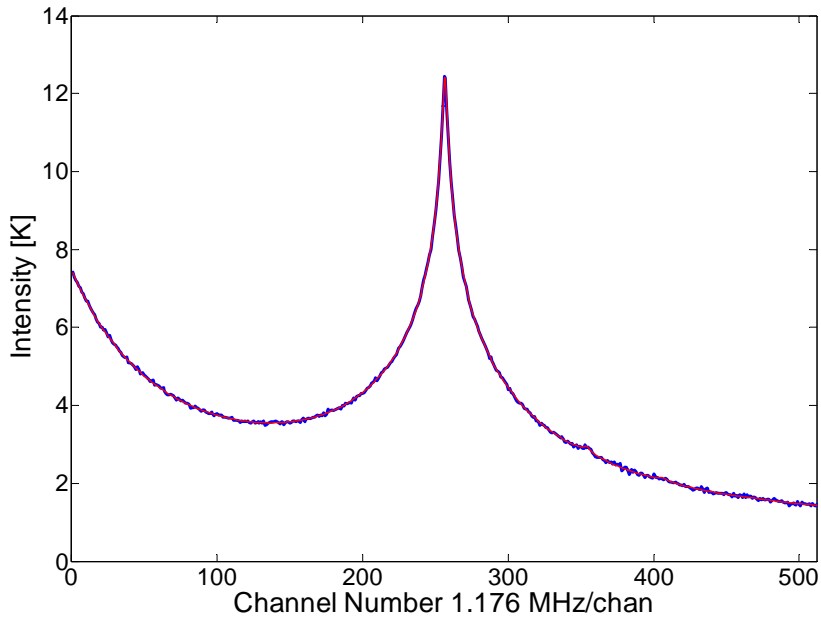


Figure 3.10 Synthetic spectra of the ozone pure rotational transition at 276.923GHz generated starting from the “true” profile shown in figure 3.11 (left panel) and adding a random noise with a standard deviation of 0.1 K.

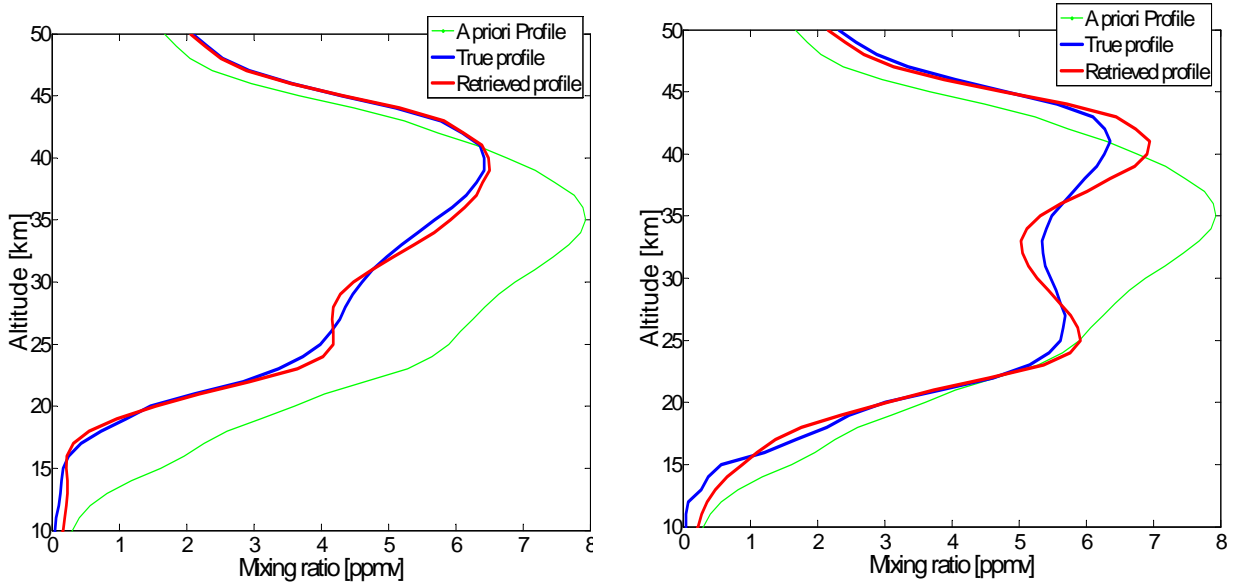


Figure 3.11 Retrieval results of simulated spectra generated starting from two different O_3 profiles characterized by a single and a double peak (left and right panel, respectively).

The same ozone initial profiles were used to generate other synthetic O_3 spectra characterized by three strong lines centered at 276,923 GHz, 279,485 GHz and 279,892 GHz (Figure 3.12). This emission spectrum could be observed by the GBMS tuning the local oscillator at 278,323 GHz but has never been measured until present. In fact, since multiple-line spectra were harder to retrieve with the old method, the line at 276.923 was chosen for ozone observations. Nevertheless, these tests were performed in order to investigate the possibility of using this spectral window for O_3 future measurements. The same parameters used in the retrieval of the 276,923 GHz spectrum were adopted here. The retrieval results, shown in Figure 3.13, are very similar to those obtained for the 276,923 GHz spectrum, demonstrating that this spectral window could be useful for ozone observations.

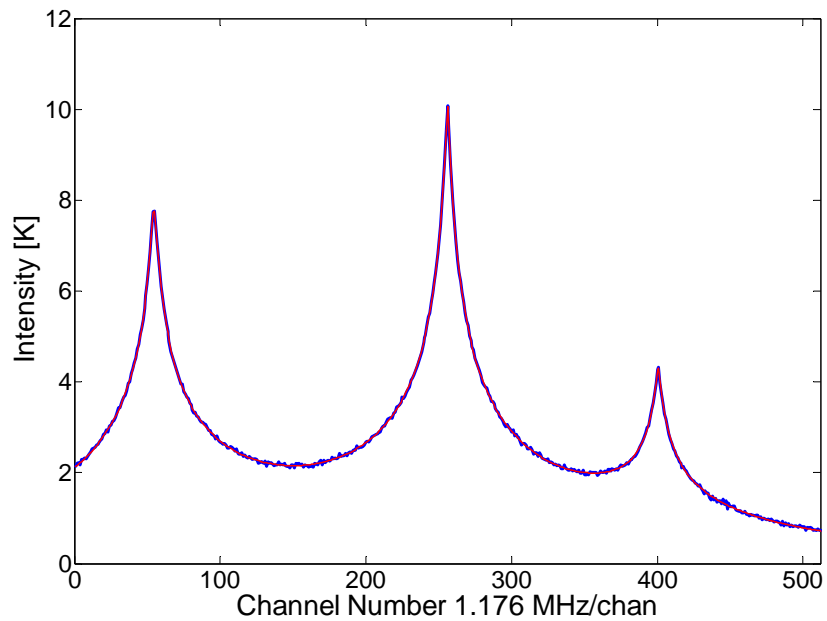


Figure 3.12 Ozone spectrum characterized by three strong O_3 lines centered at 276,923 GHz, 279,485 GHz and 279,892 GHz, which could be observed by the GBMS tuning the local oscillator at 278,323 GHz. This spectrum was generated starting from the “true” profiles shown in figure 3.13 (left panel) and adding a random noise with a standard deviation of 0.1 K.

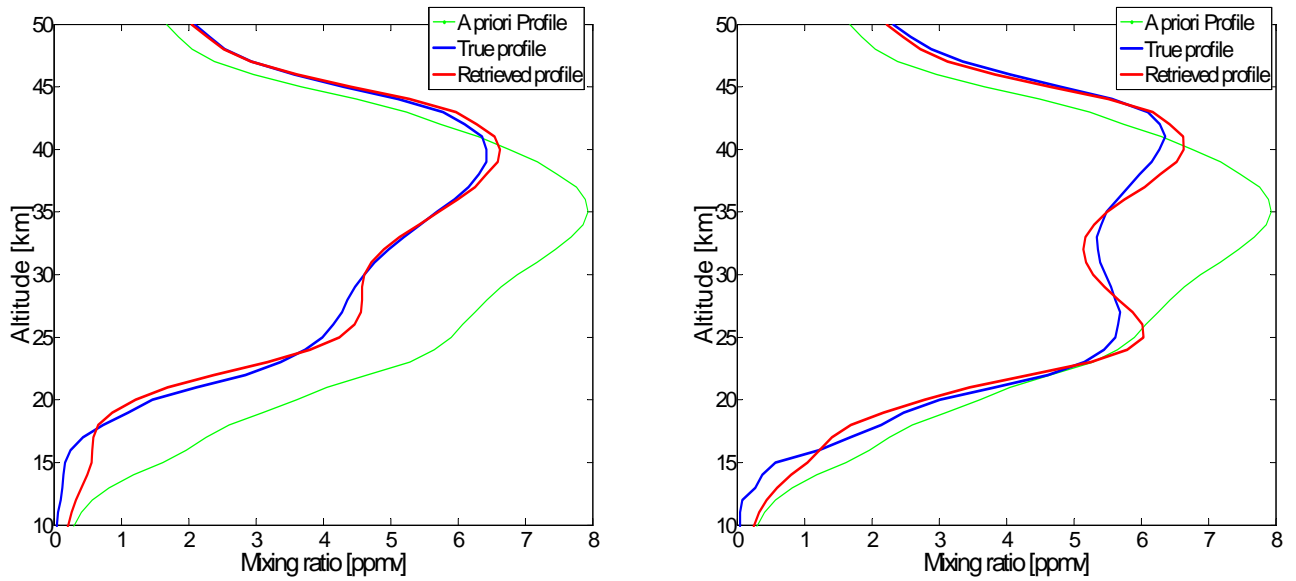


Figure 3.13 Retrieval results of simulated spectra, generated starting from two different O₃ profiles characterized by a single and a double peak (left and right panel, respectively).

3.3.1.2 Measured data

In Figure 3.14 an ozone spectrum recorded at Thule on February 20, 2009, superimposed with the spectrum calculated from the retrieved profile, is shown. An error measurement variance of 0.03 K, slightly larger than that used for synthetic spectra retrieval, has been adopted here. The retrieved profile is shown in Figure 3.15. In this figure the profile retrieved from concurrent ozonsonde data launched from Thule Air Base is also shown. The agreement between the two profiles is fairly good, except for smaller-scale vertical structures evident only in the balloon data due to the GBMS coarser vertical resolution. The Averaging Kernels (figure 3.16) and the Contribution of the a priori profile (figure 3.17) show that GBMS data allow to retrieve reliable ozone mixing ratio profile between ~15 and ~55 km, with a vertical resolution of 7-8 km. This correspond to ~5-6 independent mixing ratio values in the considered vertical range ($DF_s=5.5$).

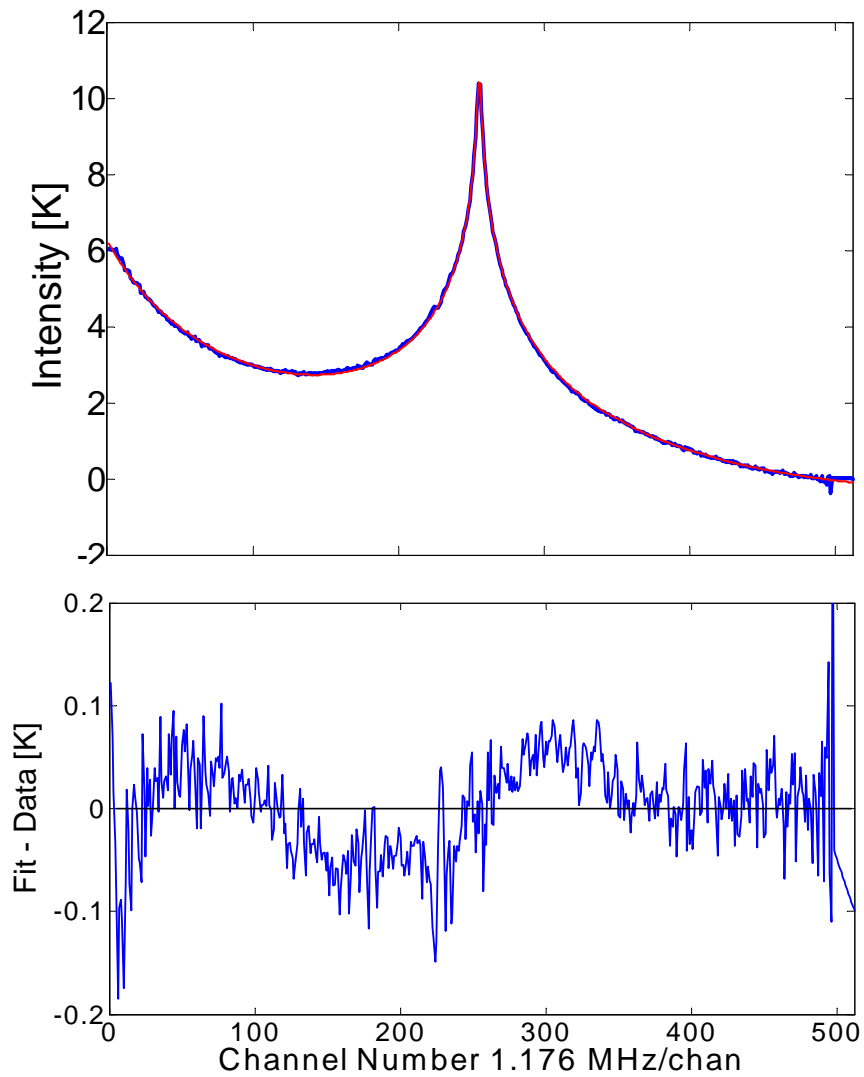


Figure 3.14 Top panel: ozone spectrum recorded at Thule on February 20, 2009 (blue line), superimposed with the spectrum calculated from the retrieved profile (red line). Bottom panel: difference between the measured and the forward calculated spectra.

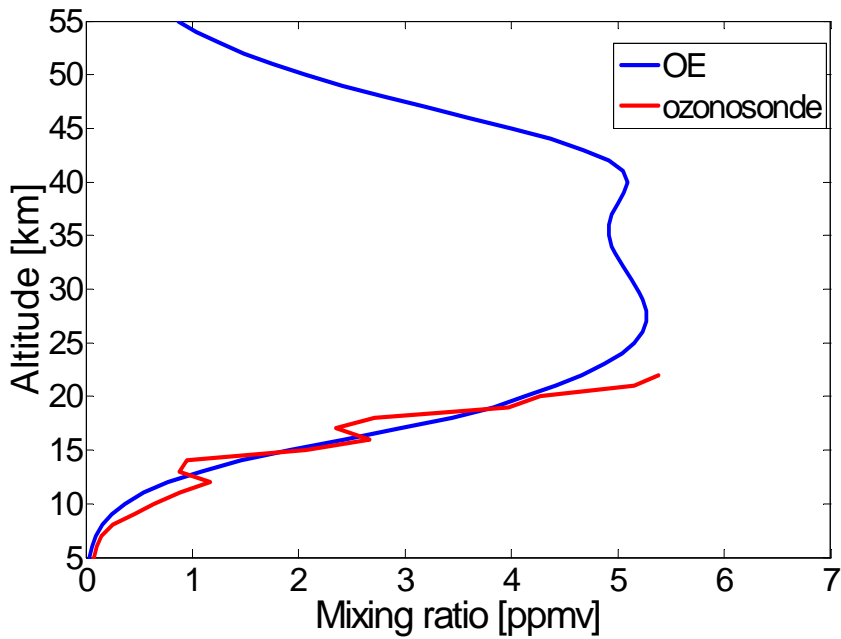


Figure 3.15 Ozone profile retrieved from the spectrum recorded at Thule on February 20, 2009 shown in figure 3.14. The red line is the profile retrieved from concurrent ozonosonde data.

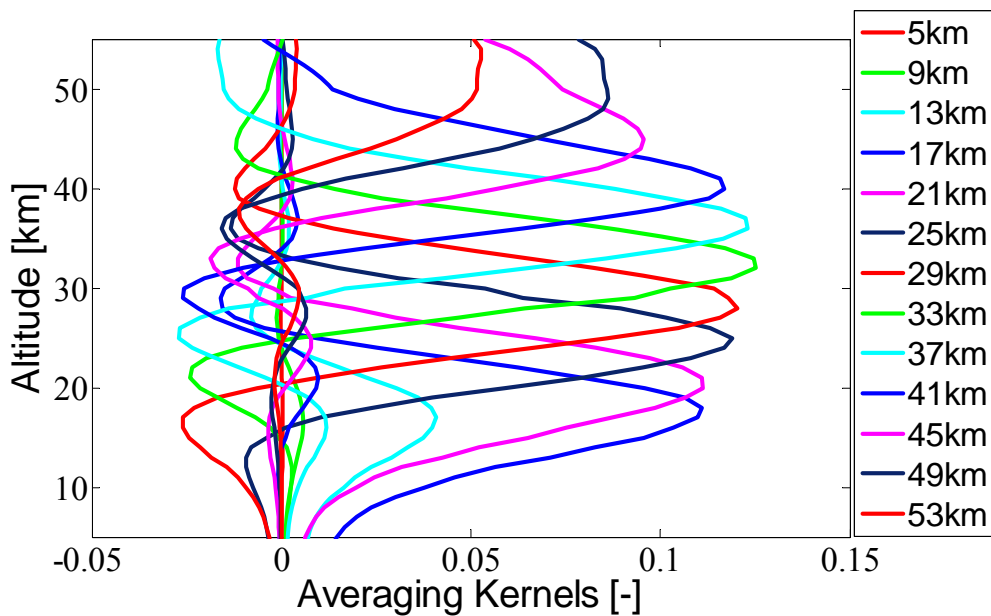


Figure 3.16 GBMS Averaging Kernels for ozone as determined from measurements carried out on February 20, 2009 at Thule.

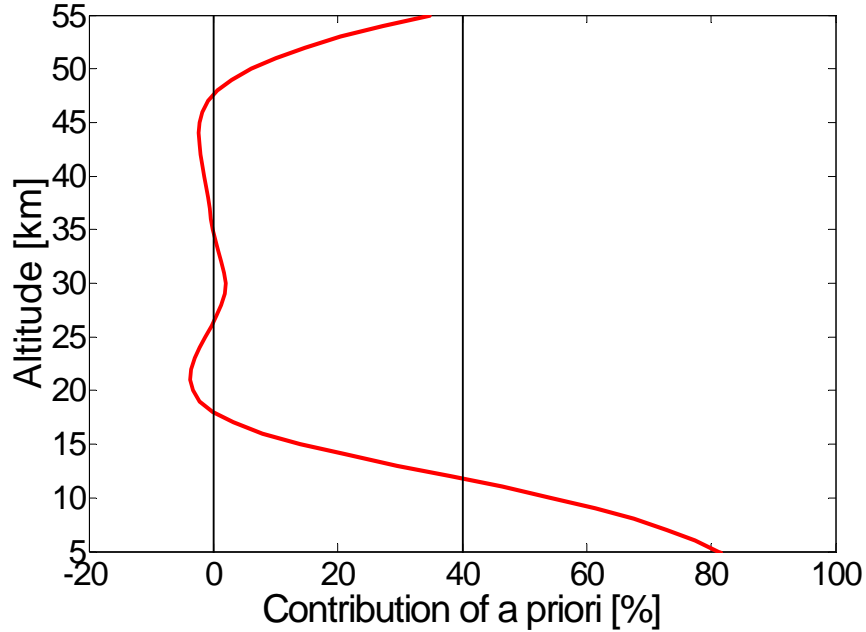


Figure 3.17 Relative contribution of the a priori profile for the retrieved profile shown in figure 3.15

3.3.2 Nitrous Oxide retrievals

3.3.2.1 Noisy synthetic data

The “true” Nitrous oxide profile shown in Figure 3.18 (blue line) was used to generate a synthetic spectra of the N_2O pure rotational transition at 276.328 GHz. A random noise with a standard deviation of 0.1 K was added. I again adopted a diagonal S_ϵ matrix (with $\sigma_\epsilon^2 = 0.01$ K) and a non diagonal matrix S_a (with σ_a^2 ranging from 0.001 to 0.08 and an exponential correlation between different altitudes) for this inversion. In Figure 3.18, the a priori and the “true” profile used in this inversion, together with the profile obtained as retrieval result are shown.

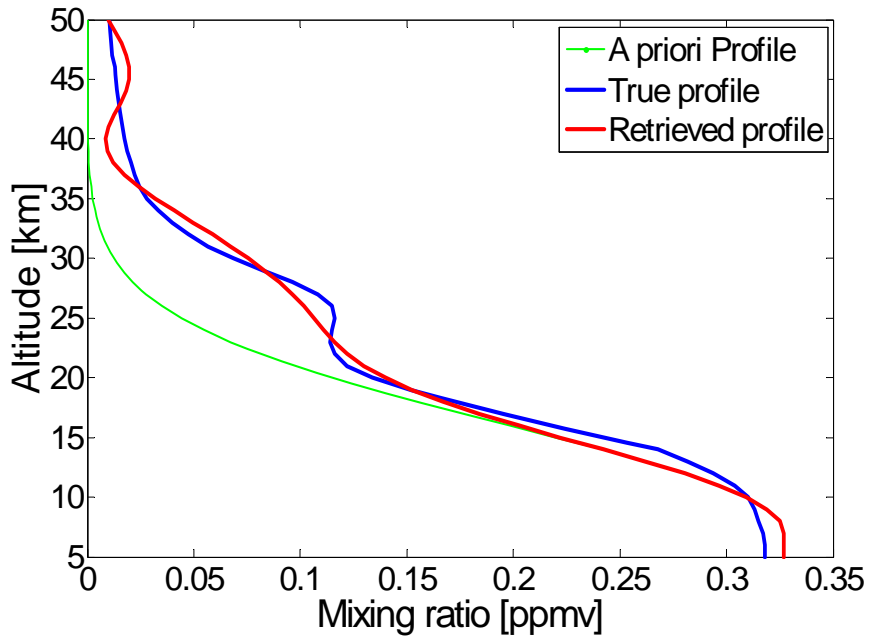


Figure 3.18 The red line is the retrieval result for N_2O synthetic spectrum generated starting from the true profile shown in blue. The green line is the a priori profile.

3.3.1.2 Measured data

Figure 3.19 shows a nitrous oxide spectrum recorded at Thule on February 20, 2009 superimposed with the forward calculated spectrum. The retrieved profile is shown in Figure 3.20. The Averaging Kernels (Figure 3.21) show that nitrous oxide profile are most accurate between ~ 18 and ~ 45 km, with a vertical resolution of 7-8 km.

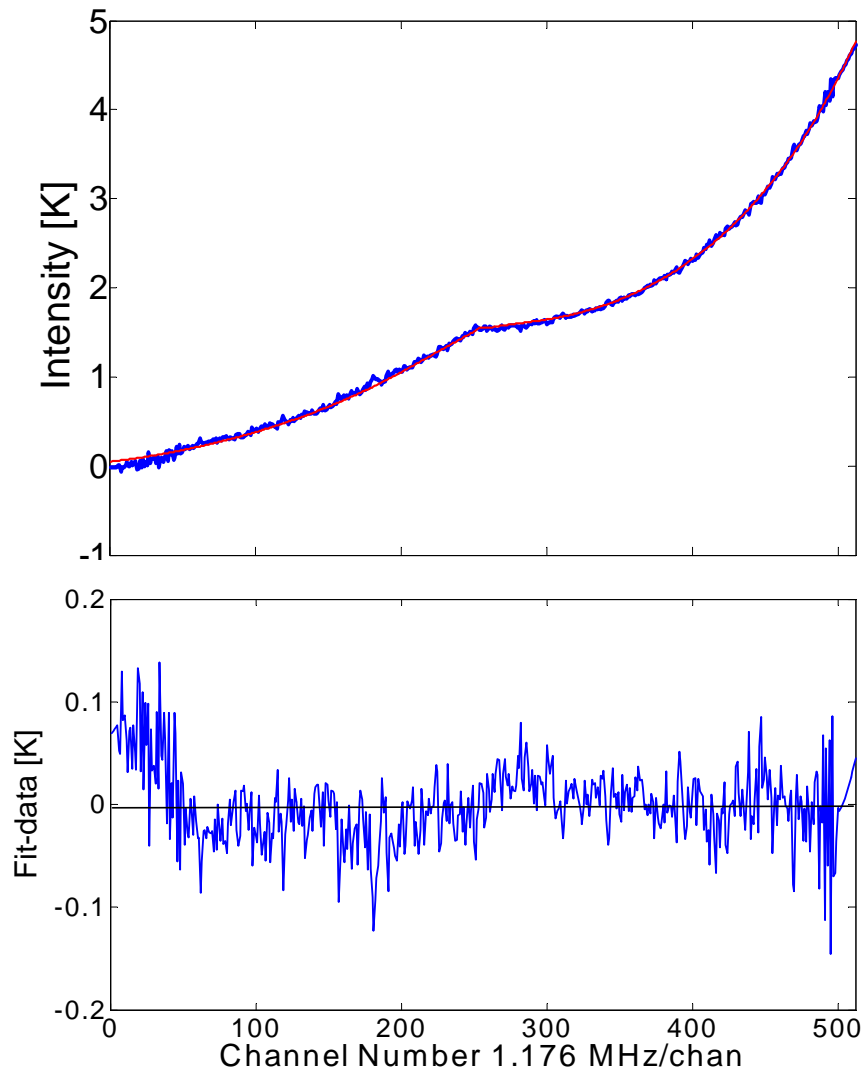


Figure 3.19 Top panel: N_2O spectrum recorded at Thule on February 20, 2009 (blue line), superimposed with the spectrum calculated from the retrieved profile (red line). Bottom panel: difference between the measured and the forward calculated spectra

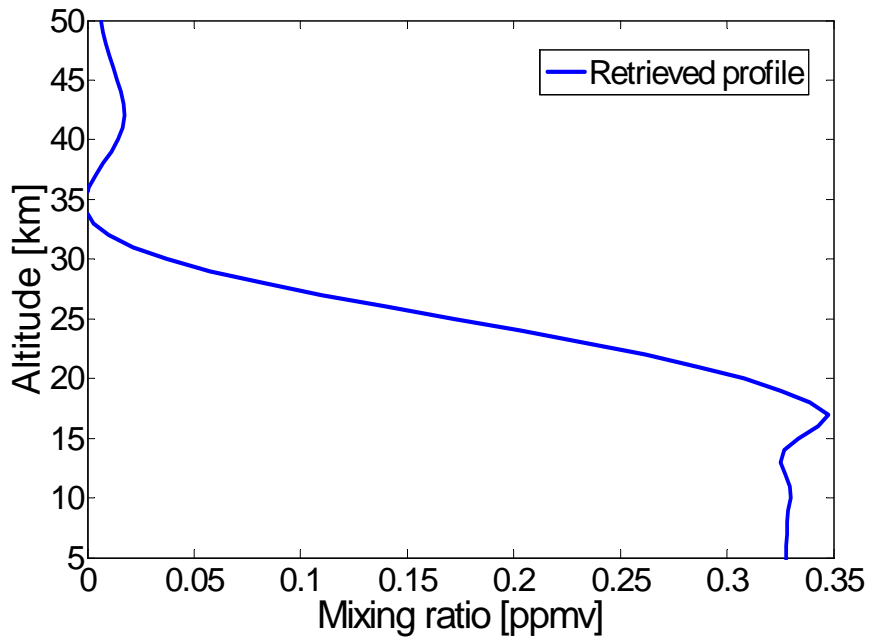


Figure 3.20 N₂O profile retrieved from the spectrum recorded at Thule on February 20, 2009 shown in figure 3.19

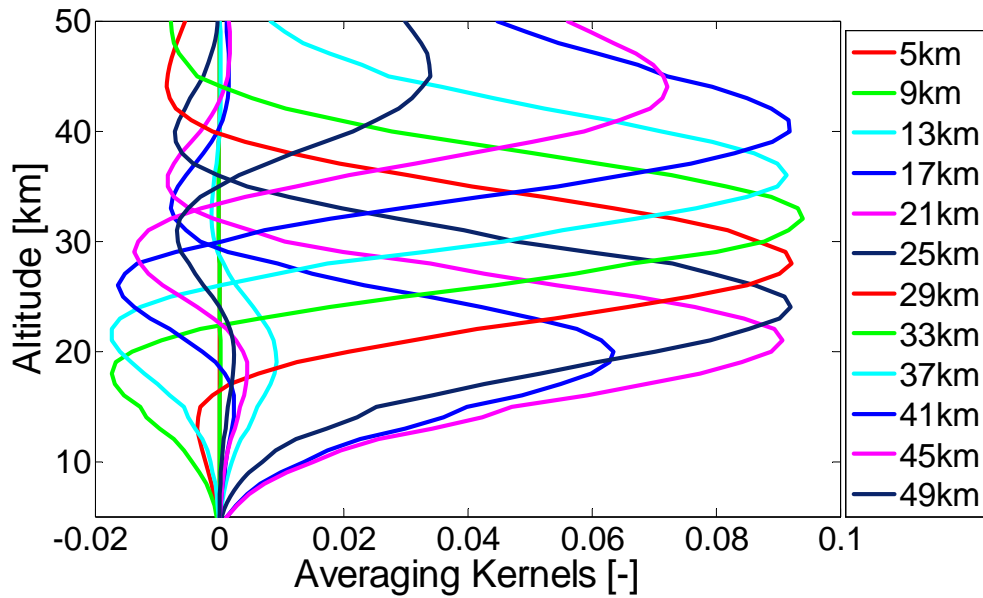


Figure 3.21 GBMS Averaging Kernels for N₂O as determined from measurements carried out on February 20, 2009 at Thule

Chapter 4

Comparison of HNO₃ retrievals with satellite measurements

In the past 30 years numerous data sets relevant to the issue of the ozone depletion were recorded from several different satellite missions and sensors (SAGE I, SAGE II, SAGE III, UARS MLS, UARS HALOE, POAM II, POAM III, ACE, EOS Aura MLS) as well as from several ground based instruments (included in the Network for the Detection of Atmospheric Composition Change). Although somewhat discontinuous and not consistent, these data records have been pivotal for understanding the ozone change and for making critical decision in the international public policy in order to mitigate the ozone depletion (i.e. the Montreal protocol in 1982 and its amendments). At the present day, one of the major need for the atmospheric research community is the creation of a unified and coherent long term data record of ozone and related trace gases, providing tighter model constraint and allowing to improve predictive capability (WMO, 2007). In the framework of the construction of such a global data set, comparison between ground-based and satellite observation are extremely useful. In fact ground-based observations can be critically used for assessing offsets between different satellite data sets, as well as to fill gaps in temporal coverage.

In this Charter I present an intercomparison between GBMS HNO₃ measurements and two satellite data sets produced by the two NASA/JPL Microwave Limb Sounder (MLS) experiments (aboard the Upper Atmosphere Research Satellite (UARS) from 1991 to 1999, and on the Earth Observing System (EOS) Aura mission from 2004 to date). In particular, I compare Aura MLS observations with GBMS HNO₃ measurements obtained from the Italian Alpine station of Testa Grigia, during the period February 2004 - March 2007, and from Thule Air Base, Greenland, during polar

winter 2008/09. A similar intercomparison is made between the UARS MLS HNO₃ measurements with those carried out from the GBMS at the South Pole during the greater part of 1993 and 1995. I assess systematic differences between GBMS and both UARS and Aura MLS HNO₃ data sets at given potential temperature levels. These comparisons have been performed as part of GOZCARDS (Global Ozone Chemistry and Related Trace gas Data Records for the Stratosphere) a multiyear NASA JPL project aimed at developing a long-term data record of stratospheric constituents relevant to the issues of ozone decline and expected recovery. Since the GBMS has been operated for more than 15 years (with minor instrumental upgrading), the GBMS HNO₃ data record is the only existing resource for the cross-calibration of HNO₃ measurements from the two MLS experiments. This cross calibration is pivotal to the GOZCARDS objective, helping to establish a unique HNO₃ data set from 1991 to date.

Moreover, the participation to this project provides the opportunity for the first comparison of the GBMS HNO₃ retrievals obtained with the new inversion method.

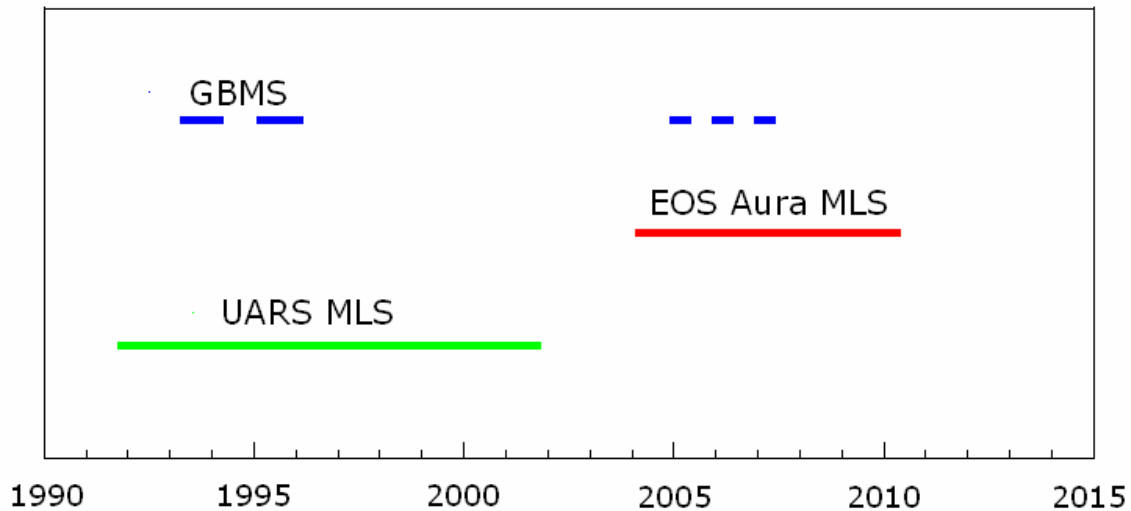


Figure 4.1 Timeline of observations for the two MLS experiments (aboard UARS and EOS Aura mission) and for the GBMS .

For a complete validation of the GBMS measurements, a preliminary validation of the tropospheric opacity τ_z (accounting for the fraction the stratospheric radiation absorbed in troposphere, before reaching the ground) is critical. As seen in Chapter 2, GBMS HNO₃ spectra need to be scaled before being retrieved. The main uncertainty in this calibration procedure come from τ_z , which is regularly derived during GBMS data

taking. In the spectral region sampled by GBMS the atmospheric opacity arises almost entirely from the water vapor continuum and the conversion from τ_z to precipitable water vapor (pwv) can be obtained by means of a simple linear relationship. Therefore, a validation of pwv measurements provides a tool for assessing the accuracy of opacity values used for scaling GBMS spectra. An extensive validation of GBMS opacity measurements has been obtained by means of simultaneous PWV observations performed by Vaisala RS92k radiosondes (Rowe *et al.*, 2008), a Raman Lidar (Di Girolamo *et al.*, 2004), and an IR Fourier Transform Spectrometer (Bianchini *et al.*, 2006). These sets of measurements were carried out during the primary field campaign of the ECOWAR (Earth COoling by WAter vapour Radiation) project which took place at Breuil-Cervinia (45.9 N, 7.6 E, elev. 1990 m) and Plateau Rosa, Italy, from 3 to 16 March, 2007.(Bhawar *et al.*, 2008) The first section of the chapter is dedicated to this preliminary validation, presented in the paper: “*Measurements of low amounts of precipitable water vapor by millimeter wave spectroscopy: An intercomparison with radiosonde, Raman lidar, and Fourier transform infrared data*”, published on the *Journal of Geophysical Research*. Additional results obtained comparing GBMS and FTIR measurements are illustrated in the paper “*Water vapor sounding with the far infrared REFIR-PAD spectroradiometer from a high-altitude ground-based station during the ECOWAR campaign*”, submitted to *Atmospheric Chemistry and Physics* and presented in Appendix B

4.1 Measurements of low amounts of precipitable water vapor by mm-wave spectroscopy: an intercomparison with radiosonde, Raman Lidar and FTIR data

1 **Measurements of low amounts of precipitable water**
2 **vapor by mm-wave spectroscopy: an intercomparison**
3 **with radiosonde, Raman Lidar and FTIR data**

4 Irene Fiorucci^{1,2}, Giovanni Muscari¹, Cesidio Bianchi¹, Paolo Di Girolamo³, Francesco
5 Esposito³, Giuseppe Grieco³, Donato Summa³, Giovanni Bianchini⁴, Luca Palchetti⁴,
6 Marco Cacciani⁵, Tatiana Di Iorio⁵, Giulia Pavese⁶, Domenico Cimini⁷, and Robert L. de
7 Zafra⁸

8

9

10

11 ¹ Istituto Nazionale di Geofisica e Vulcanologia, Roma, Italy

12 ² also at Dipartimento di Fisica, Università di Bologna, Bologna, Italy

13 ³ Dipartimento di Ingegneria e Fisica dell'Ambiente, Università della Basilicata, Potenza,
14 Italy

15 ⁴ Istituto di Fisica Applicata "Nello Carrara", CNR, Sesto Fiorentino, Firenze, Italy

16 ⁵ Dipartimento di Fisica, Università di Roma "La Sapienza", Roma, Italy

17 ⁶ Istituto di Metodologie per l'Analisi Ambientale, CNR, Tito Scalo, Potenza, Italy

18 ⁷ CETEMPS, Dipartimento di Fisica, Università di L'Aquila, L'Aquila, Italy

19 ⁸ Department of Physics and Astronomy, and Institute for Terrestrial and Planetary
20 Atmospheres, State University of New York, Stony Brook, U.S.A.

21

21 **Abstract.** Observations of very low amounts of precipitable water vapor (PWV) by
22 means of the Ground-Based Millimeter-wave Spectrometer (GBMS) are discussed. Low
23 amounts of column water vapor (between 0.5 and 4 mm) are typical of high mountain
24 sites and polar regions, especially during winter, and are difficult to measure accurately
25 due to the lack of sensitivity of conventional instruments to such low PWV contents. The
26 technique used involves the measurement of atmospheric opacity in the range between
27 230 and 280 GHz with a spectral resolution of 4 GHz, followed by the conversion to
28 precipitable water vapor using a linear relationship. We present the intercomparison of
29 this data set with simultaneous PWV observations obtained with Vaisala RS92k
30 radiosondes, a Raman Lidar, and an IR Fourier Transform Spectrometer. These sets of
31 measurements were carried out during the primary field campaign of the ECOWAR
32 (Earth COoling by WAter vapor Radiation) project which took place at Breuil-Cervinia
33 (45.9° N, 7.6° E, elev. 1990 m) and Plateau Rosa (45.9° N, 7.7° E, elev. 3490 m), Italy,
34 from 3 to 16 March, 2007. GBMS PWV measurements show a good agreement with the
35 other three data sets exhibiting a mean difference between observations of $\simeq 9\%$. The
36 considerable number of data points available for the GBMS versus Lidar PWV
37 correlation allows an additional analysis which indicates negligible systematic differences
38 between the two data sets.
39

39 **1. Introduction**

40 Water vapor is a critical component of the atmosphere, plays a key role in the
41 Earth's radiative balance and it is the most important atmospheric greenhouse gas due to
42 its intense absorption of both shortwave and longwave radiation [e.g., *Raval and*
43 *Ramanathan*, 1989; *Held and Soden*, 2000; *Marsden and Valero*, 2004]. Accurate
44 measurements of the atmospheric water distribution are therefore essential to adequately
45 model Earth's radiation budget, with the column amount of water vapor (precipitable
46 water vapor, or PWV) being one of the most important input parameters for atmospheric
47 models [e.g., *Clough et al.*, 1992].

48 Of particular interest are regions characterized by very low atmospheric water vapor
49 contents, such as polar regions. These regions are extremely vulnerable to present and
50 projected climate changes and at the same time are the regions with the greatest potential
51 to affect global climate [*Solomon et al.*, 2007]. Obtaining accurate measurements of low
52 amounts of PWV is especially important, for example, for modeling longwave radiative
53 fluxes during polar winter months. Substantial variations in longwave emission caused by
54 fluctuations in low amounts of water vapor directly affect the climate of polar regions
55 through both greenhouse trapping of radiation and cloud formation processes. Yet,
56 measurements of the low amounts of PWV observed during polar winters are difficult to
57 achieve due to the required high instrumental sensitivity to water vapor [*Cimini et al.*,
58 2007].

59 Although in the last few years new humidity sensors mounted on radiosondes have
60 proven to be a reliable tool for measuring atmospheric humidity in cold and dry
61 conditions [*Miloshevich et al.*, 2006; *Vömel et al.*, 2007], radiosonde observations are

62 limited in daily temporal coverage due to the economic and personnel efforts required for
63 each launch. Moreover, the sonde ascent time limits the time resolution of PWV
64 measurements to no less than 30 minutes, whereas water vapor content in the troposphere
65 can vary significantly on a shorter time scale. Measurements of low amounts of PWV
66 carried out regularly during the day and with a higher time resolution than balloon sondes
67 can provide are necessary, for example, in monitoring upper tropospheric water vapor, its
68 transport and rate of variation, or at sites devoted to atmospheric and astronomic
69 observations within spectral regions (infrared, millimetric and submillimetric
70 wavelengths) where water vapor is the dominant source of atmospheric opacity [e.g.,
71 *Calisse et al.*, 2004].

72 In this study we present a technique for measuring precipitable water vapor using a
73 Ground-Based Millimeter-wave Spectrometer (GBMS) and compare its results with in
74 situ and ground-based remote sensing correlative measurements. Although the technique
75 is not new [see *de Zafra et al.*, 1983], the primary field campaign of the ECOWAR (Earth
76 COoling by WAter vapor Radiation) project [*Bhawar et al.*, 2008] provided a unique
77 opportunity for an intercomparison of accuracy against several other data sets. The
78 ECOWAR campaign took place at Breuil-Cervinia (45.9° N, 7.6° E, elev. 1990 m) and
79 Plateau Rosa (also known as Testa Grigia; 45.9° N, 7.7° E, elev. 3490 m, less than 7 km
80 apart from Breuil-Cervinia), Italy, from 3 to 16 March, 2007. It is part of an experimental
81 program aimed at studying spectral properties of water vapor in its rotational band (17-50
82 μm), with particular attention to the water vapor continuum and line absorption
83 parameters. Observations of spectrally resolved radiances between 100 and 1100 cm^{-1}
84 were realized using two Fourier Transform Spectrometers: the REFIR-PAD (Radiation

85 Explorer in the Far InfraRed - Prototype for Applications and Development) [*Palchetti et*
86 *al.*, 2006] installed at Plateau Rosa and the Fourier Transform Infrared (FTIR)/ABB
87 Bomem [*Esposito et al.*, 2007] installed only a few km away at Breuil-Cervinia.
88 Ancillary measurements of temperature and relative humidity were performed by the
89 University of BASILicata Raman Lidar system (BASIL) [*Di Girolamo et al.*, 2004] based
90 at Breuil-Cervinia, and by Vaisala RS92k radiosondes launched from the same location.
91 The GBMS provided water vapor column measurements and stratospheric ozone profiles
92 from Plateau Rosa. In the next section we describe the GBMS observing technique used
93 to measure atmospheric opacity at mm-wavelengths, in Section 3 the conversion from
94 GBMS opacity measurements to PWV is discussed, while in Section 4 a description of
95 the various correlative water vapor measurements is provided. Section 5 and 6 are
96 dedicated to illustrate results obtained comparing the various data sets and to summarize
97 our work.

98

99 **2. GBMS Observing Technique**

100 The Ground-Based Millimeter-wave Spectrometer (GBMS) measures rotational
101 emission spectra of atmospheric chemical species such as O₃, N₂O, CO and HNO₃, as
102 well as the H₂O continuum, with a spectral window of 600 MHz tunable between
103 approximately 230 and 280 GHz (or 7.7 and 9.3 cm⁻¹). It was designed and built at the
104 Physics and Astronomy Department of the State University of New York at Stony Brook
105 and comprises a front end receiver employing a cryogenically cooled SIS
106 (Superconductor-Insulator-Superconductor) double sideband mixer with an intermediate
107 frequency (IF) of 1.4 GHz. The back end is composed of an Acousto-Optical

108 Spectrometer (AOS) with a spectral band pass of 600 MHz and a maximum resolution of
109 65 kHz [de Zafra, 1995]. The combination of the front and back ends results in the
110 GBMS observation of two superimposed 600 MHz spectral windows whose center
111 frequencies are separated by 2.8 GHz (two times the IF). At the AOS, the full 600 MHz
112 spectrum is read in 40 ms and integrated over time at a computer. Each spectral file is
113 saved after a total time integration of 5 to 15 minutes. In general, observed emission lines
114 are too weak to display a good signal to noise ratio (S/N) within these short time
115 integrations, and spectral files are usually added together off-line to reach a satisfactory
116 S/N ratio. The GBMS observes the emission line of one chemical species at a time,
117 usually for 1 to 5 hours (depending on S/N). Its 600 MHz window must then be tuned to a
118 different frequency interval (in the 230-280 GHz range) in order to observe the emission
119 line of another chemical species.

120 Given the physical parameters of a specific rotational transition, its spectral line
121 shape depends strongly on the vertical concentration profile of the observed species
122 (typically unknown) and on the atmospheric pressure profile (typically known).
123 Therefore, by means of the observed line shape together with pressure and temperature
124 vertical profiles, a mathematical deconvolution process allows finding the emitting
125 molecule's concentration as a function of altitude. The overall spectral band pass and
126 resolution of the GBMS are key elements to determine the 17-75 km altitude range where
127 trace gases concentration can be measured (e.g., see *Muscari et al.* [2007] and references
128 therein). For water vapor, we do not observe an H₂O emission line (e.g., at 183 or 325
129 GHz) but rather the emission from the H₂O continuum existing between emission lines.

130 Therefore, only the integrated column contents can be obtained from GBMS observations
131 of water vapor.

132 During normal data taking operations the GBMS observes radiation from two
133 different directions 75° to 80° apart, switched by a rotating reflective semicircular
134 chopper wheel at $\simeq 1$ Hz frequency (see figure 1). One observing direction is near the
135 zenith (reference beam, or R) while the other points between 10° and 15° above the
136 horizon (signal beam, or S). A dielectric sheet (made of Plexiglas) mounted in the R
137 beam acts as a local partially transparent (and weakly emitting) “grey body” source of
138 broad-band radiation to compensate for the lower total power received from atmospheric
139 emission near the zenith (with a shorter geometrical path length with respect to the S-
140 beam), and allows a power balance to be achieved between the S and R beam directions.
141 Different dielectric sheets are used, depending on atmospheric conditions, with their
142 opacity ranging from ~ 0.2 to 0.8 Nepers at 275 GHz. This power balance is sensed by a
143 phase-sensitive detector synchronized to the rotation of the beam-switching chopper
144 wheel, and maintained by a servo system which adjusts the elevation angle of the S beam
145 if the (S-R) power level deviates from zero. As atmospheric opacity increases or
146 decreases (causing thermal emission from the atmosphere to increase or decrease), the
147 servo mechanism, seeking to maintain power balance in the two beams, will drive the S-
148 beam angle upwards or downwards. The opacity of the dielectric sheet, dependent on its
149 composition and thickness, will determine the equilibrium angles for a given range of
150 atmospheric opacity. Atmospheric radiation from both beam directions enters through a
151 window made of type PP-2 Eccofoam (see figure 1) characterized by a very small opacity
152 at millimeter wavelengths (~ 0.007 Nepers).

153 As long as the emitting layer is optically thin, the signal intensity in S or R will be
 154 proportional to the geometrical path length (hereafter referred to as path length) through
 155 the layer. We define the air mass factor A_x as the dimensionless ratio of the path length
 156 along the x direction divided by the path length in the zenith direction z. For a spherical
 157 atmosphere one obtains

$$158 \quad A_x = \frac{dx}{dz} = (r + z_H) \left/ \left[(r + z_H)^2 - (r + z_0)^2 \cos^2 \theta_x \right]^{1/2} \right., \quad [1]$$

159 where r is the Earth's radius, z_H the mean height of a thin layer above the Earth's
 160 surface, z_0 the altitude of the observer and θ_x is the angle of the observed path along the x
 161 direction measured from the horizontal. For $z_H \ll r$, $A_x \simeq 1/\sin\theta_x$, i.e., the relationship
 162 for a plane parallel atmosphere. In the present case, where the major contribution to
 163 atmospheric opacity arises from water vapor not bound in ice crystals, confined to a layer
 164 of mean height z at most few kilometers above the 3.5 km altitude of Plateau Rosa, the
 165 approximation $A_x \simeq 1/\sin\theta_x$ is within 2% of the full expression for $\theta_x = 10^\circ$ and less than
 166 2% for larger values of θ_x .

167 The following analysis determines the relationship between opacity and S-beam
 168 angle [e.g., *de Zafra*, 1995]. The total power (expressed in temperature units) observed in
 169 the S direction at the frequency ν is:

$$170 \quad T_s(\nu) = T_z^*(\nu) A_s \exp(-A_s \tau_z - \tau_w) + 2T_{CB} \exp(-A_s \tau_z - \tau_w) +$$

$$171 \quad + 2T_w [1 - \exp(-\tau_w)] + 2T_{atm} [1 - \exp(-A_s \tau_z)] \exp(-\tau_w) + T_{rec}(\nu), \quad [2]$$

172 where A_s is the air mass factor in the S direction, $T_z^*(\nu)$ is the integrated signal
 173 intensity due to stratospheric and mesospheric molecular emission in the zenith direction
 174 (which we assume can be transformed to the molecular emission along any other line of

175 sight by multiplying by A_x , i.e., we assume the atmospheric homogeneity), τ_z is the
 176 opacity of the atmosphere in the zenith direction (which, again, we assume can be
 177 transformed to the opacity along any other line of sight by multiplying by A_x). T_{CB}
 178 represents the emission due to the cosmic background, $T_{rec}(\nu)$ is the receiver noise, and
 179 T_w and τ_w are the physical temperature and opacity of the window material, respectively.
 180 T_{atm} is the mean physical temperature of the noise-radiating atmosphere, typically that of
 181 the first few km within the troposphere containing most of the water vapor. It gives rise to
 182 a broad-band signal (no spectral features) with the properties of a uniform noise source
 183 over the 600 MHz spectral window. T_{atm} is obtained using local averaged temperature
 184 and water vapor lapse rates which determine a relationship between T_{atm} and the
 185 temperature monitored at the ground (there is no requirement of high accuracy on T_{atm}
 186 estimates). In equation [2], the frequency dependence is indicated only for those
 187 parameters which can vary significantly within the 600 MHz GBMS band pass. The
 188 remaining parameters (e.g., τ_z) are essentially constant over the band pass although they
 189 can vary over the 230-280 GHz range. Factors of 2 in equation [2] take into account the
 190 use of a double sideband receiver, with equal gain in each sideband. A factor of 2 is
 191 already hidden in the definition for $T_{rec}(\nu)$ for a double sideband receiver. Terms
 192 involving $\exp[-\tau_x]$ represent attenuation of signal by some entity along the path whose
 193 total opacity is τ_x , while terms involving $T_x(1 - \exp[-\tau_x])$ represent emission by the same
 194 entity, assumed to be at a mean physical temperature T_x . An expression similar to
 195 equation [2] gives the output power from the R direction:

$$196 \quad T_R(\nu) = T_z^*(\nu)A_R \exp(-A_R\tau_z - \tau_p - \tau_w) + 2T_{CB} \exp(-A_R\tau_z - \tau_p - \tau_w) +$$

$$\begin{aligned}
197 \quad & +2T_{\text{atm}}[1 - \exp(-A_R \tau_z)] \exp(-\tau_p - \tau_w) + 2T_p[1 - \exp(-\tau_p)] + \\
198 \quad & +2T_w[1 - \exp(-\tau_w)] \exp(-\tau_p) + T_{\text{rec}}(\nu), \quad [3]
\end{aligned}$$

199 where terms have been added to represent signal attenuation by the compensating sheet
200 and its broad-band emission for a given opacity τ_p and physical temperature T_p .

201 During normal data taking operations the S and R output powers averaged over the
202 two 600 MHz sideband spectral windows (whose center frequencies are 2.8 GHz apart)
203 are balanced. Terms due to emission from the Eccofoam window (those in T_w), the
204 cosmic background (T_{CB}) and, when considering spectral averages over the 600 MHz
205 band pass, terms due to molecular emission from stratospheric and mesospheric trace
206 gases (those involving T_z^*) are negligible compared to other terms and we have:

$$\begin{aligned}
207 \quad & T_{\text{atm}}[1 - \exp(-A_S \tau_z)] \exp(-\tau_w) \simeq \\
208 \quad & \simeq T_{\text{atm}}[1 - \exp(-A_R \tau_z)] \exp(-\tau_p - \tau_w) + T_p[1 - \exp(-\tau_p)]. \quad [4]
\end{aligned}$$

209 In the above equation, all terms but τ_z can be derived from independent
210 measurements so that the opacity in the zenith direction remains the only unknown
211 quantity. In fact, all terms but A_S (directly derivable from a measure of θ_S) and τ_z are
212 typically constant over a few hours and equation [4] shows that τ_z can be continuously
213 derived from the record of the angle θ_S at which S and R powers are balanced during
214 observation. Equation [4] can be solved for τ_z by means of an iterative procedure. The
215 accuracy for the resulting τ_z values is estimated at 4.5% by adding in quadrature the
216 uncertainties on θ_S (2.2%), T_{atm} (3.3%) and τ_p (2.2%). T_p is monitored by means of a
217 temperature sensor placed next to the compensating sheet and averaged over 15-minute
218 periods. The resulting uncertainty has a negligible effect on τ_z .

219 There is a second method to measure the opacity in the zenith direction, τ_z , and this
 220 involves measuring the sky brightness temperature in the S direction averaged over the
 221 600 MHz band pass, T_{Ssky} . This is obtained by considering the total power of eq. [2]
 222 (averaged over both sidebands) without the receiver noise temperature T_{rec} and the
 223 Eccofoam window terms. Again, neglecting very small contributions from stratospheric
 224 molecular line emission and from the cosmic background, T_{Ssky} is given by the
 225 expression:

$$226 \quad T_{\text{Ssky}} = T_{\text{atm}} [1 - \exp(-\tau_z A_S)]. \quad [5]$$

227 Considering that the portion of the air mass factor affecting atmospheric opacity lies
 228 within a few km of the observer, where a plane parallel approximation for path length is
 229 quite accurate, we may take $A_S \sim 1/\sin\theta_S$. Then, solving for the zenith opacity τ_z leads to

$$230 \quad \tau_z = -\sin\theta_S \cdot \ln \left\{ 1 - T_{\text{Ssky}} / T_{\text{atm}} \right\}, \quad [6]$$

231 where T_{Ssky} can be evaluated from locally measurable quantities by means of the
 232 GBMS calibrating procedure which is periodically carried out by the operator [*de Zafra*,
 233 1995; *Parrish et al.*, 1988].

234 This second procedure for the evaluation of τ_z is carried out by interrupting the
 235 normal data taking operations and performing a so called “sky dip” (see, e.g., *Han and*
 236 *Westwater* [2000]). The operation consists of manually moving the mirror which
 237 determines the S direction of observation within the range allowed by the window
 238 opening ($\sim 10^\circ$ - 15° above the horizontal) at $\sim 0.5^\circ$ steps, measuring the output power at
 239 each step by means of the GBMS, and estimating τ_z at each step using eq. [6]. If water
 240 vapor density is independent of viewing direction (atmospheric homogeneity) and T_{atm}

241 has been estimated correctly, the derived values of τ_z will be in good agreement with one
242 another and their average value will result in an estimate of zenith opacity. A further
243 check on the horizontal homogeneity of the water vapor field is performed by measuring
244 τ_z also at the zenith (after removing the compensating sheet normally placed in the R
245 beam direction) and verifying its consistency with sky dip measurements. Using this
246 technique, the uncertainty on each single measurement of τ_z (i.e., eq. [6] applied to each
247 single 0.5° mirror step) is estimated at 15%, with the largest relative error contribution of
248 14% coming from the uncertainty on the measurement of T_{ssky} by means of the GBMS
249 calibrating procedure. However, taking the mean of the ~ 11 τ_z measurements from the
250 same sky dip results in a relative uncertainty on the mean τ_z of 5.1%. Although SIS
251 mixers are sensitive to the polarization of the incident radiation, potential spurious
252 changes of polarization (e.g., those caused by changing the orientation of the S beam
253 mirror [e.g., *Renbarger et al.*, 1998]) are negligible compared to the unpolarized
254 tropospheric signal observed by the GBMS between 230 and 280 GHz.

255 Results from the two different methods described above are compared in the next
256 section (see figure 4), after discussing their conversion to PWV. Overall, the method
257 based on balancing S and R output powers is preferred over the sky dip mainly because
258 the former gives continuous measurements of opacity during normal observing of
259 rotational emission lines. This means that τ_z measurements do not require the presence of
260 an operator and each measurement can in principle be obtained with ~ 1 -minute temporal
261 resolution (allowing for the average of a large number of chopper rotations at 1 Hz
262 frequency). The sky dip technique is instead carried out manually by the operator in about
263 15 minutes. Although the sky dip method takes somewhat into account potential spatial

264 non-homogeneity by averaging over a range of directions (albeit limited), at the same
265 time it can be more affected by water vapor temporal variations with respect to the power
266 balance method.

267 The double sideband design of the GBMS is the limiting factor for the spectral
268 resolution of τ_z measurements. Emission terms present in equations [4] and [6] are
269 averages over two superimposed 600 MHz spectral windows (the upper and lower side
270 bands) whose center frequencies are separated by 2.8 GHz, giving rise to an overall 4
271 GHz resolution.

272

273 **3. From GBMS opacity measurements to precipitable water vapor**

274 In the 230-280 GHz spectral region the atmospheric emission arises almost entirely
275 from water vapor continuum in cloud-free skies, with second order contributions from
276 molecular nitrogen and oxygen (e.g., see fig.1 in *Klein and Gasieweski* [2000]), and
277 rotational spectra of trace gases contribute a negligible amount to the total brightness
278 temperature observed by the GBMS, except for a few of the strongest O₃ emission lines.
279 The conversion from the atmospheric opacity τ_z (measured at the various frequencies
280 where the GBMS is operated) to water vapor column content can hence be obtained by
281 means of the linear relation:

$$282 \text{PWV} = [\tau_z(\lambda) - \tau_{\text{dry}}(\lambda)] \alpha(\lambda). \quad [8]$$

283 Factors $\alpha(\lambda)$, which convert to PWV the opacity due to H₂O only, have been
284 obtained from measurements carried out by *Zammit and Ade* [1981], while $\tau_{\text{dry}}(\lambda)$ values
285 at Plateau Rosa are obtained using the radiative transfer (RT) model discussed by
286 *Liljegren et al.* [2005]. Although we use the model scheme of *Liljegren et al.* [2005] only

287 to estimate $\tau_{\text{dry}}(\lambda)$, we note that $\alpha(\lambda)$ and $\tau_{\text{dry}}(\lambda)$ values can differ significantly depending
288 on the RT model considered. However, while differences on $\tau_{\text{dry}}(\lambda)$ have a limited effect
289 on estimates of PWV, differences in modelled $\alpha(\lambda)$ factors can have a much larger
290 impact. Hence our choice of relying on $\alpha(\lambda)$ values from the experimental data set of
291 *Zammit and Ade* [1981] rather than adopting results from any of the RT models discussed
292 in the literature (see below).

293 *Zammit and Ade* [1981] derived experimental relationships to correlate τ_z with PWV
294 at selected frequencies between 212 and 408 GHz, with a spectral resolution of 9.6 GHz.
295 In order to derive $\alpha(\lambda)$ values at the GBMS frequencies of observation, a linear
296 interpolation between the two closest frequencies investigated by *Zammit and Ade* [1981]
297 was performed, as shown in figure 2. We implemented these interpolations also using
298 higher degree polynomials but obtained no substantial difference in the comparisons
299 results shown in Section 5. Furthermore, matching values of PWV are obtained from
300 GBMS opacity measurements at different frequencies when they are carried out within a
301 short time span (less than 15 minutes), suggesting that the conversion factors used are at
302 least consistent with one another. This check can be performed when the GBMS is
303 retuned in frequency in order to carry out daily measurements of different molecular
304 species. Often, for example, the GBMS is first set to observe the CO line at 230.5 GHz
305 and then moved in frequency to O₃ at 276.9 GHz, therefore measuring τ_z and PWV at
306 frequencies $\simeq 46$ GHz apart within a short time span.

307 The choice of using $\tau_{\text{dry}}(\lambda)$ values from *Liljegren et al.* [2005] originated from
308 comparing factors $\alpha(\lambda)$ from *Zammit and Ade* [1981] with results from 5 different RT
309 models [*Liebe and Layton*, 1987; *Liebe et al.*, 1993; *Rosenkranz*, 1998, 1999, and 2003;

310 *Liljegren et al.*, 2005]. We found that modelled $\alpha(\lambda)$'s from *Liljegren et al.* [2005] had
311 the closest match to the *Zammit and Ade* [1981] experimental data (the former values
312 being smaller by 6-9% at the GBMS observing frequencies) and chose their modelled
313 $\tau_{\text{dry}}(\lambda)$ values for consistency. In figure 3, $\tau_{\text{dry}}(\lambda)$ results from the 5 different RT models
314 are plotted. Their 1σ standard deviation at each frequency (~ 0.003 mm, see figure 3) is
315 used as estimated uncertainty on the correspondent $\tau_{\text{dry}}(\lambda)$ value from *Liljegren et al.*
316 [2005].

317 As discussed in *Hewison et al.* [2006], *Liljegren et al.* [2005] proposed few
318 modifications to previous millimeter-wave propagation models (e.g., those discussed in
319 *Liebe and Layton* [1987] and *Rosenkranz* [1998 and 1999]) following recent results
320 obtained from spectral atmospheric measurements. These modifications can be
321 summarized in the use of parameters from the HITRAN database [*Rothman et al.*, 2003]
322 and the MT_CKD continuum [*Clough et al.* 2005].

323 Uncertainties on GBMS PWV values are estimated by propagating the uncertainties
324 on τ_z (see previous section), on $\tau_{\text{dry}}(\lambda)$, and the $\simeq 1.9\%$ error on $\alpha(\lambda)$'s (see *Zammit and*
325 *Ade* [1981]). This results in PWV uncertainties that vary from $\sim 5\%$ (for large PWV) to
326 $\sim 10\%$ (for the smallest PWV observed), with very little dependence on the specific
327 technique used to measure τ_z (i.e., sky dip or power balance).

328 In figure 4, PWV values obtained from GBMS opacity measurements carried out
329 using the two different techniques at the same frequency within a short time span (less
330 than 15 minutes) are compared. Figure 4 shows that a very good agreement between the
331 two sets of GBMS PWV values exists, with a percentage value of the root mean square of
332 the difference (RMSD%) between the two data sets of 6.6%. Here we indicate with

333 RMSD% the quantity
$$\text{RMSD}\% = \sqrt{\sum_i^N \frac{1}{N} \left[\frac{(x_i - y_i)}{x_i} 100 \right]^2}$$
, with x_i and y_i indicating the
334 two sets of measurements being compared. The RMSD% represents a measure of the
335 averaged discrepancy between two data sets, with the squared differences between pairs
336 of data points insuring that positive and negative differences do not partly cancel out. Its
337 comparison with data sets uncertainties indicates the level of agreement between the two
338 sets of measurements.

339 In figure 5 the time series of precipitable water vapor values estimated by GBMS
340 during the ECOWAR field campaign is shown. All values are obtained using the power
341 balance method (see Section 2). Measurements were carried out during the entire period
342 of the ECOWAR campaign except in cases of poor weather conditions or occasional
343 equipment malfunctioning. Although measurements from instruments participating to the
344 ECOWAR campaign are used to characterize the environmental conditions occurring
345 during GBMS operations, GBMS PWV values do not depend on data from the other
346 PWV sets of measurements presented in this intercomparison study.

347 Lidar and radiosonde measurements did provide the necessary information for
348 evaluating potential influences of ice clouds on radiances measured at mm-waves [e.g.,
349 *Evans and Stephens, 1995; Liu and Curry, 1998*]. Lidar measurements were used to
350 detect the presence of clouds and, together with radiosonde relative humidity data,
351 provided information on the cloud particles phase, which is indicated to be always solid
352 at the time of the GBMS observations discussed here. Lidar measurements of cirrus
353 clouds optical depth at 532 nm (τ_{532}) provided a means for estimating an upper limit on
354 ice water path (IWP) [*Liou, 1992*]. Based on Lidar measurements of τ_{532} less than 1 (IWP

355 at most ~ 0.04 mm) at the time of GBMS observations, we find that the occasional
356 presence of cirrus clouds in the GBMS field of view can affect the observed T_{atm} by
357 amounts that are well within its 3.3% uncertainty (e.g., see figure 8 in *Cimini et al.*
358 [2007]).

359

360 **4. Correlative water vapor measurements**

361 **4.1 The RS92k sonde**

362 During the 14-day long ECOWAR field campaign, 34 Vaisala RS92k radiosonde
363 units were launched from Cervinia and measured vertical profiles of atmospheric
364 temperature and water vapor. 2 to 4 sondes were launched each day from March 4 to
365 March 15, except on March 6 when meteorological conditions prevented any data-taking
366 from ground-based instruments. Data from 27 sondes were used in this study, with only 7
367 sondes launched during daytime ($\text{SZA} < 85^\circ$). The sonde ascending time from the
368 Cervinia field station (1990 m altitude) to $\simeq 10$ km altitude was approximately 20-25
369 minutes.

370 The Vaisala RS92k radiosonde is equipped with temperature, pressure and humidity
371 sensors (see technical data in table 1 [*Jauhainen and Lehmuskero, 2005*]), while altitude
372 information is obtained from the application of the hypsometric equation. Type k of the
373 Vaisala radiosonde RS92 family is not equipped with a wind sensor. The advanced
374 HUMICAP humidity sensor is composed of two thin-film capacitors that are alternatively
375 heated in order to avoid ice formation on them at low temperatures and condensation of
376 water vapor during sounding. The advanced HUMICAP sensor works on the principle of
377 absorption of water molecules into the thin-film surface. Absorption of other molecules

378 can contaminate the sensor and produce a bias in humidity measurements. In order to
379 reduce this potential bias, a reconditioning procedure was performed on the radiosondes
380 by heating the humidity sensor just before sounding therefore removing the contaminants
381 from the sensor surface [Hirvensalo *et al.*, 2002; Währn *et al.*, 2004]. The reconditioning
382 procedure was performed by using the Vaisala Ground Check Set GC25 that reads the
383 original calibration coefficients automatically to assure that chemical contaminants have
384 been removed.

385 The RS92 radiosondes are commercially available since October 2003. Their
386 operational characterizations took place in November 2003, during the Atmospheric
387 Infrared Sounder (AIRS) Water Vapor Experiment-Ground (AWEX-G) [Miloshevich *et al.*,
388 2006], and in July 2005, during the observation campaign Ticosonde 2005 [Vömel *et al.*,
389 2007]. During these campaigns, water vapor measurements by sondes RS92 were
390 compared to simultaneous measurements carried out using the Cryogenic Frostpoint
391 Hygrometer and, only during AIRS/AWEX-G, also using different radiosonde types.
392 These studies pointed out that the humidity sensor mounted on RS92 sondes is the most
393 accurate among those installed in four types of radiosonde currently produced by Vaisala
394 (RS80-A, RS80-H, RS90, RS92). The RS92 model uses the same polymer humidity
395 sensor employed in the older RS80-H but the size and thickness of the polymer layer is
396 smaller, improving the sensor response time at low temperature [Miloshevich *et al.*, 2004;
397 Miloshevich *et al.*, 2006]. Moreover, the calibration process is more accurate than in
398 previous models [Paukkunen *et al.*, 2001]. The main problem for RS92 sondes lies in the
399 lack of a radiation shield (present in RS80-H), which makes the RS92 sensor more
400 susceptible to solar heating and produces a strong solar radiation dry bias [Vömel *et al.*,

401 2007]. However, the magnitude of this radiation dry bias and its dependance on SZA is
402 not yet well established [e.g., *Miloshevich et al.*, 2004 and 2006; *Vömel et al.*, 2007;
403 *Rowe et al.*, 2008]. In their figure 10, *Rowe et al.* [2008] plot several estimates of the
404 radiation dry bias obtained in recent studies. From their figure 10, we deduce that an 8%
405 dry bias could be affecting the 7 daytime RS92k sondes used in this study and therefore
406 applied this correction to the corresponding PWV values. Following the results depicted
407 by *Vömel et al.* [2007] in their figure 9, we assign an accuracy of 5% to PWV
408 measurements obtained using RS92 sondes.

409 In performing the comparison between GBMS and RS92k sonde PWV
410 measurements (see Section 5), radiosonde values were calculated by integrating water
411 vapor concentrations from the pressure level of Plateau Rosa up to 10 km altitude.
412 Integrating sonde measurements up to 15 km produces negligible differences. The
413 corresponding GBMS PWV value is obtained from GBMS measurements carried out
414 while radiosondes ascent from 3.5 km to 10 km altitude.

415

416 **4.2 Raman Lidar BASIL**

417 Lidar measurements were performed by the University of BASILicata Raman Lidar
418 system (BASIL). The system was substantially upgraded prior the ECOWAR
419 measurement campaign with the implementation of an additional receiver (developed at
420 the University of Roma "La Sapienza") dedicated to the detection of echoes from the
421 lowest altitude levels. The major feature of BASIL is represented by its capability to
422 perform high-resolution and accurate measurements of atmospheric temperature, both in
423 daytime and night-time, based on the application of the rotational Raman Lidar technique

424 in the UV [*Di Girolamo et al.*, 2004]. Besides temperature, BASIL is capable of
425 providing measurements of particle backscatter at 355, 532 and 1064 nm, particle
426 extinction and depolarization at 355 and 532 nm, and water vapor mixing ratio vertical
427 profiles both in day-time and night-time. This wide range of measured parameters makes
428 this system particularly suited for the study of meteorological processes and the
429 characterization of aerosol and cloud microphysical properties.

430 Vertical and temporal resolutions of raw data are 30 m and 1 minute, respectively.
431 However, in order to reduce signal statistical fluctuations, time integration together with
432 vertical profile smoothing are applied to the data. For a time resolution of 5 minutes and a
433 vertical resolution of 150 m, daytime measurements uncertainties at 2 km altitude are
434 typically 5% for the particle backscattering coefficient (at all wavelengths), 20% for the
435 particle extinction coefficient, 10% for water vapor mixing ratio values and 2 K for
436 temperature values. Relative uncertainties for nighttime measurements at 2 km are half as
437 much as daytime measurements for all parameters.

438 BASIL calibration for water vapor measurements was achieved using simultaneous
439 and co-located radiosonde observations. Once calibrated, BASIL water vapor
440 measurements represented a key contribution to the field campaign by providing
441 continuous vertical profiles of water vapor. The calibration constant was determined
442 comparing BASIL and radiosondes water vapor mixing ratio values in the lowermost
443 kilometer above Cervinia using all 34 launches performed during ECOWAR. The
444 selection of the lowermost kilometer ensures that both instruments were sampling the
445 same air mass during the calibration procedure. The consideration of all available
446 radiosondes for the determination of the calibration constant used in this intercomparison

447 effort prevents the dependence of a single Lidar vertical profile from the simultaneous
448 radiosonde profile.

449 The use of a very compact optical design reduces significantly the differences
450 between the overlap functions of the H₂O and N₂ Raman signals used to estimate water
451 vapor mixing ratio. Nevertheless, differences in the lower 1500 m between the two
452 overlap functions may, in principle, be quantified through the application of the “N₂
453 calibration procedure” [Whiteman *et al.*, 1992], consisting in the use of N₂ Raman filters
454 in both the H₂O and N₂ channels. This calibration procedure was applied during
455 ECOWAR at the beginning and end of each measurement session. However, small
456 discrepancies have been revealed between overlap-corrected lidar and co-located
457 radiosonde measurements, probably resulting from polarization effects originated in the
458 dichroic beamsplitters used for the partitioning of the signals. Hence, an independent
459 estimate of the overlap function ratio was obtained from the comparison of lidar and co-
460 located radiosonde measurements. This procedure was applied to all radiosonde launches
461 available during each measurement session and a mean overlap function ratio was
462 determined for each measurement session. Variability of the overlap function during each
463 measurement session was found to be very limited, with a very reduced impact on the
464 PWV uncertainty (estimated to not exceed 3-5 %).

465 Water vapor Lidar measurements used in this work are integrated over 10 minutes
466 and have a vertical resolution of 150 m from the ground (\simeq 2 km altitude) to 5 km and of
467 300 m above 5 km altitude. BASIL PWV values compared to GBMS values in the next
468 section are obtained using only nighttime measurements. BASIL water vapor vertical
469 profiles were integrated in the altitude region 3.5-10 km altitude. Although a 50%

470 maximum uncertainty in mixing ratio values is reached at the uppermost altitude levels,
471 this has little impact on total PWV estimates. The resulting BASIL PWV values have an
472 estimated relative uncertainty of only 5%.

473 In Figure 6, a comparison between values of PWV obtained from simultaneous
474 radiosonde and Lidar measurements is shown. Both sets of PWV values are computed
475 integrating the water vapor content from 3.5 to 10 km altitude, as previously described,
476 for consistency with comparisons discussed in section 5. Since BASIL calibration is
477 based on RS92k humidity measurements between 2 and 3 km altitude, while all PWV
478 values refer to the 3.5-10 km altitude range, concurrent Lidar and sonde PWV
479 measurements can, in practice, differ. Setting the upper limit for the PWV integration at
480 an altitude of 10 km reduced the number of concurrent measurements that could be used
481 for this comparison, since not all of the 34 radiosondes launched or the corresponding
482 Lidar profiles reached 10 km altitude. Figure 6 shows that a good agreement between the
483 two sets of PWV values exists, with a RMSD% of 8.5%.

484 Moreover, we quantified how many concurrent Lidar and sondes measurements are
485 consistent within their uncertainties. In other words, defining $\Omega_i = \Delta x_i + \Delta y_i - |x_i - y_i|$,
486 being x_i, y_i a pair of concurrent measurements from the two data sets and $\Delta x_i, \Delta y_i$ the
487 corresponding 1σ uncertainties, we find that in 87.5% of the cases (15 out of 17) Ω_i is
488 positive, i.e., the two measured PWV values are consistent within their uncertainties.

489

490 **4.3 REFIR-PAD**

491 REFIR-PAD (Radiation Explorer in the Far InfraRed - Prototype for Applications
492 and Development) is a Fourier transform spectroradiometer measuring the spectrum of

493 the downward longwave radiation (DLR) emitted from the atmosphere in the wide
494 spectral range from 100 to 1400 cm^{-1} with a maximum resolution of 0.25 cm^{-1} . It is a
495 prototype developed as a field demonstrator of a space-borne instrument designed for the
496 characterization of the Earth's radiation budget in the far infrared region [*Palchetti et al.*,
497 2005; *Bianchini et al.*, 2006]. REFIR-PAD was specifically designed with the
498 requirements of reliability, light weight (55 kg) and low power consumption (about 50 W
499 average) to fly on-board stratospheric balloons [*Palchetti et al.*, 2006], but its extremely
500 flexible design makes it suitable also for ground-based observations with only minor
501 changes required [*Bianchini et al.*, 2007].

502 The instrument uses an innovative optical design [*Carli et al.*, 1999] with two input
503 ports and two output channels. One input port is used for looking at the unknown scene to
504 be measured and the second one for looking at a reference blackbody source, which
505 allows the access and the control of the instrument self-emission. At the output ports,
506 signals are acquired with two room temperature DLATGS (deuterated L-alanine-doped
507 triglycene sulfate) pyroelectric detectors.

508 During the ECOWAR campaign, REFIR-PAD was operated in the 100-1100 cm^{-1}
509 spectral range with 0.5 cm^{-1} spectral resolution and an acquisition time of 64 s for a single
510 scan [*Bhawar et al.*, 2008]. Measurements contain the spectral signature of the pure
511 rotational water vapor band and can be used for the characterization of the water vapor
512 content in the atmosphere and in particular for the measurement of PWV.

513 Measured DLR spectra are analyzed through a retrieval code based on the ARTS
514 forward model [*Buehler et al.*, 2005] and a χ^2 minimization algorithm based on the
515 MINUIT function minimization routines supplied by CERN [*James et al.*, 1994]. The

516 number of degrees of freedom (DOF) in the acquired data is determined through the
517 analysis of the Jacobian of water vapor and temperature observations [*Bianchini et al.*,
518 2007]. To this purpose, first of all the Jacobian matrix is calculated as a function of
519 wavenumber and altitude. Calculations are performed for zenith sounding, operating
520 conditions at Plateau Rosa, and with a midlatitude-winter standard atmosphere. The
521 spectral range used for analysis is 305-650 cm^{-1} , the altitude range is from the ground to
522 18 km altitude.

523 Singular values decomposition (SVD) is then applied to the Jacobian matrix. The
524 relative magnitude of the resulting eigenvalues is used as a criterion to choose fitted
525 parameters. The highest value is obtained for the first water vapor eigenvector, the second
526 and third eigenvalues of water vapor are $\sim 3.5\%$ and $\sim 0.4\%$, respectively, of the first
527 eigenvalue. For the atmospheric temperature, the first and second eigenvalues are 2.7%
528 and 0.1% , respectively, of the first water vapor eigenvalue. As expected, the far-infrared
529 spectral range shows a high sensitivity to water vapor atmospheric content. Given the
530 $\sim 1\%$ average uncertainty on the measured radiance, we deduce a $\text{DOF} = 3$, with two DOF
531 for water vapor and one for temperature.

532 The chosen parameter set includes two points from the water vapor profile, about 1
533 km and 2 km above the measuring station of Plateau Rosa, and the temperature
534 corresponding to the lowest water vapor fitted point. While the two values of the water
535 vapor vertical profile are being adjusted by the minimization algorithm, the rest of the
536 profile is assumed to have the shape of the midlatitude-winter standard water vapor
537 profile and is rescaled accordingly.

538 Practically, these two points represent two partial water vapor column contents that
539 added together give the PWV. The midlatitude-winter standard atmosphere temperature
540 profile is instead rescaled according to the fitted temperature value and to the tropopause
541 temperature of the standard profile. A very simple cloud model, based on the Rayleigh
542 scattering approximation, is used to run retrievals in the presence of a thin cloud cover.
543 The cloud geometry (layer altitude and thickness, cloud particles phase) is inferred from
544 meteorological data, while the ice or liquid water content is fitted as an additional
545 parameter. It is worth mentioning that REFIR-PAD measurements are always carried out
546 when no visible clouds are present, so clouds affecting REFIR-PAD spectral
547 measurements can only be subvisible cirrus clouds. Furthermore, water vapor and cirrus
548 clouds have different effects on REFIR-PAD measurements: while clouds produce the
549 effect of a reduced transparency in the windows between water vapour lines, leaving
550 absorption lines unaffected, water vapor variations show up in absorption lines. These
551 two different effects are not correlated and are adjusted independently (using different
552 parameters) in the REFIR-PAD PWV retrieval procedure. Only two REFIR-PAD PWV
553 data points used in this study are obtained in the presence of subvisible cirrus clouds, and
554 they are relative to measurements carried out on March 4 and 9.

555 Since the first water vapor eigenvalue is more than one order of magnitude larger
556 than the second water vapor and temperature eigenvalues, and the first water vapor
557 eigenvector accounts for most of the total integrated water column, it follows that PWV is
558 the physical parameter to which REFIR-PAD zenith-looking spectra show the largest
559 sensitivity. This is taken into account in the estimation of the uncertainty on PWV values.
560 Since most of the uncertainty on the two retrieved water vapor mixing ratio values comes

561 from the correlation between them, which does not affect the total water vapor column, a
562 second data analysis run is performed with only one fitted water vapor parameter. As
563 expected from the SVD analysis described above, this procedure gives total column
564 values that are over- or underestimated by up to a few percent (depending on atmospheric
565 conditions), but their relative error does not have any contribution from the correlation
566 between the two water vapor levels.

567 Following the analysis described above, a 5% average relative uncertainty is
568 assigned to measured PWV values. This 5% value encompasses more than 90% of the
569 measurement errors obtained, with no visible dependence on PWV values.

570 In this work, we use REFIR-PAD spectral measurements integrated over $\simeq 5$
571 minutes and retrieve a PWV value from each 5-minute integration. In particular, REFIR-
572 PAD PWV values reported in the following section are averages of 3 PWV retrievals
573 obtained from 3 successive 5 minute spectral integrations carried out concurrently with a
574 sonde's ascent from 3.5 to 10 km altitude. The estimated uncertainty of 5% assigned to
575 REFIR-PAD PWV values does not take into account the averaging procedure over 3
576 successive PWV retrievals and is therefore to be considered a rather conservative
577 accuracy assessment.

578

579 **5. Comparisons results**

580 In this section we compare precipitable water vapor values estimated using the
581 GBMS with those obtained from the three additional sets of data described in the
582 previous section and obtained during the March 2007 ECOWAR field campaign.
583 Comparisons are shown in three different scatterplots (Figures 7a, 7b, and 7c). GBMS

584 estimates are those obtained using the power balance method (see Section 2). Although
585 this technique can in principle provide opacity measurements with a temporal resolution
586 of $\simeq 1$ minute, in practice GBMS raw measurements are integrated over 15 minutes
587 during regular data taking. During the ECOWAR campaign we also carried out 5 minute
588 integrations at frequencies where no emission line of stratospheric and mesospheric
589 chemical species could be detected and observations were devoted to opacity (and
590 therefore PWV) measurements only.

591 GBMS PWV measurements are in good agreement with the other three data sets
592 displaying RMSD% values ranging from 9% to 9.6%. Furthermore, Ω_i values (see
593 section 4.2) are positive in 78.5% of the cases for GBMS/Lidar, 75% of the cases for
594 GBMS/REFIR comparisons and in 86.9% of the cases for the GBMS/sonde comparison.
595 The statistics reported in Figure 7 provide details for each comparison. In particular, the
596 comparison between GBMS and BASIL data (figure 7b) is based on a considerable
597 number of correlation points and allows an interpretation of slope and intercept values of
598 the linear fit to the scatterplot. A slope of 0.99 (± 0.02) indicates that the sensitivity of the
599 two instruments to variations of PWV is within 1% ($\pm 2\%$) of one another. Alternatively,
600 we can indicate slope and intercept values of the linear fit as measures of percentage and
601 absolute systematic differences between GBMS and BASIL PWV measurements. This
602 would lead to an estimation of percentage and absolute systematic differences of 1% (\pm
603 2%) and 0.03 (± 0.02) mm, respectively.

604 Although the same analysis can in principle be applied also to the comparisons
605 illustrated in figures 6, 7a, and 7c, a much smaller number of data points is available in
606 these cases. For these correlation plots, we restrain from drawing any conclusion based

607 on the characteristics of the linear fits and consider RMSD% values the most accurate
608 measure of the agreement between the data sets.

609 The four comparisons illustrated in figures 6 and 7 are not based on measurements
610 all carried out at the same time. Each comparison relies, in principle, on separate pairs of
611 measurements (i.e., each pair carried out at different times with respect to the other
612 comparisons). In particular, the GBMS/lidar correlation is based on many points (31 out
613 of 42) unique to the GBMS/lidar correlation and not available to the other three. This
614 explains the apparent inconsistency among the slopes that characterize the lidar/sonde,
615 GBMS/lidar, and GBMS/sonde correlations (see figure 7).

616 A systematic GBMS high bias appears to be present for measurements carried out on
617 March 13 and marked in figure 7. During this day only, GBMS PWV are consistently
618 larger than values from all other data sets by up to 16%. Although a large unaccounted
619 inaccuracy in GBMS opacity observations for March 13 cannot be ruled out, this result,
620 unique for March 13, suggests that a peculiar meteorological condition possibly occurred
621 on this day. Particle backscatter Lidar measurements (not shown) indicate that a large
622 amount of Saharan dust particles arrived over Cervinia on March 12, reaching altitudes as
623 high as 8 km. Concurrently, the GBMS PWV time series displayed in Figure 5 shows a
624 rapid increase of the PWV (day 71, March 12) from 0.6 mm at 9:30 am to 1.7 mm at 7
625 pm, suggesting that the advection of lower tropospheric air from the Saharan region
626 brought both desert aerosols and a large concentration of water vapor to the Western
627 Alps. On March 13, the Saharan aerosol layer slowly faded away and its top altitude was
628 observed by BASIL at 4.5 km in the morning, lowering to $\simeq 3$ km in the late
629 evening/night, while the GBMS PWV from Plateau Rosa stayed stable between 1.7 and 2

630 mm (see Figure 5). Since the GBMS opacity measurements from Plateau Rosa are based
631 on observations at 10-15 degrees above the horizon looking almost directly North, while
632 Cervinia is South-West of Plateau Rosa, during the particular transitional conditions of
633 March 13 the GBMS might have sampled air masses with a different water vapor content
634 relative to BASIL and the RS92k sondes, based at Cervinia, and even with respect to
635 REFIR-PAD observing in the zenith direction from Plateau Rosa.

636

637 **6. Summary**

638 Low amounts of PWV are difficult to measure accurately due to the necessary high
639 instrumental sensitivity to water vapor, but are important for climate studies, in particular
640 for correctly modeling longwave fluxes in polar regions, for increasing our basic
641 knowledge about concentration and transport of water vapor in the upper troposphere and
642 in polar regions, and for providing ancillary information to atmospheric and astronomy
643 observations performed at infrared, millimetric and submillimetric wavelengths. In this
644 study we describe a technique for measuring very low column contents of water vapor
645 (below 4 mm of PWV) using observations of atmospheric opacity at frequencies between
646 230 and 280 GHz. Although the technique was developed by *de Zafra et al.* [1983], here
647 we present the first accurate intercomparison of these measurements with in situ and
648 ground-based correlative measurements. Furthermore, we use the state of the art radiative
649 transfer model in the millimeter wavelength range by *Liljegren et al.* [2005] in order to
650 take into account the opacity due solely to the dry atmosphere (not negligible under very
651 low PWV conditions) with a resulting improvement with respect to the qualitative PWV
652 estimates displayed in *de Zafra et al.* [1983] and *Parrish et al.* [1987].

653 We discuss the two methods used to measure atmospheric opacity using the GBMS,
654 the beam balancing and the sky dip procedures, and the scatterplot displayed in figure 4
655 shows that the two methods produce the same results with similar accuracies. In order to
656 obtain PWV amounts, we have first removed the component due to the dry atmosphere
657 from the GBMS atmospheric opacity measurements and then applied a scale factor
658 obtained from measurements reported in *Zammit and Ade* [1981] to convert to PWV the
659 opacity due to H₂O only.

660 The intercomparison between the GBMS data set and simultaneous PWV
661 observations obtained with Vaisala RS92k radiosondes, a Raman Lidar, and an IR
662 Fourier Transform Spectrometer is presented in Section 5. These sets of concurrent
663 measurements were carried out during the primary field campaign of the ECOWAR
664 project which took place on the Western Italian Alps from 3 to 16 March, 2007.

665 GBMS PWV measurements are in good agreement with the other three data sets
666 displaying percentage values for the root mean square of the difference between
667 observations ranging from 9% to 9.6% (see figure 7). Given the considerable number of
668 data points available for the comparison between GBMS and Lidar measurements, for
669 this case we can provide an interpretation of slope and intercept values of the linear fit to
670 the scatterplot (figure 7b) which suggests very small, if any, systematic differences
671 between the two data sets. The slope indicates a percentage systematic difference of 1%
672 ($\pm 2\%$), while the intercept suggests an absolute systematic difference of 0.03 (± 0.02)
673 mm.

674 Only on March 13 were GBMS PWV values consistently larger than those from all
675 other data sets by up to 16%. Although a large unaccounted inaccuracy in GBMS opacity

676 observations carried out on March 13 cannot be ruled out, we discuss the possibility that
677 a peculiar meteorological condition has taken place on this day.

678

678

679 **References**

- 680 Bhawar, R., G. Bianchini, A. Bozzo, M. Cacciani, M. R. Calvello, M. Carlotti, F.
681 Castagnoli, V. Cuomo, P. Di Girolamo, T. Di Iorio, L. Di Liberto, A. di Sarra, F.
682 Esposito, G. Fiocco, D. Fuà, G. Grieco, T. Maestri, G. Masiello, G. Muscari, L.
683 Palchetti, E. Papandrea, G. Pavese, R. Restieri, R. Rizzi, F. Romano, C. Serio, D.
684 Summa, G. Todini, and E. Tosi (2008), Spectrally Resolved Observations of
685 Atmospheric Emitted Radiance in the H₂O Rotation Band, *Geophys. Res. Lett.*, 35,
686 L04812, doi:10.1029/2007GL032207, 2008.
- 687 Bianchini, G., L. Palchetti, and B. Carli (2006), A wide-band nadir-sounding
688 spectroradiometer for the characterization of the Earth's outgoing long-wave radiation,
689 *Proceedings of SPIE, Systems and Next-generation Satellites XII*, 6361, R. Meynard, S.
690 P. Neeck, H. Shimoda, 63610A.
- 691 Bianchini, G., L. Palchetti, and A. Baglioni (2007), Far infrared spectrally resolved
692 broadband emission of the atmosphere from Monte Morello and Monte Gomito near
693 Florence, *Proceedings of SPIE, Remote Sensing of Clouds and the Atmosphere*, vol.
694 6745, 6745-61, Florence, 17-19 September 2007.
- 695 Buehler, S. A., P. Eriksson, T. Kuhn, A. von Engeln, and C. Verdes (2005), ARTS, the
696 atmospheric radiative transfer simulator, *J. Quant. Spectrosc. Radiat. Transf.*, 91, 65-
697 93.
- 698 Calisse, P. G., M. C. B. Ashley, M. G. Burton, M. A. Phillips, J. W. V. Storey, S. J. E.
699 Radford, and J. B. Peterson (2004), Submillimeter site testing at Dome C, Antarctica,
700 *Publ. Astron. Soc. Aust.*, 21, 1 – 18.

701 Carli, B., A. Barbis, J.E. Harries, and L. Palchetti (1999), Design of an efficient
702 broadband far-infrared Fourier-transform spectrometer, *Appl. Opt.*, 38, 3945-3950.

703 Cimini D., E. R. Westwater, A. J. Gasiewski, M. Klein, V. Y. Leuski, J. C. Liljegen
704 (2007), Ground-based millimeter- and submillimeter-wave observations of low vapor
705 and liquid water contents, *IEEE Trans. Geosci. Remote Sens.*, 45, 2169-2180.

706 Clough S. A., Iacono M. J., Moncet J.-L. (1992), Line-By-Line Calculations Of
707 Atmospheric Fluxes And Cooling Rates - Application To Water-Vapor, *J. Geophys.*
708 *Res.*, 97(D14): 15761-15785.

709 Clough, S. A., M.W. Shephard, E.J. Mlawer, J.S. Delamere, M.J. Iacono, K. Cady-
710 Pereira, S. Boukabara, P.D. Brown (2005), Atmospheric radiative transfer modeling: a
711 summary of the AER codes, *J. Quant. Spectrosc. Radiat. Transf.*, 91, 233–244.

712 de Zafra, R. L., A. Parrish, P.M.Solomon and J. W. Barrett (1983), A quasi continuous
713 record of atmospheric opacity at $\lambda = 1.1$ mm over 34 days at Mauna Kea observatory,
714 *Int. J. Infrared Millimeter Waves*, 4, 757-765.

715 de Zafra, R. L. (1995), The ground-based measurements of stratospheric trace gases using
716 quantitative millimeter wave emission spectroscopy, in *Diagnostic tools in atmospheric*
717 *physics*, Proceedings of the international school of physics “Enrico Fermi”, pp. 23-54,
718 Società italiana di fisica, Bologna.

719 Di Girolamo, P., R. Marchese, D. N. Whiteman, B. B. Demoz (2004), Rotational Raman
720 Lidar measurements of atmospheric temperature in the UV, *Geophys. Res. Lett.*, Vol.
721 31, L01106, doi:10.1029/2003GL018342.

722 Esposito, F., G. Grieco, G. Masiello, G. Pavese, R. Restieri, C. Serio, and V. Cuomo
723 (2007), Intercomparison among line-parameters spectroscopic databases using
724 downwelling spectral radiance, *Q. J. R. Meteorol. Soc.*, 133, 191-202.

725 Evans, K. F., and G. L. Stephens (1995), Microwave radiative transfer through clouds
726 composed of realistically shaped ice crystals, part II, Remote sensing of ice clouds, *J.*
727 *Atmos. Sci.*, 52, 2058-2072.

728 Han, Y., and E. R. Westwater (2000), Analysis and improvement of tipping calibration
729 for ground-based microwave radiometers, *IEEE Trans. Geosci. and Remote Sens.*, 38,
730 1260-1277.

731 Held, I. M., and B. Soden (2000), Water vapor feedback and global warming, *Annu. Rev.*
732 *Energy Environ.*, 25, 441– 475.

733 Hewison, T. J., D. Cimini, L. Martin, C. Gaffard and J. Nash (2006), Validating clear air
734 absorption model using ground-based microwave radiometers and vice-versa,
735 *Meteorol. Z.*, 15, 1, 27-36.

736 Hirvensalo, J., J. Wahn, and H. Jauhiainen (2002), New Vaisala RS92 GPS radiosonde
737 offers high level of performance and GPS wind data availability, *paper presented at*
738 *12th Symposium on Meteorological Observations and Instrumentation*, Am. Meteorol.
739 Soc., Long Beach, California.

740 James, F. (1994), Minuit, function minimization and error analysis, reference manual,
741 *CERN Program Library Long Writeup*, D506.

742 Jauhiainen, H., M. Lehmuskero (2005), Performance of the Vaisala Radiosonde in the
743 WMO Mauritius Radiosonde Intercomparison, *technical note*, [http://www.vaisala.com/
744 weather/products/soundingequipment/radiosondes/rs92/mauritiustest](http://www.vaisala.com/weather/products/soundingequipment/radiosondes/rs92/mauritiustest).

745 Klein, M., and A. J. Gasieweski (2000), Nadir sensitivity of passive millimeter and
746 submillimeter wave channels to clean air temperature and water vapor variations, *J.*
747 *Geophys. Res.*, 105(D13), 17481-17511.

748 Liebe, H. J., and D. H. Layton (1987), Millimeter-Wave Properties Of The Atmosphere:
749 Laboratory Studies And Propagation Modeling, NTIA-Report 87-224, *Natl.*
750 *Telecommun. And Inf. Admin.*, Boulder, CO.

751 Liebe, H. J., G. A. Hufford, and M. G. Cotton (1993), Propagation modeling of moist air
752 and suspended water/ice particles at frequencies below 1000 GHz. *Proc. AGARD 52d*
753 *Specialists' Meeting of the Electromagnetic Wave Propagation Panel*, Paper 542,
754 Palma de Mallorca, Spain, 3.1–3.10.

755 Liljegren, J. C., S.-A. Boukabara, K. Cady-Pereira and S. A. Clough (2005), The effect of
756 the half-width of the 22-GHz water vapor line on retrievals of temperature and water
757 vapor profiles with a 12-channel microwave radiometer, *IEEE Trans. Geosci. Remote*
758 *Sens.*, 43, 1102-1108.

759 Liou, K.N. (1992), *Radiation and Cloud Processes in the Atmosphere*, 487 pp., Oxford
760 Univ. Press, New York.

761 Liu, G., and J. A. Curry (1998), Remote sensing of ice water characteristics in tropical
762 clouds using aircraft microwave measurements, *J. Appl. Meteorol.*, 37, 337–355.

763 Marsden, D., and F. P. J. Valero (2004), Observation of water vapour greenhouse
764 absorption over the Gulf of Mexico using aircraft and satellite data, *J. Atmos. Sci.*, 61,
765 745– 753.

766 Miloshevich, L. M., A. Paukkunen, H. Vömel, and S. J. Oltmans (2004), Development
767 and validation of a time lag correction for Vaisala radiosonde humidity measurements,
768 *J. Atmos. Oceanic Technol.*, 21, 1305–1327.

769 Miloshevich, L. M., H. Vömel, D. N. Whiteman, B. M. Lesht, F. J. Schmidlin, and F.
770 Russo (2006), Absolute accuracy of water vapour measurements from six operational
771 radiosonde types launched during AWEX-G and implications for AIRS validation, *J.*
772 *Geophys. Res.*, 111, D09S10, doi:10.1029/2005JD006083.

773 Muscari, G., A. G. di Sarra, R. L. de Zafra, F. Lucci, F. Baordo, F. Angelini and G.
774 Fiocco (2007), Middle atmospheric O₃, CO, N₂O, HNO₃, and temperature profiles
775 during the warm Arctic winter 2001–2002, *J. Geophys. Res.*, 112, D14304,
776 doi:10.1029/2006JD007849.

777 Palchetti, L., C. Belotti, G. Bianchini, F. Castagnoli, B. Carli., U. Cortesi, M. Pellegrini,
778 C. Camy-Peyret, P. Jeseck, and Y. Té (2006), First spectral measurement of the Earth's
779 upwelling emission using an uncooled wideband Fourier transform spectrometer,
780 *Atmos. Chem. Phys.*, 6, 5025-5030.

781 Palchetti, L., G. Bianchini, F. Castagnoli, B. Carli, C. Serio, F. Esposito, V. Cuomo, R.
782 Rizzi, T. Maestri (2005), Breadboard of a Fourier-transform spectrometer for the
783 Radiation Explorer in the Far Infrared atmospheric mission, *Appl. Opt.*, 44, 2870-2878.

784 Parrish, A., R. L. de Zafra, J. W. Barrett, P. Solomon and B. Connor (1987), Additional
785 atmospheric opacity measurements at $\lambda = 1.1$ mm from Mauna Kea observatory,
786 Hawaii, *Int. J. Infrared Millimeter Waves*, 8, 431-440.

787 Parrish, A., R. L. de Zafra, P. M. Solomon and J. W. Barrett (1988), A ground-based
788 technique for millimeter wave spectroscopic observations of stratospheric trace
789 constituents, *Radio Sci.*, 23, 106-118.

790 Paukkunen, A., V. Antikainen, and H. Jauhiainen (2001), Accuracy and performance of
791 the new Vaisala RS90 radiosonde in operational use, paper presented at 11th
792 Symposium on Meteorological Observations and Instrumentation, Am. Meteorol. Soc.,
793 Albuquerque, N. M., 14–18 Jan.

794 Raval, A., and V. Ramanathan (1989), Observational determination of the greenhouse
795 effect, *Nature*, 342, 758– 761.

796 Renbarger, T., J. L. Dotson, and G. Novak (1998), Measurements of submillimeter
797 polarization induced by oblique reflection from aluminum alloy, *Appl. Opt.*, 37, 6643-
798 6647.

799 Rosenkranz, P. W. (1998), Water vapor microwave continuum absorption: a comparison
800 of measurements and models. *Radio Sci.*, 33, 919–928.

801 Rosenkranz, P. W. (1999), Correction to “Water Vapor Microwave Continuum
802 Absorption: A Comparison Of Measurements And Models”, *Radio Sci.*, 34, 1025.

803 Rosenkranz, P. W. (2003), Rapid Radiative Transfer Model for AMSU/HSB Channels,
804 *IEEE Trans. on Geosci. and Remote Sens.*, 41, 362-368.

805 Rowe, P. M., L. M. Miloshevich, D. D. Turner, and V. P. Walden (2008), Dry bias in
806 Vaisala RS90 radiosonde humidity profiles over Antarctica, *J. Atm. Oceanic Technol.*,
807 doi:10.1175/2008JTECHA1009.1, in press.

808 Rothman, L. S., et al. (2003), The HITRAN molecular spectroscopic database: edition of
809 2000 including updates through 2001, *J. Quant. Spectrosc. Radiat. Transf.*, 82, 5–44.

810 Solomon, S., D. Qin, M. Manning, Z. Chen, M. Marquis, K.B. Averyt, M. Tignor and
811 H.L. Miller (Eds.) (2007), *IPCC, 2007: Climate Change 2007: The Physical Science*
812 *Basis. Contribution of Working Group I to the Fourth Assessment Report of the*
813 *Intergovernmental Panel on Climate Change*, 996 pp., Cambridge University Press,
814 Cambridge, United Kingdom and New York, NY, USA.

815 Vömel, H., H. Selkirk, L. Miloshevich, J. Valverde-Canossa, J. Valdès, E. Kyrö, R. Kivi,
816 W. Stolz, G. Peng, J.A. Diaz (2007), Radiation Dry Bias of the Vaisala RS92 Humidity
817 Sensor, *J. Atm. Oceanic Technol.*, 24, doi: 10.1175/JTECH2019.1, 953-963.

818 Währn, J., and I. Reikikoski, H. Jauhiainen, and J. Hirvensalo (2004), New Vaisala
819 Radiosonde RS92: Testing and Results from the Field, *Eighth Symposium on*
820 *Integrated Observing and Assimilation Systems for Atmosphere, Oceans, and Land*
821 *Surface*, Seattle.

822 Whiteman, D. N., S. H. Melfi, and R. A. Ferrare (1992), Raman lidar system for the
823 measurement of water vapor and aerosols in the Earth's atmosphere, *Appl. Opt.*, 31,
824 3068-3082.

825 Zammit, C. C., and P. A. R. Ade (1981), Zenith atmospheric attenuation measurements at
826 millimetre and sub-millimetre wavelengths, *Nature*, 293, 550.

827

828

828 **Table 1.** Vaisala RS92k sensors technical data. The accuracy is the 2-sigma confidence
829 level (95.5%), including repeatability, long-term stability, measurement conditions
830 effects, response time [*Jauhiainen and Lehmuskero, 2005; Währn et al., 2004*].

	<i>Range</i>	<i>Resolution</i>	<i>Total uncertainty in sounding</i>
Temperature	-90°C to + 60°C	0.1°C	0.5°C
Humidity	0% to 100%	1%	5%
Pressure	3 hPa to 1080 hPa	0.1 hPa	0.6-1 hPa

831

832

833

834

834 **Captions**

835

836 **Figure 1.** Schematic diagram of the GBMS front-end. The inclination angle of the servo
837 mirror is adjusted in order to keep the S and R powers balanced. The chopper wheel is a
838 reflective half circle rotating with a $\simeq 1$ Hz frequency in order to let through to the
839 receiver the S and R beams, alternatively. See text for details.

840

841 **Figure 2.** Opacity due to water vapor absorption only measured by *Zammit and Ade*
842 [1981] at selected frequencies between 212 and 300 GHz (solid squares) and used in this
843 work at the GBMS operating frequencies (empty triangles). Plotted opacity values are for
844 1 mm of PWV.

845

846 **Figure 3.** Opacity in the zenith direction due to a dry atmosphere as calculated by 5
847 different radiative transfer models (see text and legend) at the GBMS operating
848 frequencies. The modelled opacity values assume a ground station at 3500 m altitude.
849 Error bars indicate the 1σ standard deviation at each frequency calculated from the
850 corresponding $5 \tau_{\text{dry}}$ values.

851

852 **Figure 4.** Scatter plot of PWV values obtained by balancing the S and R powers (x axis)
853 versus PWV measured using a sky dip procedure (y-axis, see text for details). The linear
854 fit to the data points ($y = q + mx$) is represented with a solid line and the 1:1 bisector with
855 a dashed-dotted line. The percentage root mean square of the difference (RMSD%, see
856 text) between the two sets of observations is also reported in the legend together with the

857 total number of correlation points N , the parameters q and m of the linear fit, and the
858 correlation coefficient R^2 .

859

860 **Figure 5.** Time series of GBMS PWV during the ECOWAR field campaign at Plateau
861 Rosa. Plotted values are those obtained from the power balance technique only.

862

863 **Figure 6.** Scatter plot of BASIL versus Vaisala RS92k PWV measurements. Both Lidar
864 and sonde PWV amounts are obtained by integrating humidity measurements from the
865 Plateau Rosa pressure level to 10 km altitude. The linear fit to the data points ($y = q +$
866 mx) is represented with a solid line and the 1:1 bisector with a dashed-dotted line. The
867 RMSD% (see text) is also reported in the legend together with the total number of
868 correlation points N , the parameters q and m of the linear fit, and the correlation
869 coefficient R^2 .

870

871 **Figure 7.** Scatter plot of GBMS versus Vaisala RS92k (panel a), GBMS versus BASIL
872 (panel b), and GBMS versus REFIR-PAD (panel c) PWV amounts. Linear fits to the data
873 points ($y = q + mx$) are represented in each panel with a solid line and the 1:1 bisectors
874 with dashed-dotted lines. The RMSD% (see text) for each comparison is also reported in
875 the corresponding panel together with the associated total number of correlation points N ,
876 the parameters q and m of the corresponding linear fit, and the correlation coefficient R^2 .

877

878

878 **Acknowledgements.** This research was carried out with a grant from MIUR
879 PRIN 2005, project # 2005025202/Area 02 and funding from NASA grant NAG 513029.
880 We are indebted to the Istituto di Fisica dello Spazio Interplanetario (INAF/IFSI), the
881 Centro Nazionale di Meteorologia e Climatologia Aeronautica (CNMA) and the town of
882 Valtournenche (Breuil-Cervinia) for logistic support at the two field sites of Plateau Rosa
883 and Cervinia. We thank Daniele Fuà and Giorgio di Sarra for helpful discussions. We
884 also thank Dave Turner and two anonymous reviewers for valuable comments on the
885 original manuscript.
886

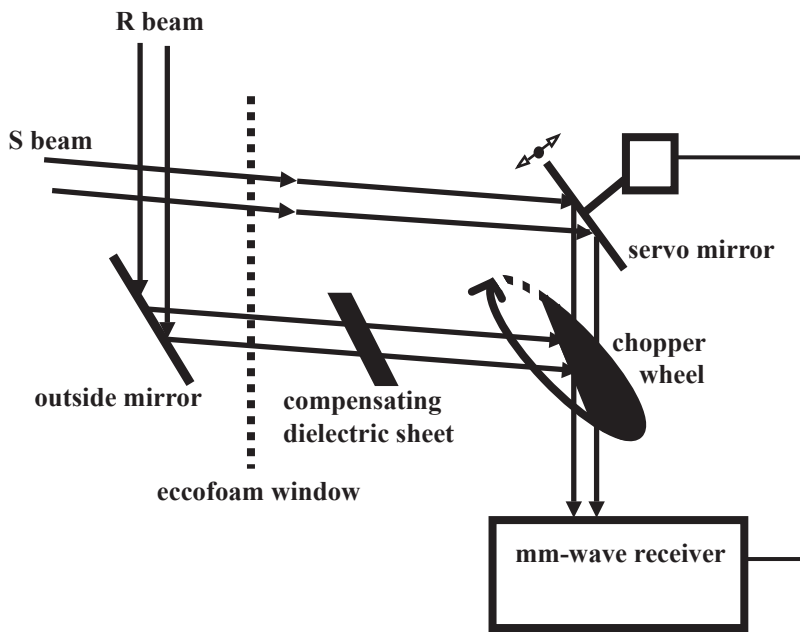


Figure 1. Schematic diagram of the GBMS front-end. The inclination angle of the servo mirror is adjusted in order to keep the S and R powers balanced. The chopper wheel is a reflective half circle rotating with a ≈ 1 Hz frequency in order to let through to the receiver the S and R beams, alternatively. See text for details.

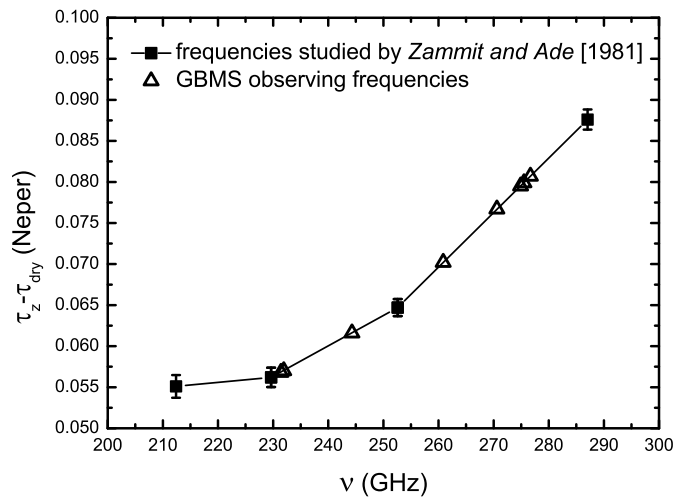


Figure 2. Opacity due to water vapor absorption only measured by *Zammit and Ade* [1981] at selected frequencies between 212 and 300 GHz (solid squares) and used in this work at the GBMS operating frequencies (empty triangles). Plotted opacity values are for 1 mm of PWV.

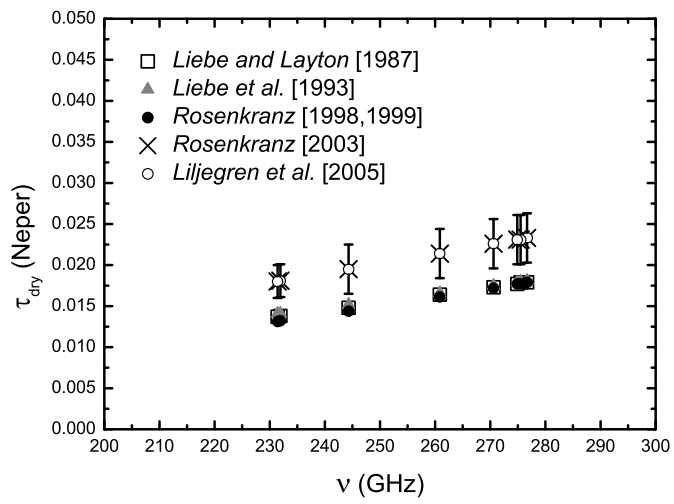


Figure 3. Opacity in the zenith direction due to a dry atmosphere as calculated by 5 different radiative transfer models (see text and legend) at the GBMS operating frequencies. The modelled opacity values assume a ground station at 3500 m altitude. Error bars indicate the 1σ standard deviation at each frequency calculated from the corresponding 5 τ_{dry} values.

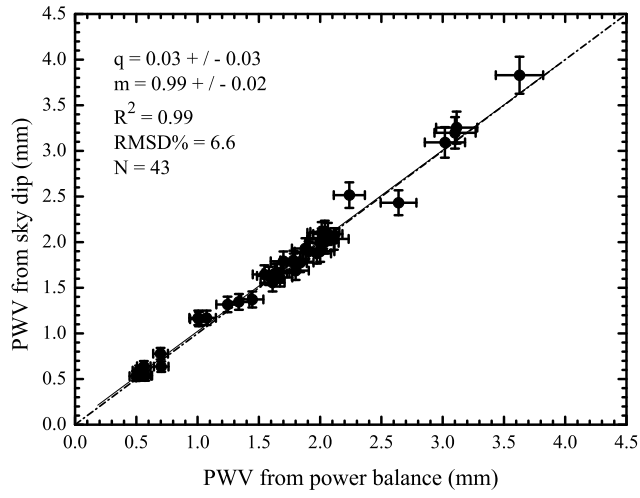


Figure 4. Scatter plot of PWV values obtained by balancing the S and R powers (x axis) versus PWV measured using a sky dip procedure (y-axis, see text for details). The linear fit to the data points ($y = q + mx$) is represented with a solid line and the 1:1 bisector with a dashed-dotted line. The percentage root mean square of the difference (RMSD%, see text) between the two sets of observations is also reported in the legend together with the total number of correlation points N , the parameters q and m of the linear fit, and the correlation coefficient R^2 .

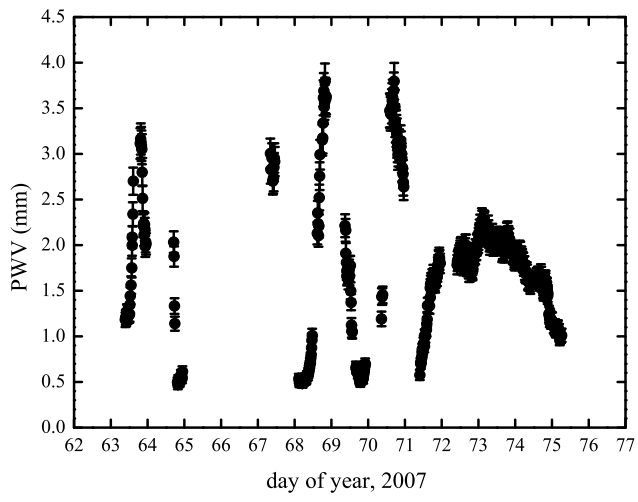


Figure 5. Time series of GBMS PWV during the ECOWAR field campaign at Plateau Rosa. Plotted values are those obtained from the power balance technique only.

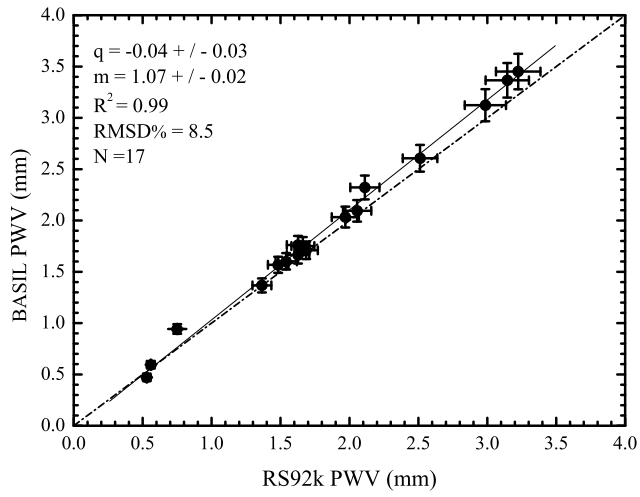


Figure 6. Scatter plot of BASIL versus Vaisala RS92k PWV measurements. Both Lidar and sonde PWV amounts are obtained by integrating humidity measurements from the Plateau Rosa pressure level to 10 km altitude. The linear fit to the data points ($y = q + mx$) is represented with a solid line and the 1:1 bisector with a dashed-dotted line. The RMSD% (see text) is also reported in the legend together with the total number of correlation points N , the parameters q and m of the linear fit, and the correlation coefficient R^2 .

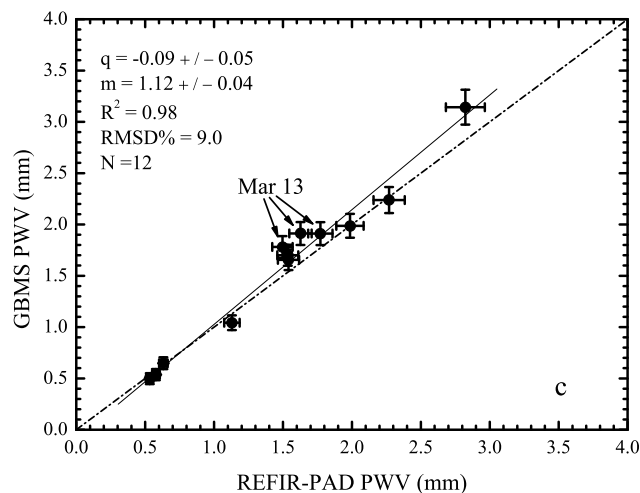
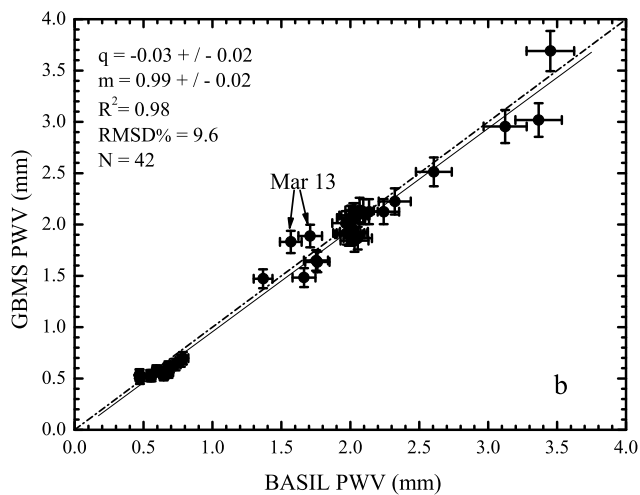
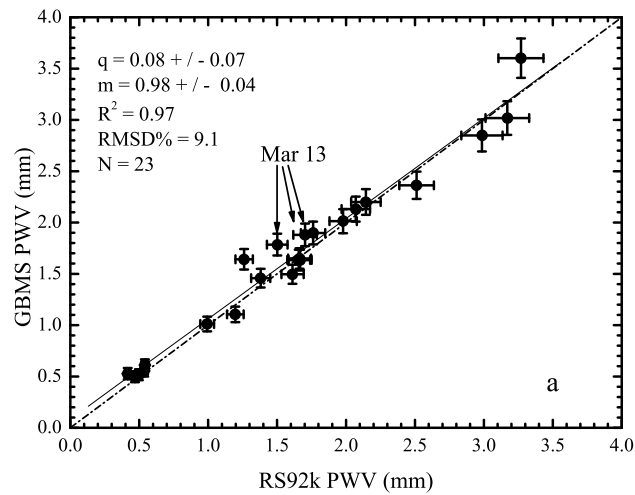


Figure 7. Scatter plot of GBMS versus Vaisala RS92k (panel a), GBMS versus BASIL (panel b), and GBMS versus REFIR-PAD (panel c) PWV amounts. Linear fits to the data points ($y = q + mx$) are represented in each panel with a solid line and the 1:1 bisectors with dashed-dotted lines. The RMSD% (see text) for each comparison is also reported in the corresponding panel together with the associated total number of correlation points N , the parameters q and m of the corresponding linear fit, and the correlation coefficient R^2 .

4.2 Comparisons between GBMS and UARS MLS HNO₃ retrievals (1993-1995)

NASA's Upper Atmosphere Research Satellite (UARS) with JPL's Microwave Limb Sounder MLS as one of its 10 instruments was launched 12 September 1991. MLS observes the thermal emission from the Earth's limb using a microwave heterodyne technique. Although designed to measure stratospheric ozone, water vapor and chlorine monoxide it has also produced useful observations of other stratospheric constituents, among which HNO₃. UARS MLS acquired HNO₃ profiles from September 1991 to August 2001, although after March 1994 the measurements became increasingly sparse in order to conserve lifetime of the MLS antenna scan mechanism and UARS power. The UARS orbit and MLS viewing geometry are such that MLS observes from 34° latitude on one side of the equator to 80° on the other, alternating 10 times per year between viewing northern and southern high latitudes (see *Santee et al.* (1999) and references therein for further details).

MLS profiles are retrieved using an algorithm based on the Optimal Estimation approach. The retrievals used in this study are from the definitive UARS MLS HNO₃ data set, known as version 6 (hereinafter referred as v6). This is a corrected version of the prior version 5 (v5), accounting for emission from 2 excited vibrational states previously neglected. The correction consists of a linear temperature-dependent scaling of the original v5 HNO₃ values. The v6 HNO₃ vertical profiles are reported as function of pressure and are judged to be reliable between 100 hPa and 4.6 hPa (~ 15-35 km altitude). Their vertical resolution, defined as the full width at half maximum of the Averaging Kernels, is ~5 km in the upper troposphere and lower stratosphere, degrading to ~10 km in the middle and upper stratosphere. The horizontal resolution of the measurements is of 400 × 400 km. The typical single profile precision, computed as the minimum monthly rms variability of HNO₃ profiles in a region of homogeneous atmospheric conditions, varies with altitude, ranging from 0.8 to 1.5 ppbv. Here I have decided to use the theoretical precision values, provided by the retrieval algorithm and accounting for variations in the uncertainties that may occur from a profile to another.

Even if these theoretical estimates are generally consistent with the empirically determined values, the last ones tend to be conservative. Therefore to obtain the best estimate of precision, these theoretical uncertainties have been multiplied by a “precision ratio ” factor (~0.7), according to *Livesey et al.* (2003) (see Table 4.1). The estimated absolute accuracy of the MLS v6 has not been quantified in detail but, based on comparisons with correlative data sets, values of 2ppbv are expected below 15 hPa and 3 ppbv above that pressure level. The MLS HNO₃ uncertainties adopted in this study include both random error and systematic uncertainties. A detailed description of the MLS v5 data processing algorithm and validation of many of the version 6 data products is given by *Livesey et al.* (2003); information about the quality of the version 5 retrievals is also available from the MLS web site (<http://mls.jpl.nasa.gov>). In this intercomparison I used only measurements that passed all the quality control checks.

Pressure / hPa	Vertical resolution ^a / km	Typical precision / ppbv	Precision ratio ^b
4.6	10.5	1.5	0.7
6.8	10.0	1.4	0.7
10	9.3	1.3	0.7
15	8.7	1.2	0.7
22	7.4	1.2	0.7
31	6.4	1.1	0.7
46	5.7	1.0	0.7
68	5.7	0.8	0.6
100	4.3	1.3	0.9

Table 4.1 Estimated vertical resolution and precision of v6 UARS MLS HNO₃ (from *Livesey et al.*, 2003)

A description of the GBMS experimental apparatus and the observational technique is given in Chapter 2, while the new retrieval procedure used to deconvolve HNO₃ spectral lines is extensively illustrated in Chapter 3. Briefly, the GBMS HNO₃ profiles are retrieved as a function of altitude every km and have a vertical resolution of ~7-10 km, depending on the altitude. Although the GBMS instantaneous field of view is about 10 km in width at 23 km of altitude, the integration time of each measurement (about 6 hours) means that the GBMS samples an air stream typically 200-300 km in length, as air masses move over the observing site.

In this section UARS MLS HNO₃ vertical profile are compared to those retrieved by the GBMS set up at the Amundsen Scott Base, located at the geographic South Pole. HNO₃ measurements at South Pole were carried out by means of GBMS during the greater part of 1993 and 1995 twice a week (*McDonald et al.*, 2000), even if there are some periods of instrumental inactivity or malfunctioning, during which data are not available. A comprehensive comparison of this data set with nearby MLS profiles is presented in *Muscari et al.* (2002). I basically followed the approach used in this previous comparison, with some changes due to the new retrieval algorithm and to more stringent coincidence criteria needed in the current intercomparison.

Since GBMS measurements are taken at 90°S, and MLS reaches a southernmost latitude of about 80°, the two sets of data are never co-located. To compensate for this, I used the same trajectory mapping technique used in *Muscari et al.* (2002), to connect air masses passing over the Pole with locations of MLS measurements. I employed the Goddard Space Flight Center (GSFC) trajectory model (*Schoeberl and Sparling*, 1995), which advects air parcels backward or forward in time with respect to an initial position using horizontal wind velocity fields and diabatic heating rates (proportional to vertical transport). I used 5 day trajectories, both backward and forward in time, at seven potential temperature (θ) surfaces: 465, 520, 585, 620, 655, 740, and 960 K. These levels have been chosen in order to be close to the six standard UARS pressure levels used for MLS v6 HNO₃ retrievals, plus one additional level (620 K) to allow a better characterization of the peak of the HNO₃ distribution. As an example, Figure 4.2 shows 5-day backward and 5-day forward trajectories starting over the South Pole on June 3, 1993, at 520 K. For each run, trajectory traces were initiated at 8 locations surrounding the Pole (at 4 cardinal points separated 90° in longitude and by offsets of 0.5° and 1° in latitude from the Pole) at noon of any day when GBMS data are available. After running the individual trajectories, all the parameters (position, temperature, etc.) of the 8 parcels were averaged together at each time step along their trajectories, and this averaged trajectory was used to select MLS retrievals to compare with GBMS data. In <10 % of the traces, one of the 8 parcels would begin to deviate substantially from the averaged trajectory position and was dropped from the averaging process. For each trajectory I considered only parcels which were found between 70°S and 80°S at noon of the different days. A latitude of 70°S was chosen as the northern boundary to obtain

and average together a sufficient number of MLS measurements, while still minimizing the distance between the GBMS profiles observed at the Pole and the MLS measurements selected. I looked at the parcel's position and selected MLS measurements (if any are available) within a box of $\pm 10^\circ$ longitude (approximately ± 287 km) and $\pm 2.5^\circ$ latitude (approximately ± 278 km) around this location. MLS observations belonging to the specified box were averaged together using a $\cos^2(d)$ weighting function depending on their distance "d" from the center of the box ("d" is normalized to have $\cos^2(d) = 0$ at the edges of the box). At this stage of the process, I have a spatially-averaged profile of MLS HNO₃ mixing ratio for each day when the following two conditions coexist: 1) MLS data are available; 2) the air parcel is between 70°S and 80°S. Finally, for each GBMS day of measurement, I selected the MLS spatially-averaged profile the closest in time to it. When 2 MLS spatially-averaged profiles temporarily equidistant to GBMS data exist (for example air parcels that passed on the Pole the day before and the day after a GBMS measurement), I averaged together their mixing ratio values. Even if 5 day trajectories were run, as a result of this procedure, the matching time between MLS and GBMS observations has been reduced to 3 days. In fact, as in this comparison I am looking for systematic differences between the two MLS datasets, I decided to adopt this more restrictive selection criterion, even if it leads to reducing the number of useful coincidences. Both GBMS and MLS selected averaged profiles must be interpolated onto the chosen θ levels, in order to be compared. However, because of the different vertical resolutions of the instruments, the higher resolution MLS profiles should be convolved using the GBMS Averaging Kernels (see Chapter 3 for further details) before this comparison. Thus, MLS averaged profiles are interpolated on GBMS vertical grid, convolved with the GBMS Averaging Kernels and finally interpolated on potential temperatures. To interpolate both data sets on θ , I use the daily global assimilated pressure and temperature data from the U.K. Meteorological Office (*Swinbank and O'Neill, 1994*) interpolated to the location of interest.

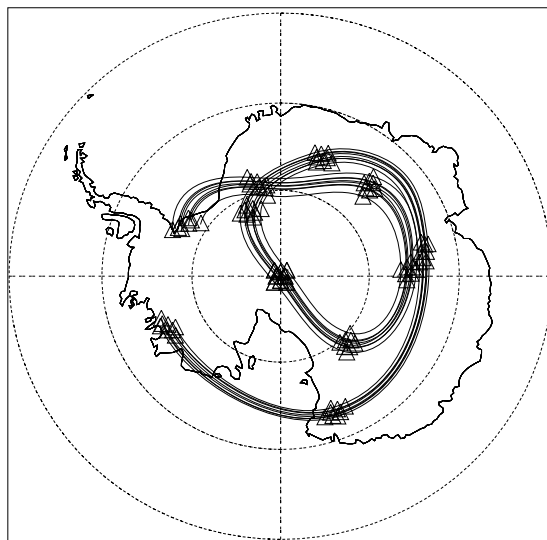


Figure 4.2 Five day backward and forward trajectories originating at the South Pole on 3 June 1993, at $\theta=520$ K. Triangles indicate the daily position of the 8 parcels at noon.

As seen in Chapter 1, the polar early winter stratosphere is characterized by a strong denitrification, starting as soon as temperatures reach the PSC formation range. The HNO₃ is almost entirely removed by the beginning of late winter. In spring, with the daylight return, lower stratospheric nitric acid start to gradually recover, due to a combination of evaporation of residual PSCs, descent from higher levels and advection of air masses from lower latitude regions, as the vortex weakens and breaks up. In this season, the intrusion of air previously confined outside the vortex causes a large variability in HNO₃ mixing ratio. Because of the final aim of this study (the cross-calibration of UARS and Aura MLS data sets), I selected periods with HNO₃ mixing ratio peak values at the South Pole not radically different from those observed at northern midlatitude, available from GBMS at Testa Grigia. The peculiar behavior of the HNO₃ in winter and spring make the measurements carried out in these periods not suitable for the aim of the study. No summer measurements are available for 1993 (and very few for 1995). Thus I decided to focus this comparison on Antarctic Fall, before the onset of significant denitrification. In all, 4 days of measurements (from 15 April to 28 May) were available for 1993 and 4 days (from 14 March to 8 April) for 1995. Mean GBMS and MLS profiles and mean differences for the 2 years are shown in Figure 4.3 and Figure 4.4, respectively.

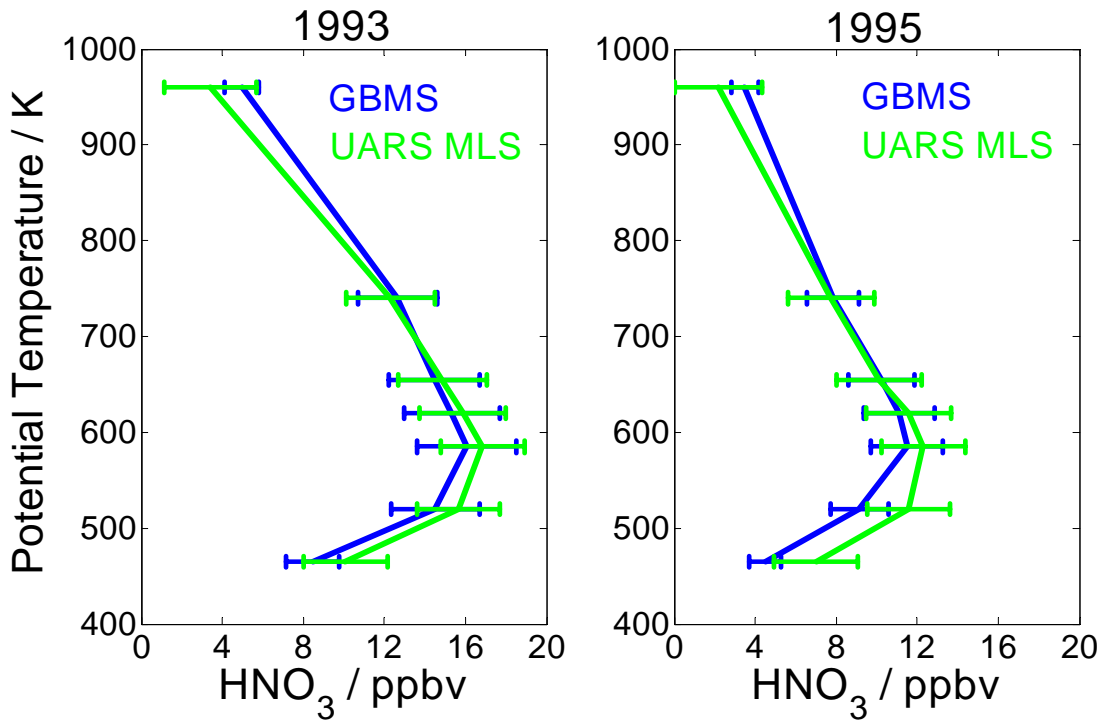


Figure 4.3 Average profile comparisons (versus θ) between GBMS profiles (blue) at the South Pole (translated via trajectory calculations to positions coincident with UARS MLS profiles) and UARS MLS profiles (green) for 1993 (left panel) and 1995 (right panel). Mean profiles are obtained by averaging 4 days of measurements for 1993 and 4 days for 1995.

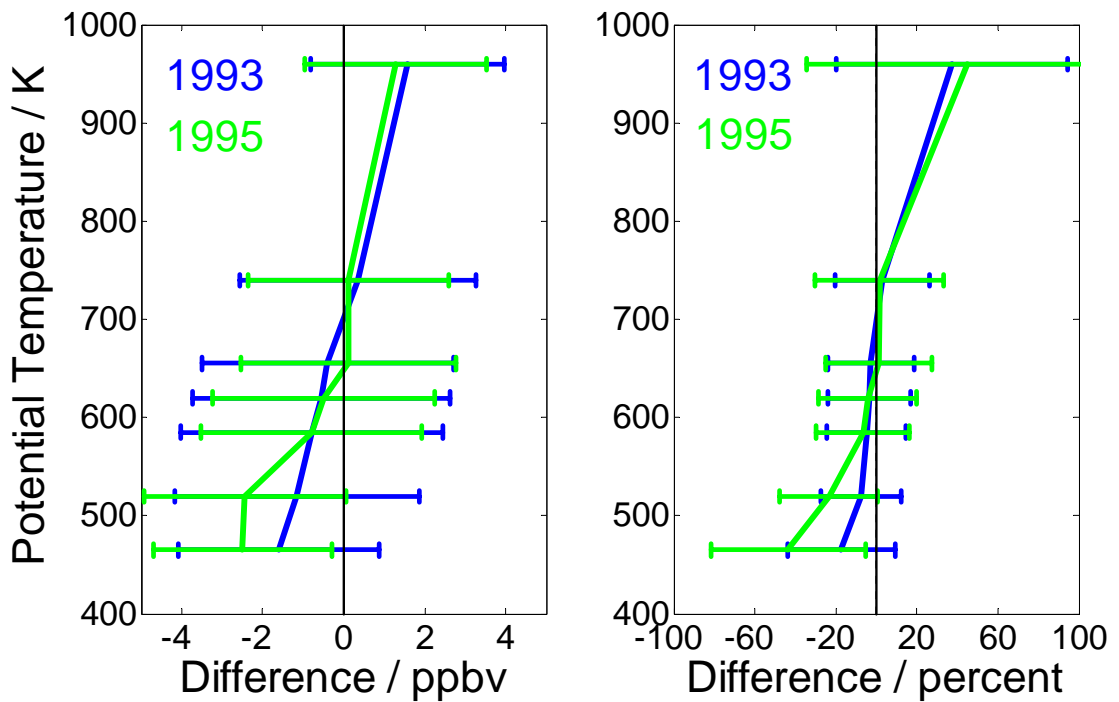


Figure 4.4 Left panel: Average HNO_3 absolute difference for GBMS – MLS in the 1993 (blue) and 1995 (green). Right panel: Same differences, expressed in percent.

Figure 4.4 shows that the differences between UARS MLS and GBMS HNO_3 at the

South Pole are consistent, within the error bars, for the two similar time periods of GBMS observations in 1993 and 1995. For that reason the 1993 and 1995 South Pole data sets have been averaged together; results are shown in figure 4.5.

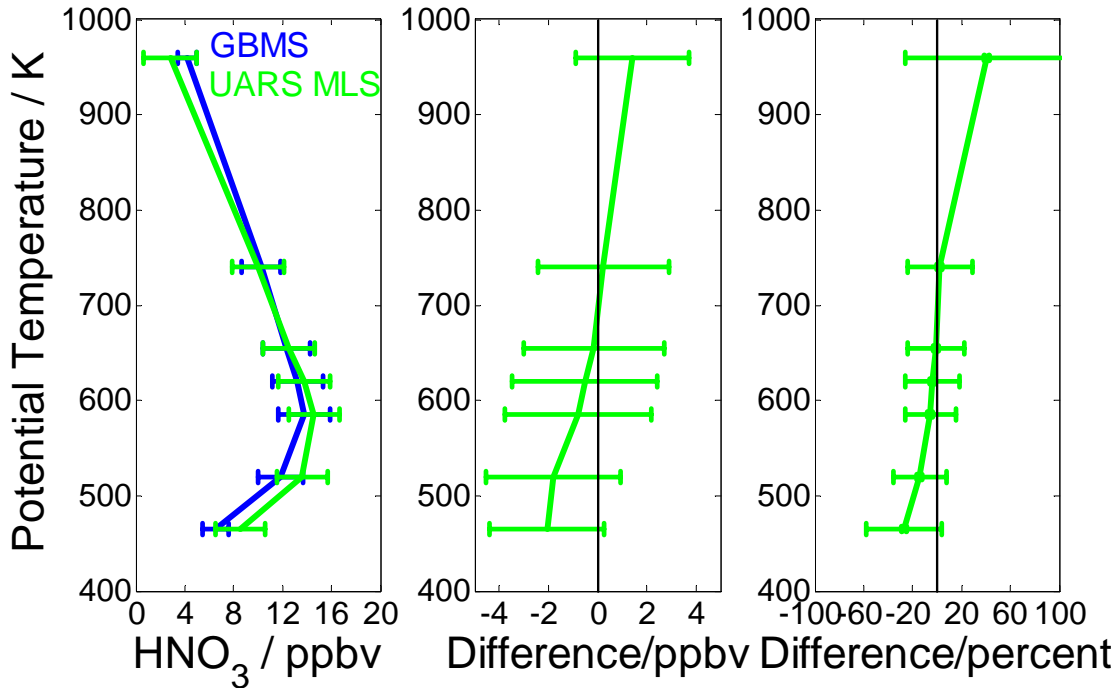


Figure 4.5 Left panel: Average profile comparisons between GBMS (blue) and UARS MLS (green). Middle panel: Average difference (ppbv) for GBMS – MLS. Right panel: Average difference (percent). Here, the 1993 and 1995 datasets are averaged together.

θ (K)	Difference (ppbv)	Difference (percent)
465	-2.05	-27.35
520	-1.791	-14.11
585	-0.791	-5.57
620	-0.52	-3.90
655	-0.14	-1.18
740	0.23	2.34
960	1.42	40.48

Table 4.2 Absolute and relative mean differences between GBMS and UARS MLS HNO₃ mixing ratio at the South Pole. Mean values are obtained from the average of the 1993 and 1995 data sets.

Combining the 1993 and 1995 South Pole comparisons (Figure 4.5) shows that the

agreement between UARS MLS and GBMS HNO₃ is typically within ~ 20% in the lower stratosphere and within 5% in the middle stratosphere. The two data sets are consistent, within error bars, at all the potential temperature levels. Moreover, the differences found out in this comparison are similar to those observed in previous intercomparison of UARS MLS v6 with other HNO₃ data sets (from CLAES and ILAS), with higher MLS values in the lower stratosphere and lower MLS values at 740 and 960 K (*Livesey et al.*, 2003)

4.3 Comparisons between GBMS and Aura MLS HNO₃ retrievals

The Microwave Limb Sounder (MLS) is one of the four instruments, aboard of Aura, the last NASA's EOS satellite, launched on 15 July 2004 into a near-polar, Sun-synchronous orbit (*Schoeberl et al.*, 2006b). It is the advanced successor to the MLS experiment on UARS and observes several atmospheric parameters by measuring millimeter and submillimeter wavelength thermal emission from Earth's limb with seven radiometers. Nitric acid is measured by three of these radiometers, centered near 190, 240, and 640 GHz. The standard HNO₃ product is derived from the 240-GHz retrievals at and below 10 hPa and from the 190-GHz retrievals above that level; the HNO₃ measurements from the 640-GHz radiometer have significantly poorer precision and are not used. The Aura MLS fields of view point forward in the direction of orbital motion and vertically scan the limb in the orbit plane, leading to data coverage from 82°S to 82°N latitude on every orbit. Thus MLS obtains continuous daily sampling of both polar regions. Most MLS data products, including HNO₃, are reported on a fixed vertical pressure grid with six levels per decade change in pressure in the troposphere and stratosphere. The version 2.2 (v2.2) MLS retrieval algorithms, described in detail by *Livesey et al.* (2006), are based on the standard optimal estimation method; they employ a two-dimensional approach that takes into account the fact that limb observations from consecutive scans cover significantly overlapping regions of the atmosphere. The two-dimensional nature of the MLS data processing system means that the Averaging Kernels can be used to describe both vertical and horizontal resolution. The vertical resolution is 3–4 km in the upper troposphere and lower stratosphere, degrading to ~5 km in the middle and upper stratosphere. The v2.2 HNO₃ data are recommended for scientific use over the range 215 to 3.2 hPa, with single-profile precision, empirically estimated, of ~0.7 ppbv throughout. The best precision estimate is represented by the theoretical precision, that takes into account occasional variations in instrument performance, even if it generally overestimates the actual measurement noise above 22 hPa. Systematic uncertainties, quantified through a comprehensive set of retrieval simulations, are estimated to induce in the v2.2 HNO₃ measurements biases

that vary with altitude between ± 0.5 and ± 2 ppbv and relative errors of ± 5 – 15% throughout the stratosphere, rising to $\pm 30\%$ at 215 hPa. Further details on v2.2 HNO₃ data quality and validation can be found in *Santee et al.* (2007).

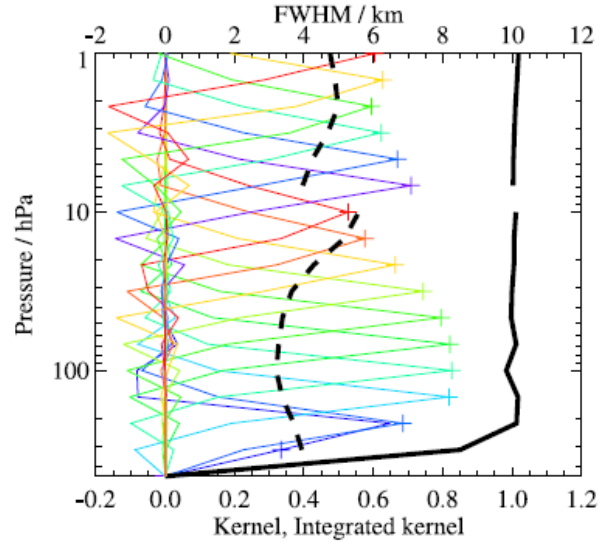


Figure 4.6 Typical averaging kernels for the MLS v2.2 HNO₃ data. The dashed black line indicates the resolution, determined from the full width at half maximum (FWHM) of the averaging kernels. The solid black line shows the integrated area under each Kernel (from *Santee et al.*, 2007)

Pressure, hPa	Resolution, Vertical × Horizontal, ^a km	Precision, ^b ppbv	Bias Uncertainty, ^c ppbv	Scaling Uncertainty, ^c %	Comments
2.1–0.001	-	-	-	-	unsuitable for scientific use
6.8–3.2	4–5×300	±0.7	±0.5	±10–15%	
22–10	4.5–5.5×450–550	±0.7	±1–2	±10%	
100–32	3.5×400	±0.7	±0.5–1	±5–10%	
147	3.5×400	±0.7	±0.5	±15%	
215	4×500	±0.7	±1	~±30%	
316	-	-	-	-	unsuitable for scientific use
1000–464	-	-	-	-	not retrieved

Table 4.3 Summary of Aura MLS v2.2 HNO₃ characteristics

Presently the full Aura MLS HNO₃ data set is available in the version 2.2. However a reanalysis with the new version 3 of the retrieval algorithm is ongoing. All the data presented in this comparison are retrieved with the preliminary v3, even if the fully reprocessed v3 HNO₃ dataset will not be available until Spring, 2011. The accuracy of the MLS v3.1 has not yet been quantified and here we use the accuracy of the old v2.2. Both accuracy and precision are included in the MLS uncertainty considered

hereinafter.

In this section MLS HNO₃ measurements are compared with those from GBMS carried out at two different observing sites in the northern hemisphere: Testa Grigia, a high mountain station on the Italian Alps (45.9 °N, 7.7 °E, 3500 m a.s.l.) and Thule Air Base, Greenland (76.5 °N, 68.7 °W). The GBMS has been operational at Testa Grigia for 4 winter periods, from February 2004 to March 2007, for a total of 116 days grouped in about 18 field campaigns. In January 2009 the ground based spectrometer was moved to Thule, within a project aimed at studying stratospheric processes occurring during the polar winter. It has been operated from January to March 2009 and from January to February 2010 mostly on a daily basis, except during periods of poor weather conditions. Since Aura is in a near polar orbit, co-located measurements are available for both these sites and there is no need to use the trajectory tracing technique for this comparison. Here, each GBMS observation is compared to the closest MLS profile, with a coincidence criteria of $\pm 10^\circ$ longitude, $\pm 2.5^\circ$ latitude and ± 24 h. I again convolved the higher resolution MLS profiles with the GBMS averaging kernels to account for the different vertical resolutions of the two data sets. Moreover, in order to obtain comparable results for the two intercomparisons (GBMS versus UARS MLS and GBMS versus Aura MLS) the same vertical grid used for the previous comparison must be used here. Thus both GBMS and MLS profiles have been interpolated on the 7 selected θ levels (see section 4.2), using temperature and pressure data from the NCEP reanalysis.

In the following comparison only MLS data that passed all the quality control have been used. GBMS measurements for which the observed spectrum has been poorly fitted by the retrieval algorithm ($\text{rms} > 0.02$) are considered less reliable and have been left out from the comparison.

4.3.1 Testa Grigia (2004-2007)

Figure 4.7 shows average GBMS and MLS (version 2.2 and 3) coincident profiles from the 2004-2005 winter. A much better agreement between this and GBMS observations is obtained using MLS preliminary version 3.

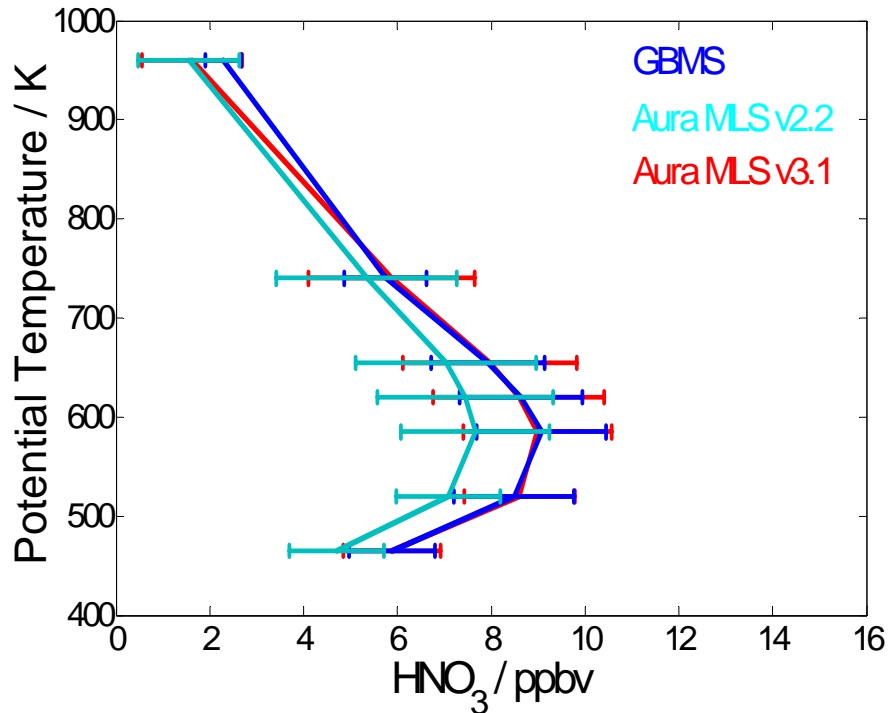


Figure 4.7 Comparisons between average GBMS retrievals and coincident Aura MLS profiles (v2.2 in red and v3.1 in green) for 10 days in the 2004-2005 winter (January-February), at Testa Grigia, Italy.

GBMS mean profiles and Aura MLS v3.1 coincident data comparison for 2004-2005 (10 days), 2005-2006 (9 days) and 2006-2007 (9 days) winter periods at Testa Grigia are presented in figure 4.8. Corresponding mean differences are shown in Figure 4.9.

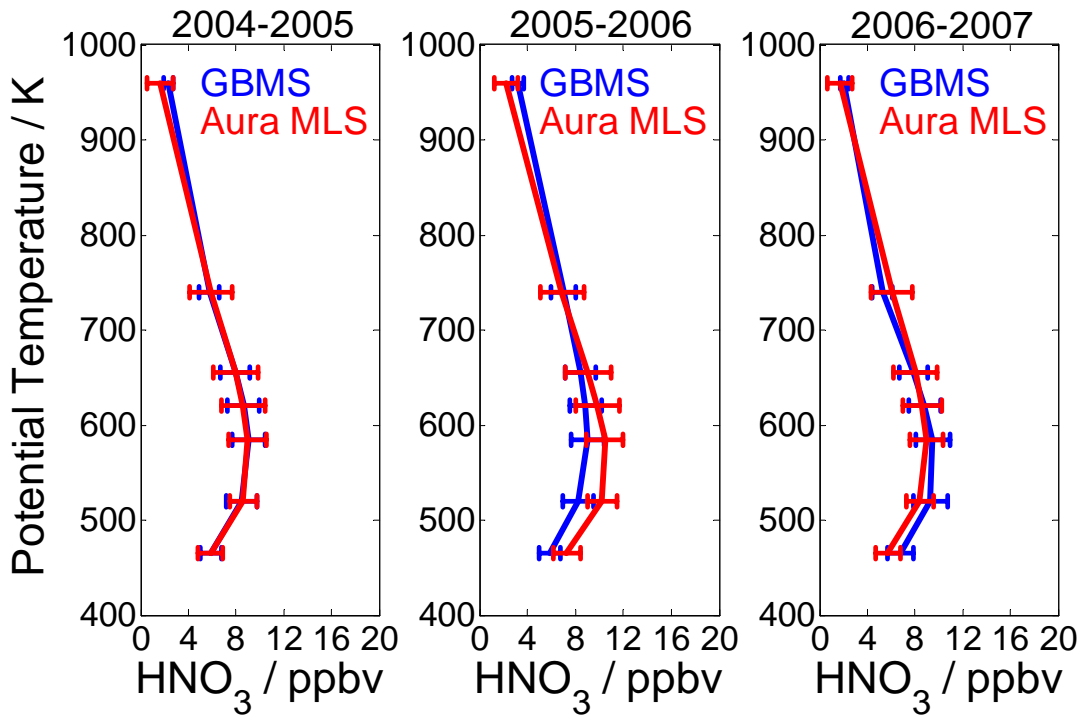


Figure 4.8 GBMS average HNO₃ profiles (blue) from Testa Grigia are compared to the average of coincident Aura MLS v3.1 profiles (red) for 10 days in 2004-2005 (left panel), 9 days in 2005-2006 (middle panel) and 9 days in 2006-2007 (right panel).

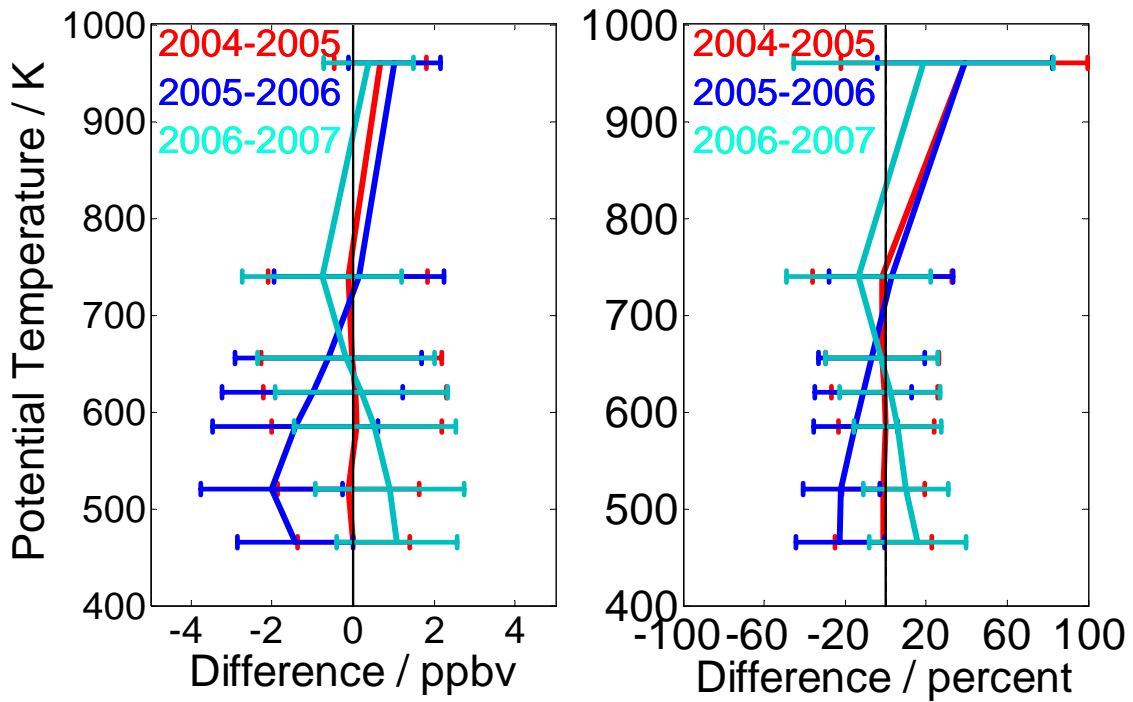


Figure 4.9 Left panel: Average HNO₃ differences (GBMS – Aura MLS), in ppbv, for 2004-2005 (red), 2005-2006 (blue), and 2006-2007 (cyan). Right panel: Same, for percent differences.

Figure 4.9 shows that the differences between Aura MLS v3 and GBMS HNO₃ values for the three winters of measurements at Testa Grigia agree fairly well. For the potential temperature levels from 585 up to 960 K the agreement is within the errors. Because of the overall good agreement of the mean differences in the three years and after examining and excluding any possible instrumental issue and/or particular atmospheric conditions, the whole Testa Grigia data set has been averaged together. Mean profiles and mean differences are shown in Figure 4.10 A very good agreement, within 5% for all θ levels but the 960 K, is obtained between GBMS and Aura MLS v3.1 HNO₃.

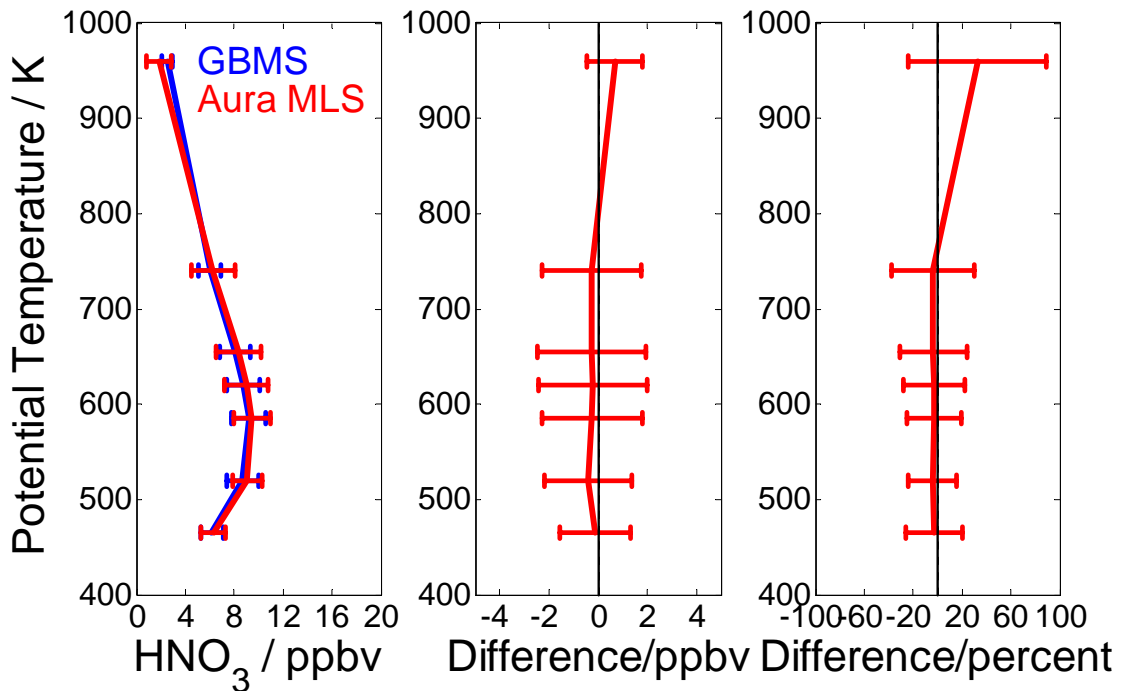


Figure 4.10 Left panel: GBMS (blue) and Aura MLS (red) mean HNO₃ profiles obtained from the average of the three years Testa Grigia data sets. The middle and right panels show the average differences (ppbv and percent, respectively)

θ (K)	Difference (ppbv)	Difference (percent)
465	-0.10	-2.64
520	-0.40	-4.34
585	-0.25	-2.86
620	-0.23	-3.02
655	-0.26	-3.56
740	-0.24	-4.06
960	0.68	32.44

Table 4.4 Absolute and relative mean differences between GBMS and Aura MLS HNO₃ mixing ratio at Testa Grigia. Mean values are obtained from the average of the three years of observations.

4.3.2 Thule (2008-2009)

Mean GBMS and v3.1 MLS coincident profiles and mean differences for 11 days of measurements at Thule, during polar winter 2009, are shown in Figure 4.11.

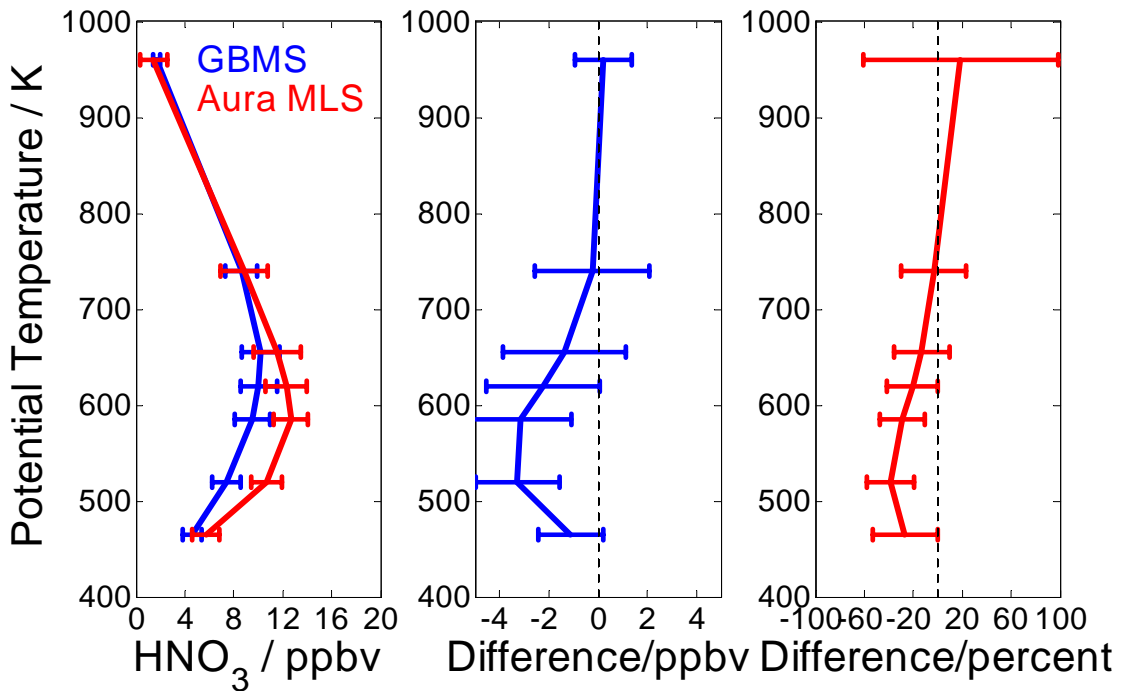


Figure 4.11 Left panel: Mean profiles from 11 days of coincident GBMS (blue) and Aura MLS (red) profiles at Thule. Mean differences (in ppbv and percent) are given in the other two panels.

θ (K)	Difference (ppbv)	Difference (percent)
465	-1.12	-26.74
520	-3.29	-38.64
585	-3.13	-28.59
620	-2.24	-20.58
655	-1.37	-13.24
740	-0.23	-3.24
960	0.22	18.52

Table 4.5 Absolute and relative mean differences between GBMS and Aura MLS HNO₃ mixing ratio at Thule.

Differences as large as 3 ppbv (~40%) are observed on average near the peak for this data set. The worse agreement between MLS and GBMS data at Thule, with respect to Testa Grigia, could be due to a potential issue with the retrieval of the ozone background for this particular data set. In fact, while ozonsonde data (obtained from Payerne, Switzerland, about 100 km away from the GBMS observing site) were available for the entire period of GBMS operations at Testa Grigia, only 2 ozonsondes were launched from Thule, during January – March 2009. As seen in Chapter 3, the lack of reliable a priori information on the ozone vertical distribution could introduce a significant uncertainty in the retrieved HNO₃ profiles, especially at lower altitudes.

4.4 UARS MLS – Aura MLS cross-calibration

Comparing figures 4.10 and 4.11 is clear that somewhat different characteristics in the average differences between the two northern hemisphere observing sites exist. Apart from the potential problem with the ozone background, sites dependent differences are not completely unexpected since some latitude-dependent differences are observed also between MLS and other satellite data sets (ACE-FTS, Odin-SMR). Comparisons of MLS HNO₃ with these satellite datasets are scheduled as part of the GOZCARDS project and maybe will help to clarify the observed discrepancies. At this stage of the project only the Testa Grigia and South Pole measurements have been considered for the cross calibration of UARS MLS and Aura MLS data sets. Relative mean differences for South Pole and Testa Grigia data sets are shown in Figure 4.12. They show very similar trend and are consistent, within the error bars, for all the θ levels. From these comparisons we infer that no adjustments are required to link the UARS and Aura HNO₃ data sets, at least in the error range obtained combining MLS and GBMS total uncertainties .

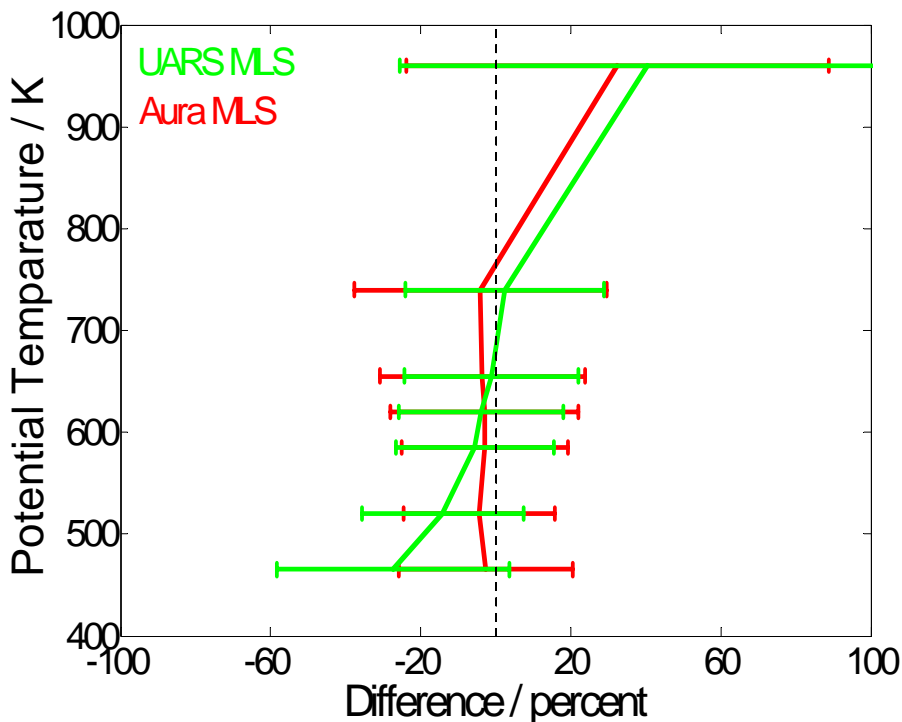


Figure 4.12 Mean relative differences GBMS - UARS MLS data at South Pole (green) and GBMS - Aura MLS data at Testa Grigia (red).

Summary and Conclusions

In the first part of this thesis work I developed a modified version of the OEM algorithm (Rogers, 2000) to invert HNO₃ microwave spectra observed by means of the Ground-Based Millimeter-wave Spectrometer. Uncertainties on a priori information and spectral measurements noise, represented by covariance matrices, were treated as tunable parameters and their values were set empirically in order to optimize the retrieval sensitivity. A standard Gaussian profile has been used as *a priori* HNO₃ mixing ratio vertical profile instead of using data coming from models or climatology. Using these constraints, nitric acid mixing ratio vertical profiles were retrieved between 10 and 50 km. The nominal retrieval sensitivity, assessed by means of Averaging Kernels, showed that the retrieved profiles are most accurate between ~18 and ~32 km altitude and the vertical resolution is about 7-8 km in this altitude interval. In fact, retrieval tests suggested that the inversion algorithm is able to infer the altitude of the profile mixing ratio peak with an uncertainty of ± 1 km, even though the nominal resolution is formally coarser. In this vertical range the contribution of the a priori profile to the retrieval is typically within 20% and the overall uncertainty of the final HNO₃ mixing ratio profiles is approximately 15% -18% (depending on the altitude).

Careful comparisons of HNO₃ profiles obtained with the previously-employed MI (Muscarei *et al.* (2007), and references therein) and the present OE algorithms are shown in Chapter 3 and displayed no significant differences in mixing ratio values and their associated errors. The HNO₃ profiles retrieved with the formerly-adopted MI technique showed an overall good agreement with satellite data by the two NASA/JPL Microwave Limb Sounder (MLS) experiments (UARS MLS and EOS Aura MLS) (Muscarei *et al.*, 2002; Santee *et al.*, 2007) and the agreement between GBMS HNO₃ profiles obtained with the two different retrieval techniques has been an initial validation of the new inversion method I developed. The OEM is however an improvement with respect to the MI because it provides additional information on the retrieved profiles. Such information are useful to better characterize and compare the GBMS retrievals to other datasets.

The new retrieval algorithm developed for inversion of HNO₃ spectra has been also

applied to other trace gases observed by GBMS, namely O₃ and N₂O. Reliable O₃ mixing ratio profiles were retrieved between ~15 and ~55 km, with a vertical resolution of 6-7 km, whereas N₂O retrievals proved to be sensitive to true atmospheric profiles between ~20 and ~45 km altitude, with the same vertical resolution. Preliminary results of these retrievals are briefly presented in this thesis and widely discussed in the paper “*Evolution of temperature, O₃, CO, and N₂O profiles during the exceptional 2009 Arctic major stratospheric warming as observed by lidar and mm-wave spectroscopy at Thule (76.5°N, 68.8°W), Greenland*” recently submitted to *Journal of Geophysical Research*. Further refinements and validation efforts on O₃ and N₂O OEM retrievals are still underway and the results shown in the paper should be considered as preliminary. CO retrievals have not yet undergone such testing and vertical profiles reported in the manuscript are therefore still obtained using the old inversion technique (Chahine-Twomey method (*de Zafra and Muscari, 2004*, and references therein)). The characterization of the OEM necessary for its application to upper stratospheric/mesospheric CO and O₃ profiles is a future development of this thesis work.

The second part of this study deals with the validation of HNO₃ profiles obtained with the new inversion method.

The first step has been the validation of GBMS measurements of tropospheric opacity, which is a necessary tool in the calibration of any GBMS spectra. This was achieved by means of comparisons among correlative measurements of water vapor column content (or Precipitable Water Vapor, PWV) since, in the spectral region observed by GBMS, the tropospheric opacity is almost entirely due to water vapor absorption. In particular, I compared GBMS PWV measurements collected during the primary field campaign of the ECOWAR project (*Bhawar et al., 2008*) with simultaneous PWV observations obtained with Vaisala RS92k radiosondes (*Rowe et al., 2008*), a Raman lidar (*Di Girolamo et al., 2004*), and an IR Fourier transform spectrometer (*Bianchini et al., 2006*). I found that GBMS PWV measurements are in good agreement with the other three data sets, displaying percentage values for the root mean square of the difference between observations ranging from 9% to 9.6%. Furthermore, the considerable number of data points available for the GBMS versus lidar PWV correlation allowed an additional analysis which indicates negligible

systematic differences between these two data sets. These results are illustrated in *Fiorucci et al* (2008) and *Fiorucci et al* (2009). Moreover, I presented comparisons between the GBMS and additional FTIR data, as a result of the collaboration with Bianchini and coauthors (*Bianchini et al.*, 2010). Noticeably, the two data sets resulted to be consistent within the errors and showed no significant bias.

The second part of the validation consists of a comparison between GBMS HNO₃ profiles and satellite measurements. I compared UARS MLS measurements (1991-1999) (*Livesey et al.*, 2003) with those carried out by the GBMS at South Pole, Antarctica (90°S), during the most part of 1993 and 1995. Systematic differences between GBMS and Aura HNO₃ data sets have been assessed at seven potential temperature levels θ spanning the range 465-960K (19-30 km). This comparison shows that the agreement between UARS MLS and GBMS is within ~15 % between 520 and 740 K (22-27 km) and that the two data sets are consistent, within their errors. I also compared Aura MLS HNO₃ observations (2004 - to date) (*Santee et al.*, 2007) to GBMS measurements obtained during the period February 2004-March 2007, at the mid-latitudes/high altitudes station of Testa Grigia (45.9° N, 7.7° E, elev. 3500 m), and during polar winter 2008/09 at Thule Air Base (76.5°N 68.8°W). A very good agreement, within 5% for all θ levels but the 960 K, has been obtained between the two data sets at Testa Grigia. Conversely, differences as large as 3 ppbv (~40%) have been observed on average near the concentration peak of HNO₃ profiles obtained over Thule. This partial disagreement at Thule is possibly due to an issue related to the ozone background retrieval at this site. Apart from this problem with the ozone background, such site dependent differences are not completely unexpected since some latitude-dependent differences are observed also between MLS and other satellite data sets, such as ACE-FTS, and Odin-SMR (Lucien Froidevaux,, personal communication). Further investigations, including comparisons of MLS HNO₃ with the latter datasets, are planned in order to clarify the issue.

The second part of the validation process has been performed in the framework of the GOZCARDS NASA JPL project, which is aimed at developing a long-term, global data record of the relevant stratospheric constituents in the context of ozone decline. GBMS data have been selected in GOZCARDS to cross calibrate HNO₃ measurements by the UARS and Aura MLS experiments. The GBMS HNO₃ dataset is the only one

spanning a sufficiently long time interval for connecting and calibrating the two satellite datasets. I inferred that no bias correction of MLS data is necessary in order to link the UARS and Aura HNO₃ data sets in the error range obtained combining MLS and GBMS total uncertainties (~20 % at 465 K, below 15% from 520 up to 740 K and ~40% at 960 K)

Appendix A

Evolution of temperature, O₃, CO, and N₂O profiles during the exceptional 2009 Arctic major stratospheric warming as observed by lidar and mm-wave spectroscopy at Thule (76.5°N, 68.8°W), Greenland.

1 **Evolution of temperature, O₃, CO, and N₂O profiles during the exceptional 2009 Arctic**
2 **major stratospheric warming as observed by lidar and mm-wave spectroscopy at Thule**
3 **(76.5°N, 68.8°W), Greenland.**

4
5 Claudia Di Biagio^{1,2}, Giovanni Muscari³, Alcide di Sarra¹, Robert L. de Zafra⁴, Paul
6 Eriksen⁵, Giorgio Fiocco⁶, Irene Fiorucci^{3,7}, and Daniele Fuà⁶

7
8 ¹ ENEA/CLIM-OSS, S. Maria di Galeria, Italy

9 ² Department of Earth Science, University of Siena, Siena, Italy

10 ³ Istituto Nazionale di Geofisica e Vulcanologia, Rome, Italy

11 ⁴ Department of Physics and Astronomy, Stony Brook University, Stony Brook, NY, USA

12 ⁵ Danish Meteorological Institute, Copenhagen, Denmark

13 ⁶ Department of Physics, “Sapienza” University of Rome, Rome, Italy

14 ⁷ Department of Physics, University of Bologna, Bologna, Italy

15
16 **Authors**

17
18 Claudia Di Biagio

19 ENEA/CLIM-OSS, via Anguillarese 301, 00123, S. Maria di Galeria (Rome), Italy

20 Phone: 0039 06 30486127

21 claudia.dibiagio@enea.it

22
23 Giovanni Muscari

24 Istituto Nazionale di Geofisica e Vulcanologia, Via di Vigna Murata 605, 00143, Rome,

25 Italy

26 Phone: 0039 06 51860724

27 giovanni.muscari@ingv.it

28

29 Alcide di Sarra

30 ENEA/CLIM-OSS, via Anguillarese 301, 00123, S. Maria di Galeria (Rome), Italy

31 Phone: 0039 06 30484986

32 alcide.disarra@enea.it

33

34 Robert L. de Zafra

35 Department of Physics and Astronomy, Stony Brook University, New York, USA

36 Phone: 001 631 6328137

37 rdezafra@notes.cc.sunysb.edu

38

39 Paul Eriksen

40 Danish Meteorological Institute, Danish Climate Centre

41 Lyngbyvej 100, DK-2100, Copenhagen, Denmark

42 Phone : 0045 39157418

43 pe@dmi.dk

44

45 Giorgio Fiocco

46 Department of Physics, "Sapienza" University of Rome, Piazzale Aldo Moro 2, 00185,

47 Rome, Italy

48 Phone: 0039 06 49913513

49 giorgio.fiocco@uniroma1.it

50

51 Irene Fiorucci

52 Istituto Nazionale di Geofisica e Vulcanologia, Via di Vigna Murata 605, 00143, Rome,

53 Italy
54 Phone: 0039 06 51860719
55 irene.fiorucci@ingv.it

56

57 Daniele Fuà
58 Department of Physics, “Sapienza” University of Rome, Piazzale Aldo Moro 2, 00185,
59 Rome, Italy
60 Phone: 0039 06 49913515
61 daniele.fua@uniroma1.it

62

63

64

65

66

67

68

69

70

71

72

73

74

75

76

77

78

79
80
81
82
83
84
85
86
87
88
89
90
91
92
93
94
95
96
97
98
99
100
101
102
103
104

Abstract

The 2009 Arctic sudden stratospheric warming (SSW) was the most intense event ever observed. Unique ground-based measurements of middle atmospheric profiles of temperature, O₃, CO, and N₂O obtained at Thule (76.5°N, 68.8°W), Greenland, in the period January – early March are used to show the evolution of the 2009 SSW in the region of its maximum intensity. The first sign of the SSW was detected at ~80 km on 15 January, when a rapid decrease in CO mixing ratio took place. The first evidence of a temperature increase was observed at ~2000 K on 22 January. The warming propagated from the upper to the lower stratosphere in 7 days and the record maximum temperature of 289 K was observed between 1300 and 1500 K potential temperature on 22 January. The vortex splitting was associated with the SSW. Stratospheric backward trajectories indicate that airmasses arriving to Thule during the warming peak underwent a rapid compression and an intense adiabatic warming of up to 50 K. The rapid advection of air from the extra-tropics was also occasionally observed to produce elevated values of N₂O mixing ratio. Starting from mid-February the temperature profile and the N₂O mixing ratio returned to the pre-warming values in the mid- and upper stratosphere, indicating the reformation of the vortex at these levels. In late winter, vertical descent at mesospheric altitudes is estimated from CO profiles at 0.25±0.05 km/day.

INDEX TERMS: 3334 (middle atmosphere dynamics), 0340 (middle atmosphere: composition and chemistry), 0341 (middle atmosphere: constituent transport and chemistry), 3360 (remote sensing)

KEYWORDS: sudden stratospheric warming, winter polar stratosphere, ground-based remote sensing.

105 **1. Introduction**

106 Sudden Stratospheric Warmings are the most important perturbing events that
107 affect the dynamics and thermal structure of the winter stratosphere in the Northern
108 Hemisphere. The 2008/09 Arctic winter has been characterized by the largest major SSW
109 event on record ever observed [*Labitzke and Kunze, 2009; Manney et al., 2009*]. The
110 development of SSWs is linked to the vertical propagation of planetary waves, which
111 dissipate in the mesosphere first and then progressively through the stratosphere, interacting
112 with the westerly winter circulation and modifying the atmospheric thermal profile from the
113 upper troposphere through the mesosphere [*Schoeberl et al., 1978*]. Major warmings produce
114 the breakdown of the winter circulation through either the displacement or the splitting of the
115 polar vortex, the instauration of an easterly circulation, and the reversal of the latitudinal
116 temperature gradient. Strong differences in terms of dynamics, transport, evolution of the
117 stratospheric chemical composition and of the vertical structure of the polar vortex exist
118 between displacement and splitting events [*Charlton and Polvani, 2007; Manney et al.,*
119 *2009; Matthewman et al., 2009*]. Minor events are less intense and do not produce the
120 reversal of the mean zonal circulation.

121 The Arctic stratosphere is characterized by a great interannual variability and very
122 warm winters can alternate with cold ones. The occurrence of SSWs has been shown to be
123 connected to the phase of the Quasi Biennial Oscillation, to the solar cycle [*Labitzke and van*
124 *Loon, 1988*], and to the Southern Oscillation [*van Loon and Labitzke, 1987*]. As discussed by
125 *Charlton and Polvani [2007]*, a frequent occurrence of sudden warmings occurred in the
126 period 1958-2002, and a mean of six major events per decade was observed. Series of minor
127 warmings or single minor events alternate with major SSWs [*Schoeberl, 1978; Manney et*
128 *al., 2005*].

129 An increasing number of large warming events has been registered during the last
130 ten years [*Manney et al.*, 2005]. Before the winter of 2008/09, the most intense recent
131 warmings in the Arctic were detected in 2004 and 2006 [*Manney et al.*, 2005 and 2008].

132 The 2009 SSW to be described here using ground-based observations started in
133 mid-January and was accompanied by an intensification of planetary wave number 2. As the
134 SSW developed, the stratopause lowered and the mean zonal circulation reversed,
135 proceeding from the mesosphere downwards. Studies by *Manney et al.* [2009] (using
136 satellite-based measurements) and by *Labitzke and Kunze* [2009] (using the European Centre
137 for Medium-range Weather Forecast reanalyses) describe the mean evolution of the warming
138 event over the entire Arctic region, thus providing a global view on the 2009 winter. A 10
139 hPa wind reversal at 60°N occurred at around 22 January [*Manney et al.*, 2009]. As the SSW
140 propagated downward, it induced a splitting of the polar vortex in the lower stratosphere.
141 The maximum warming at 10 hPa took place on 24 January above Greenland [*Labitzke and*
142 *Kunze*, 2009]. At the end of January the stratopause disappeared and a quasi-isothermal
143 stratospheric temperature profile was observed. A strong polar vortex reformed very rapidly
144 in the upper stratosphere at the beginning of February. The 10 hPa 60°N westerly circulation
145 was restored at the beginning of March.

146 In this study, ground-based observations of the thermal structure and chemical
147 composition of the middle atmosphere from the Network for Detection of Atmospheric
148 Composition Change (NDACC, <http://www.ndsc.ncep.noaa.gov/>) station at Thule Air Base
149 (76.5°N, 68.8°W), Greenland, were used to show the evolution of the phenomenon and its
150 interactions with the dynamical structure of the polar vortex in the region of maximum
151 warming [*Labitzke and Kunze*, 2009].

152

153

154

155 **2. Measurements**

156 An intensive measurement campaign was conducted at Thule during January–early
157 March, 2009, with a lidar (“Sapienza” University of Rome) and a ground-based millimeter-
158 wave spectrometer (Stony Brook University). The lidar was installed at Thule in 1990 and
159 has been operational during several years, particularly during the winter season [i.e., *di Sarra*
160 *et al.*, 2002 and references therein; *Keckhut et al.*, 2004]. The transmitter of the lidar system
161 is composed by a two stage Nd:YAG laser with second harmonic generator producing
162 linearly polarized pulses of a nominal energy of ~200 mJ at 532 nm, with a repetition rate of
163 10 Hz. The divergence of the laser beam is less than 1 mrad. The receiver includes a 0.8 m
164 diameter Cassegrain telescope and a photon counting acquisition system. The parallel and the
165 cross polarized components of the backscattered signal are separately acquired. A chopper is
166 used to cut off signals from the lowest atmospheric levels in order to prevent the saturation of
167 the photomultiplier tubes. Atmospheric temperature (T) profiles were derived from 25 km up
168 to 70 km altitude by applying the algorithm described by *Marenco et al.* [1997]. T was
169 derived with a vertical resolution of 150 m and averaged over 4.5 km. To reduce the signal-
170 to-noise ratio, the signal was integrated for 1-5 hours, depending on the weather conditions.
171 The estimated 1σ uncertainty varies from ~1 K at 25 km to ~15 K at the maximum probed
172 altitude. National Centers for Environmental Predictions (NCEP) reanalyses over Thule were
173 used to derive temperatures below 25 km.

174 The ground-based millimeter-wave spectrometer (GBMS) has been operated at
175 Thule also during the winters of 2001-2002 and 2002-2003 [*Muscari et al.*, 2007, and
176 references therein]. The GBMS measures rotational emission spectra of atmospheric
177 chemical species such as O₃, N₂O, CO and HNO₃, as well as the H₂O continuum, with a
178 spectral window of 600 MHz tunable between approximately 230 and 280 GHz. It comprises
179 a front end receiver employing a cryogenically cooled SIS mixer and a back end composed
180 of an Acousto-Optical Spectrometer (AOS) [*de Zafra*, 1995]. By means of the observed line

181 shape together with pressure and temperature vertical profiles, a mathematical deconvolution
182 process allows finding the emitting molecule's concentration as a function of altitude from
183 about 15 to 80 km altitude. For water vapor, only the integrated column contents can be
184 obtained [*Fiorucci et al.*, 2008]. O₃ and CO spectra are measured with a ~1.5-hour
185 integration, while HNO₃ and N₂O lines are weaker and need about 3-4 hours of integration.
186 The vertical resolution of the GBMS is limited by the inversion algorithm and averages one
187 pressure scale height: the nominal vertical resolution is 6-8 km, although relative peaks in
188 concentration profiles can be determined within ±1 km altitude. Detailed information on the
189 observing technique, and GBMS data analysis can be found in *de Zafra* [1995], and *Muscari*
190 *et al.* [2007].

191 GBMS retrieval algorithm has recently changed to a standard Optimal Estimation
192 Method (OEM) which was applied to the O₃ and N₂O measurements reported here. Careful
193 comparisons of mixing ratio (mr) profiles obtained with previous (*Muscari et al.* [2007], and
194 references therein) and current algorithms show no significant differences in results and error
195 estimates, with the OEM providing however additional information needed to better
196 characterize the retrievals and compare them to other datasets. Further refinements and
197 validation efforts on O₃ and N₂O OEM retrievals are still underway and results shown here
198 should be considered preliminary. CO retrievals, instead, have not yet undergone such testing
199 and vertical profiles reported in this manuscript are therefore still obtained using the
200 Chahine-Twomey method [*de Zafra and Muscari*, 2004, and references therein]. O₃, N₂O,
201 and CO measurements have an estimated 1σ uncertainty of 13% (minimum 0.3 ppmv), 15%
202 (minimum 5 ppbv), and 16% (minimum 0.1 ppmv), respectively.

203 During January- early March 2009, lidar and GBMS measurements were usually
204 performed on a daily basis, except during periods characterized by poor weather conditions
205 (both instruments, 5-11 February) or instrument malfunctioning (lidar, 16-22 January).

206

207 **3. Results and discussion**

208 **3.1. Temporal evolution of the middle atmosphere thermal structure**

209 Figure 1 shows the temporal evolution of T at different potential temperature (θ)
210 levels between 400 and 2000 K (approximately 16 to 50 km) during the period 14 January –
211 5 March 2009 (days 14-64). In mid-January, before the SSW event, a cold vortex was stably
212 present over Thule. An ozonesonde launched from Thule on 12 January showed that
213 conditions for polar stratospheric cloud (PSC) formation were already reached at that date at
214 an altitude of about 19 km. Type Ia PSC particles were detected by lidar on January 17 and
215 18 between 17 and 19 km. Initial lidar profiles reached only up to \sim 50 km and at this altitude
216 ($\theta \sim$ 2000 K) the first sign of warming was observed on 22 January. The warming reached
217 800-1000 K after 2-4 days (January 24-26), and the region between 400 and 600 K after 6-7
218 days (January 28-29). The value of the maximum T reached at each level due to the
219 downward propagation of the warming decreased approximately linearly with θ from 289 K
220 at layers between 1300 and 1500 K (22 January) to 222 K at level 400 K (30 January). A
221 linear fit to the T maxima observed at the different θ levels versus time (Fig. 1) gives a
222 decrease of 8.2 K/day as the warming proceeded downward. On January 24, at 800 K (\sim 10
223 hPa), we measured a peak temperature of 273 K, consistent with values reported over Thule
224 by *Labitzke and Kunze* [2009] in their Figure 4. The temperature profile became nearly
225 isothermal over the wide range of θ between 600 and 2000 K at the end of January (days 27-
226 28, $T \sim$ 240K), and then between 400 and 1100 K at the beginning of February (days 35-37,
227 $T \sim$ 230 K). From mid-February (days 43-44) to the beginning of March, the temperature
228 profile returned to the pre-warming values at the higher levels (between 1000 and 2000 K),
229 due to polar vortex reformation (see Fig. 4), while remaining up to 30 K warmer than in the
230 pre-warming period at lower levels (900 K and below), where the vortex never restored. On
231 January 22, the stratopause (identified as the height of maximum stratospheric temperature)
232 was observed at about 35 km altitude. It decreased to about 30 km on 25 January. With the

233 development of the isothermal profile a local maximum appeared at about 25 km on the
234 26th, progressively decreasing to 20 km on 29 January. In early February a T maximum
235 appeared near 52 km, and remained between 45 and 55 km until early March. This differs
236 somewhat from the findings of *Manney et al.* [2009] that place the stratopause (this time
237 identified with the atmospheric temperature absolute maximum) at 80 km in early February.
238 It must be noticed, however, that *Manney et al.* [2009] discuss only zonal averages at 80 °N
239 and their temperature maximum is more than 35 K smaller than our observation at 52 km.

240 In order to relate the warming event to the dynamical situation, we calculated
241 temperature variations along 5-day isentropic backward airmass trajectories arriving at
242 Thule. Trajectories were obtained from the NASA-GSFC Automailer system [*Schoeberl and*
243 *Sparling*, 1994] using NCEP reanalysis data. A trajectory a day ending at Thule at 00 UT
244 was used in the analysis. The difference ΔT between the airmass final temperature over
245 Thule and the minimum T reached by the air parcel during its 5-day run is indicative of the
246 adiabatic heating taking place along the trajectory. Figure 2 shows the temporal evolution of
247 ΔT for θ levels between 400 and 2000 K in the period 1 January – 5 March (days 1-64). ΔT
248 is always <10 K at all levels, except when the warming occurs. ΔT for the days of maximum
249 warming is ~ 50 K at 1000+1300 K and between 25 and 45 K at the other selected θ levels.
250 The compression occurs later at the lowest levels, consistently with the evolution of the
251 warming. Thus, the trajectories approaching the polar region during the warming peak were
252 subjected to a rapid compression and an intense adiabatic heating that largely contributed to
253 the total observed warming.

254

255 **3.2 Comparison with recent SSWs**

256 Figure 3 shows the temporal evolution of the temperatures measured by lidar at θ
257 levels between 700 and 2000 K for the winters 2002, 2003, 2007, and 2009, all affected by
258 major warmings. The 2009 SSW was characterized by the largest absolute temperatures and

259 by the largest temperature gradient versus time ever observed at Thule by lidar. The
260 maximum temperature of 289 K at layers between 1300 and 1500 K is up to 40 K larger than
261 maxima observed during winters 2002, 2003, and 2007 and the T gradient peaked at 1300 K
262 with ~ 9 K/day between 14 and 22 January. For the warming of 2006, which was identified as
263 the strongest event of the last decade prior to 2009, *Manney et al.* [2008], in their Figure 3,
264 reported a maximum 70°N zonal mean temperature of 275 K at about 1.5 hPa (~ 1500 K) and
265 a temperature gradient versus time in the maximum warming period that is comparable to
266 what we observed in 2009. Temperatures at 1000 and 1500 K levels were consistently lower
267 throughout February and early March than in the other considered winters.

268

269 **3.3 Chemical composition and vortex evolution**

270 Figure 4 shows the temporal evolution above Thule of Ertel's potential vorticity
271 (PV), T, N₂O, CO, and O₃ mixing ratios, at different θ levels between 500 (~ 18 -20 km) and
272 2000 K (~ 48 -50 km), in the period 14 January – 5 March 2009. The PV values were obtained
273 from the NASA-GSFC Automailer system, based on NCEP data. Estimates of PV values
274 corresponding to the inner vortex edge during January are also reported in Fig. 4. PV values
275 show that the splitting of the vortex progressed from the top downward and took about 8
276 days to reach the lower stratosphere (about 20 January at 2000 K, and 28 January at 500 K).
277 Figure 5 shows a contour plot of CO mr between 50 and 85 km in the period 14 January – 5
278 March (days 14-64). GBMS CO mr values from the mesosphere indicate an initial vortex
279 disruption at 80 km on 15 January, identified as a rapid decrease in CO mr, in agreement
280 with *Manney et al.* [2009]. As apparent in Figure 4, between 1000 and 500 K the vortex
281 break up was accompanied by a sudden increase in N₂O mr which occurred between January
282 26 and 28. The observed increase in N₂O mr was about 0.25, 0.15, 0.10, and 0.08 ppmv at
283 500, 600, 800 K, and 1000 K, respectively. At all these levels, PV and N₂O are in good
284 agreement in identifying the vortex break up (decreasing PV, increasing N₂O), although the

285 exact timing might be slightly off depending on the PV value chosen as indicative of the
286 vortex inner edge.

287 At higher levels, because of the rapid vertical decrease in both nitrous oxide mr and
288 its gradient across the vortex edge, N₂O becomes less reliable in describing the origin of the
289 observed airmasses. Instead, CO becomes a better tool for this purpose [e.g., *de Zafra and*
290 *Muscari*, 2004]. At these levels, the vortex splitting was marked by a rapid decrease in CO
291 mr matching the PV decrease. CO data indicate that at 2000 K and 1500 K the vortex broke
292 up over Thule on January 20-21. CO mr variations during the warming were observed to be
293 about -0.2 and -0.35 ppmv/day at 1500 and 2000 K, respectively. Concurrently, as warm, O₃-
294 rich low and mid-latitude air moved over Thule during the SSW, the GBMS measured an
295 increase in O₃ mr in the upper stratosphere of 0.8 and 0.6 ppmv/day at 1500 and 2000 K,
296 respectively. On late 25 January, shortly after the vortex break up, a decrease in O₃ mr
297 (about 3.6 ppmv) concurrent with a rapid and strong increase in CO mr (about 1.2 ppmv)
298 between 1700 and 2000 K (only level 2000 K is shown in Fig. 4) suggests that a volume of
299 vortex air was advected over Thule at these levels. This filament of vortex air above Thule is
300 not present in the PV reanalysis data. This indicates that GBMS tracers measurements may
301 identify air parcels more accurately than PV reanalyses, which have an inherent coarser
302 temporal and spatial resolution. After such an intense SSW, air parcels in the newly formed
303 vortex can be characterized by very different chemical tracer contents. The history of air
304 masses contained in this re-formed vortex are therefore defined by their tracer concentrations
305 more accurately than by their position inside the vortex (i.e., PV value) and a strict
306 consistency between chemical tracer mr and PV values should not be expected. During
307 February, PV values indicate that the vortex reformed rapidly and strongly at higher levels
308 (between about 6 and 12 February at 2000, 1500, and 1000 K) but not in the lower
309 stratosphere (below about 800 K).

310 At 500 K stable conditions with no vortex reformation were maintained until early
311 March and the observed N₂O mr remained almost constant (about 0.3 ppmv) since the
312 beginning of the SSW event, thus indicating well mixed extra-vortex airmasses, in
313 agreement with what is indicated by 10-day backward trajectories (also obtained by the
314 NASA-GSFC Automailer system). At 800 K, the N₂O mr shows more variability with
315 respect to level 500 K, with larger values from immediately after the warming event (day 27)
316 through mid-February, indicating extra-vortex air masses, and smaller values from day 50 to
317 the end of the campaign, indicating the observation of vortex air. 10-day backward
318 trajectories show airmasses coming from North Africa arriving over Thule on 30 January
319 and on 15 February, therefore explaining the two relative maxima of N₂O mr at 800 K
320 (~0.11 ppmv) observed on these two days. Plots produced using Aura MLS data at 850 K
321 (<http://mls.jpl.nasa.gov/data/gallery.php>) show that complex structures of filaments of both
322 residual and new vortex air formed during February and early March above the entire Arctic
323 area, and the presence of these filaments may in part explain the observed N₂O and O₃
324 variability. At 1000 K, after the SSW event, the N₂O mr rapidly returns to low values,
325 indicating the rapid reformation of a strong vortex with somewhat mixed vortex and mid-
326 latitude air inside.

327 CO mr values at 1000 K and above 2300 K (data not shown) suggest the same
328 considerations, with a rapid return to larger values shortly after the SSW and some variability
329 due to vortex and extra vortex filaments (e.g., a sudden drop on day 42 at 1000 K matching
330 in time the large O₃ mr peak shown in Fig. 4). At 1500 and 2000 K, however, CO does not
331 show the same significant increase in mr from early February onward (see Fig. 4) and the
332 GBMS must be sampling extra-vortex air inside the re-formed vortex, as discussed
333 previously. As shown in Figure 5, from mid-February to early March GBMS observations
334 followed the vertical descent of a CO mr mesospheric peak inside the vortex, which moved
335 from about 70 to 66 km altitude during this period. By applying a linear regression to the

336 peak altitude we estimate a descent rate of late winter mesospheric air of 0.25 ± 0.05 km/day
337 (see Fig. 5); the squared correlation coefficient of the linear regression is 0.82.

338

339 **4. Summary**

340 Ground-based measurements of middle atmospheric profiles of temperature, O₃,
341 CO, and N₂O mr were carried out from Thule, Greenland, during winter 2008-2009. These
342 measurements add further information to previous analyses aimed at studying the evolution
343 of the 2009 winter stratosphere and to tracking the exceptional SSW that occurred during the
344 second half of January. Main findings of this analysis are:

345

346 1. In the first part of January the polar vortex was stable and cold. PSCs were
347 detected between 17 and 19 km on 18-19 January.

348

349 2. The SSW event was initially detected at about 80 km on January 15 by a rapid
350 decrease in CO mr. The first evidence of a temperature increase was observed at $\theta \sim 2000$ K
351 on 22 January. The warming progressed downward reaching level 400 K on 29 January. The
352 maximum T, 289 K, was observed at layers between 1300 and 1500 K on 22 January. In late
353 January the temperature profile became near isothermal, particularly in the altitude layer
354 between 400 and 1100 K.

355

356 3. Backward trajectories at the various altitudes studied indicate that airmasses
357 approaching the polar region during the warming peak were subjected to a rapid
358 compression and an intense adiabatic warming. This is estimated to maximize with $\Delta T \sim 50$
359 K at $\sim 1000 \div 1300$ K.

360

361 4. The vortex break up was marked by a sudden increase in N₂O and decrease in
362 CO mixing ratios below and above 1000 K, respectively. PV, N₂O, and CO are in good
363 agreement in identifying the vortex break up. The vortex reformed rapidly and strongly
364 above 1000 K at the beginning of February, but not in the lower stratosphere. Rapid changes
365 in N₂O, O₃, and CO are associated with the advection of airmasses of different origins, in
366 some cases not detected by PV analyses. Maxima in N₂O mr in late January and mid
367 February are associated with rapid transport of extra-tropics airmasses.

368

369 5. Mesospheric CO measurements inside the reformed vortex indicate a descent rate
370 at ~68 km of 0.25±0.05 km/day from mid-February to early March.

371

372 **Acknowledgements**

373 This work was supported by the project PRIN 2007 (“Dirigibile Italia”), funded by
374 the Italian Ministry for University and Research, and by the Italian Antarctic Program. We
375 would like to thank NSF and Susan Zager of CH2M HILL Polar Services for logistic
376 support, and NASA-GSFC for the trajectory Automailer system. We are grateful to C.
377 Cesaroni for his assistance during the field campaign. Contributions by S. E. Ascanius, M.
378 Cacciani, G. Casasanta, V. Ciardini, T. Di Iorio, and C. Tirelli are gratefully acknowledged.

379

380

381

382

383

384

385

386

387
388
389
390
391
392
393
394
395
396
397
398
399
400
401
402
403
404
405
406
407
408
409
410

References

- de Zafra, R. L. (1995), The ground-based measurements of stratospheric trace gases using quantitative millimeter wave emission spectroscopy, in *Diagnostic Tools in Atmospheric Physics, Proc. of the Int. Sch. of Phys. "Enrico Fermi"*, vol. 124, 23– 54, Soc. It. di Fis., Bologna, Italy.
- de Zafra, R. L., and G. Muscari (2004), CO as an important high-altitude tracer of dynamics in the polar stratosphere and mesosphere, *J. Geophys. Res.*, 109, D06105, doi:10.1029/2003JD004099.
- di Sarra, A., M. Cacciani, G. Fiocco, D. Fuà, and T. S. Jørgensen (2002), Lidar observations of polar stratospheric clouds over northern Greenland in the period 1990-1997, *J. Geophys. Res.*, 107(D12), doi:10.1029/2001JD001074.
- Fiorucci, I., et al. (2008), Measurements of low amounts of precipitable water vapor by millimeter wave spectroscopy: An intercomparison with radiosonde, Raman lidar, and Fourier transform infrared data, *J. Geophys. Res.*, 113, D14314, doi:10.1029/2008JD009831.
- Keckhut, P., et al. (2004), Review of ozone and temperature lidar validations performed within the framework of the Network for the Detection of Stratospheric Change, *J. Environ. Monit.*, 6, 721–733
- Labitzke, K, and H. Van Loon (1988), Associations between the 11-year solar cycle, the QBO and the atmosphere. Part I: The troposphere and the stratosphere in the Northern Hemisphere winter, *J. Atmos. Terr. Phys.*, 50, 197-206.
- Labitzke, K, and M. Kunze (2009), On the remarkable Arctic winter 2008/2009, *J. Geophys. Res.*, 114, D00I02, doi:10.1029/2009JD012273.

411 Manney, G. L., et al. (2005), The remarkable 2003-2004 winter and other recent warm
412 winters in Arctic stratosphere since 1990s, *J. Geophys. Res.*, *110*, D04107,
413 doi:10.1029/2004JD005367.

414 Manney, G. L., et al. (2008), The evolution of the stratopause during the 2006 major
415 warming: Satellite data and assimilated meteorological analyses, *J. Geophys. Res.*, *113*,
416 D11115, doi:10.1029/2007JD009097.

417 Manney, G. L., et al. (2009), Aura Microwave Limb Sounder observations of dynamics and
418 transport during the record-breaking 2009 Arctic stratospheric major warming,
419 *Geophys. Res. Lett.*, *36*, L12815, doi:10.1029/2009GL038586.

420 Marenco, F., et al. (1997), Thermal structure of the winter middle atmosphere observed by
421 lidar at Thule, Greenland, during 1993-1994, *J. Atmos. Sol-Terr. Phys.*, *59* (2), 151-
422 158.

423 Matthewman, N. J., J. G. Esler, A. J. Charlton-Perez, A. J., Polvani, L. M.(2009), A new
424 look at stratospheric sudden warmings. Part III: Polar vortex evolution and vertical
425 structure, *J. Clim.*, *22*, 1566-1585.

426 Muscari, G., et al. (2007), Middle atmospheric O₃, CO₂, N₂O, HNO₃, and temperature
427 profiles during the Arctic winter 2001-2002, *J. Geophys. Res.*, *112*, D14304,
428 doi:10.1029/2006JD007849.

429 Rodgers, C. D. (2000), *Inverse Methods for Atmospheric Sounding: Theory and Practice*,
430 World Sci., Singapore.

431 Schoeberl, M.R., (1978), Stratospheric warmings: observations and theory, *Rev. Geophys.*
432 *and Space Ge.*, *16* (4), 521-538.

433 Schoeberl M.R., and L. C. Sparling (1994), Trajectory Modelling; *Diagnostic Tools in*
434 *Atmospheric Physics, Proc. S.I.F. Course CXVI*, edited by G. Fiocco and G. Visconti,
435 North-Holland, Amsterdam, 1994.

436 Van Loon, H., and K. Labitzke (1987), The Southern Oscillation. Part V: the anomalies in
437 the lower stratosphere of the Northern Hemisphere in winter and a comparison with the
438 Quasi-Biennial Oscillation, *Mon. Weather Rev.*, *115*, 357-369.

439
440
441
442
443
444
445
446
447
448
449
450
451
452
453
454
455
456
457
458
459
460
461

462 **Figure captions**

463

464 Figure 1. Temporal evolution of stratospheric temperature interpolated at different θ levels
465 between 400 and 2000 K (temperatures at 400, 500, and 600 K are from NCEP reanalyses)
466 in the period 14 January – 5 March (days 14-64). The maximum 1σ uncertainty at the
467 different levels is indicated by vertical bars. The maximum temperature obtained at each
468 level due to the downward propagation of the warming is highlighted by a circle; a linear fit
469 of T maxima versus time is also shown (dashed line).

470

471 Figure 2. Temporal evolution of the temperature difference (ΔT) between the airmass final T
472 over Thule and the minimum T reached by the air parcel along 5-day isentropic backward
473 airmass trajectories for θ levels between 400 and 2000 K in the period 1 January – 5 March
474 (days 1-64).

475

476 Figure 3. Temporal evolution of the temperature measured by lidar at various θ levels
477 between 700 and 2000 K for the winters 2002, 2003, 2007, and 2009, all characterized by
478 major warming events.

479

480 Figure 4. Temporal evolution of: a) Ertel's potential vorticity ($1 \text{ PVU} = 1 \text{ K m}^2 \text{ kg}^{-1} \text{ s}^{-1}$), N_2O
481 and CO mr; b) O_3 mr and temperature, at θ levels between 500 and 2000 K in the period 14
482 January – 5 March (days 14-64). Temperatures at 500 and 600 K are from NCEP reanalysis.
483 Horizontal dashed lines are indicative threshold values for the inner vortex edge.

484

485 Figure 5. Contour plot of CO mr between 50 and 85 km in the period 14 January – 5 March
486 (days 14-64). A linear fit to CO mr peak altitude versus time for the period mid February –
487 early March is also shown (solid line).

Figure 1. Temporal evolution of stratospheric temperature interpolated at different θ levels between 400 and 2000 K (temperatures at 400, 500, and 600 K are from NCEP reanalyses) in the period 14 January - 5 March (days 14-64). The maximum 1σ uncertainty at the different levels is indicated by vertical bars. The maximum temperature obtained at each level due to the downward propagation of the warming is highlighted by a circle; a linear fit of T maxima versus time is also shown (dashed line).

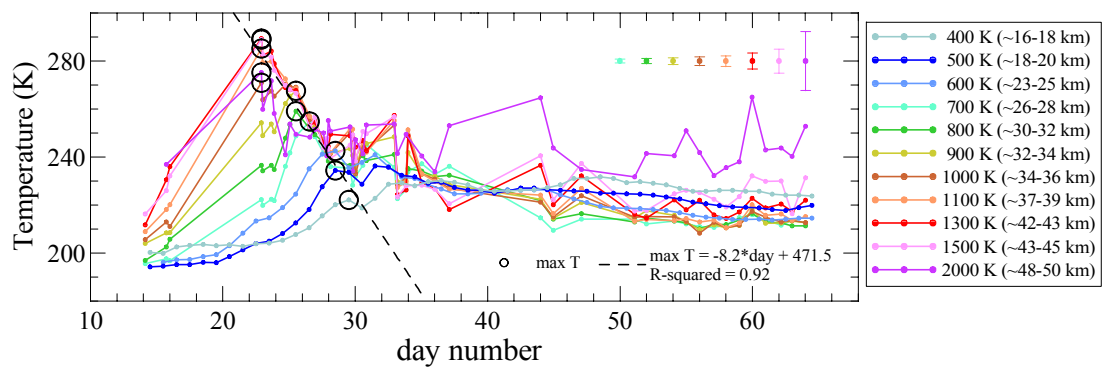


Figure 3. Temporal evolution of the temperature measured by lidar at various θ levels between 700 and 2000 K for the winters 2002, 2003, 2007, and 2009, all characterized by major warming events.

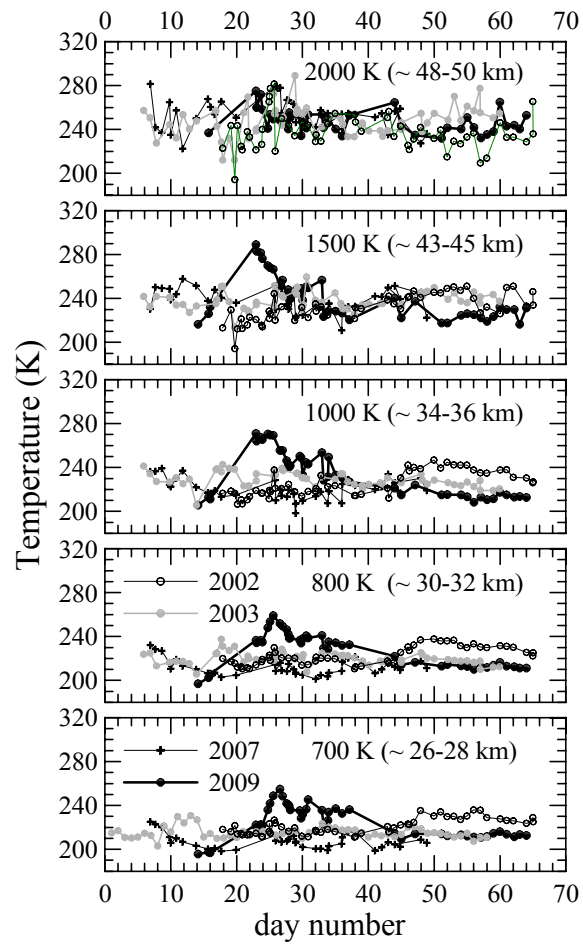


Figure 4. Temporal evolution of: a) Ertel's potential vorticity ($1 \text{ PVU} = 1 \text{ K m}^2 \text{ kg}^{-1} \text{ s}^{-1}$), N_2O and CO mr; b) O_3 mr and temperature, at θ levels between 500 and 2000 K in the period 14 January - 5 March (days 14-64). Temperatures at 500 and 600 K are from NCEP reanalysis. Horizontal dashed lines are indicative threshold values for the inner vortex edge.

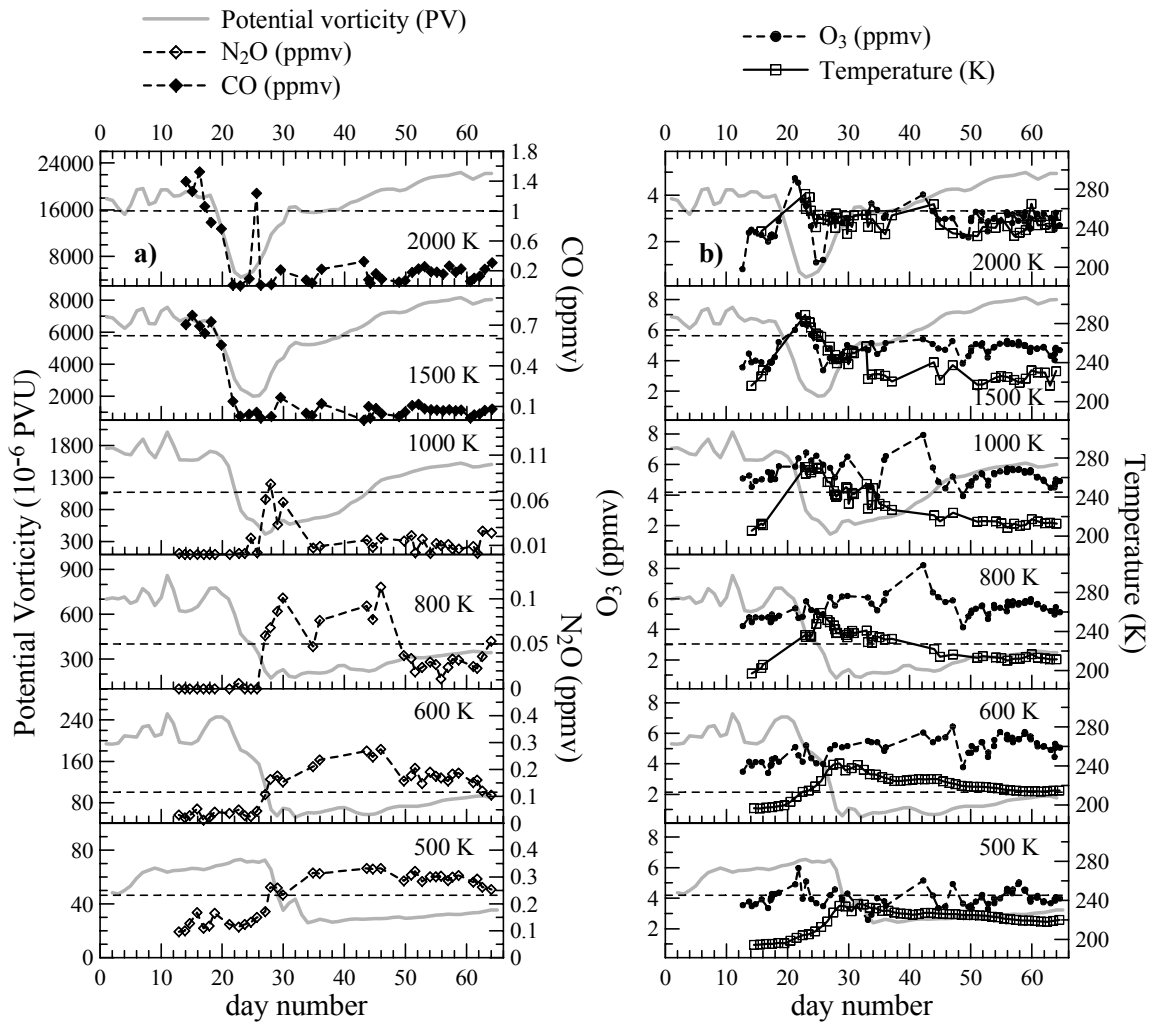
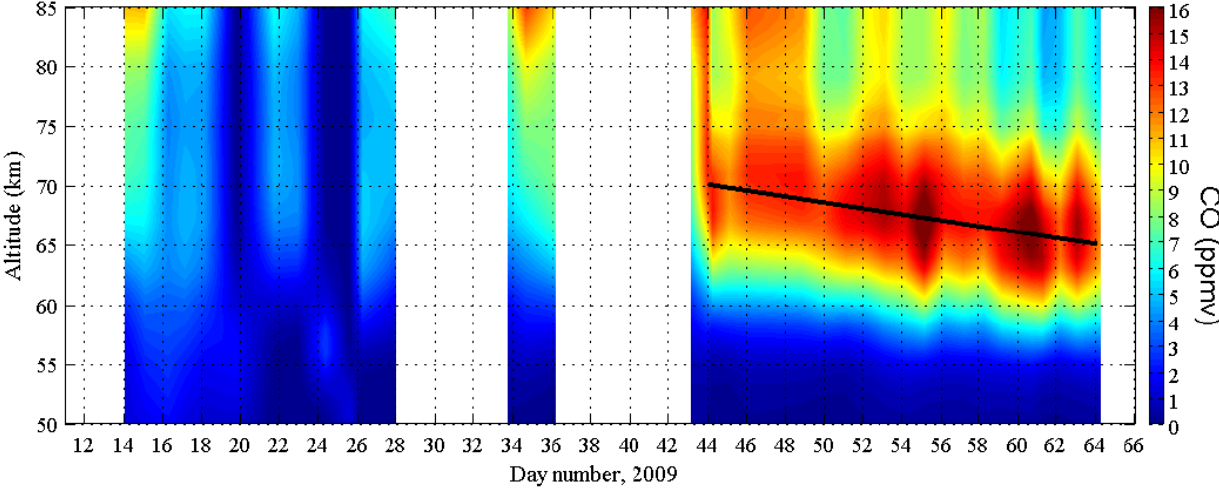


Figure 5. Contour plot of CO mr between 50 and 85 km in the period 14 January – 5 March (days 14-64). A linear fit to CO mr peak altitude versus time for the period mid February – early March is also shown (solid line).



Appendix B

Water vapor sounding with the far infrared REFIR-PAD spectroradiometer from a high-altitude ground-based station during the ECOWAR campaign

Water vapor sounding with the far infrared REFIR-PAD spectroradiometer from a high-altitude ground-based station during the ECOWAR campaign

G. Bianchini¹, L. Palchetti¹, G. Muscari², I. Fiorucci², P. Di Girolamo³, and T. Di Iorio⁴

¹Istituto di Fisica Applicata “Nello Carrara”, Firenze, Italy

²Istituto Nazionale di Geofisica e Vulcanologia, Roma, Italy

³Dipartimento di Ingegneria e Fisica dell’Ambiente, Universit della Basilicata, Potenza, Italy

⁴Dipartimento di Fisica, Universit di Roma “La Sapienza”, Roma, Italy

Abstract. The REFIR-PAD spectroradiometer has been operated from Testa Grigia Italian-Alps station in March 2007 during the Earth COoling by WATER vapouR emission (ECOWAR) measurement campaign, obtaining downwelling radiance spectra in the 100-1100 cm⁻¹ range, in clear sky condition and in presence of cirrus clouds. The analysis of these measurements has proven that the instrument is capable of determining the precipitable water vapor with a total error of 5–7%. The measurement is unaffected by the presence of cirrus, which optical depth can be instead retrieved as an additional parameter. Information on the vertical profiles of water vapor volume mixing ratio and temperature can also be retrieved for three levels. The capability of measuring the water vapor column with a simple, uncooled instrument, capable of operating continuously and with a time resolution of about 10 minutes makes the REFIR-PAD instrument an interesting alternative for meteorological and climatological studies involving the water vapor distribution.

tration can also be used to develop and check atmospheric models (Clough et al. (1992)).

The vertical distribution of water vapor is typically measured for meteorological applications by using radionsounding systems. Although such measurements can also be used for climate studies (Elliott et al. (1991)), they are limited by accuracy (Vömel et al. (2007)) and by a low temporal acquisition rate which prevents the application for characterizing rapid atmospheric phenomena. Other measurements methods exploit the spectral features of water vapor either using passive spectroscopy, from microwave to infrared spectral regions, or using active Raman lidars (England et al. (1992); Divakarla et al. (2006)).

In this paper we describe the inversion method developed to retrieve the PWV and a few parameters of the vertical profile from the far infrared spectral region of the pure rotational water vapor band. These measurements have been performed by the Radiation Explorer in the Far-InfraRed - Prototype for Applications and Development (REFIR-PAD) spectroradiometer (Bianchini et al. (2006)), which has been developed in the framework of the REFIR studies (Rizzi et al. (2001); Palchetti et al. (1999)), for the characterization of the Earth’s emitted radiance from the far- to mid-infrared spectral region (Sinha and Harries (1995)).

The REFIR-PAD instrument is a Fourier transform spectroradiometer designed to operate both from balloon platform, in the nadir and limb view observation geometries (Palchetti et al. (2006); Palchetti et al. (2007)), and from ground in the zenith looking geometry (Bianchini et al. (2007)). In the latter configuration, the instrument was operated in March, 2007 from 3480 m a.s.l. during the Earth COoling by WATER vapor Radiation (ECOWAR) campaign (Bhawar et al. (2008)). A comparison/validation among the PWV values retrieved with the REFIR-PAD measurements and the PWV values measured with the other sensors deployed in the campaign: radionsondes, a Raman lidar and a millimeter-wave spectrometer, has already been performed

1 Introduction

Water vapor is a key atmospheric component to be measured with great accuracy for both meteorological applications and climatological studies. Due to its intense absorption bands, water vapor plays a important role in the Earth radiation balance (Kiehl et al. (1997)). Despite that, there are some important issues to be fully addressed, such as for example its radiative feedback effect. A better understanding of the water vapor climatological behavior requires the characterization of its atmospheric concentration at different altitude and in different sky and atmospheric conditions. The precipitable water vapor (PWV), i.e. the column amount of water vapor present in the atmosphere, or the vertical profile of concen-



Fig. 1. The REFIR-PAD instrument installed outside the Testa Grigia station at 3480 m a.s.l. in the Italian-Swiss Alps.

only for measurements in coincidence with the radiosonde launches (Fiorucci et al. (2008)). In this paper we perform an in-depth analysis by comparison PWV with all the available data and at the maximum acquisition frequency of 10 minutes.

2 Field campaign

The ECOWAR campaign was performed from the Testa Grigia station (Plateau Rosa, 3480 m a.s.l., 45.933° N, 7.7° E), owned by the Italian Consiglio Nazionale delle Ricerche (CNR) and, 5 km apart, from Breuil-Cervinia (1990 m a.s.l., 45.933° N, 7.6° E) in the Italian-Swiss Alps near Aosta.

REFIR-PAD was installed at Testa Grigia in a heated and thermally insulated enclosure just outside of the station (see Fig. 1). The instrument input port had no windows, thus was protected by a chimney to avoid deposition of ice crystals carried by the wind on the input optics.

The instrument was operated for a total of 61 hours of measurements, distributed across 11 days, including daytime and nighttime, with widely varying meteorological conditions both in terms of water vapor concentrations and cirrus cloud presence. Table 1 reports date, time and sky condition for all the acquired measurements.

The other measurements that are used for the comparison/validation of the parameters retrieved from the REFIR-PAD measurements are:

- PWV measured with the Ground-Based Millimeter wave Spectrometer (GBMS), designed and built at the Physics and Astronomy Department of the State Univer-

Table 1. Data available from the ECOWAR campaign. TG: Testa Grigia station, BC: Breuil-Cervinia.

Site	Date	Time (UTC)	Sky conditions
TG	4 March 2007	19:20–23:39	cirrus (8–12 km)
TG	5 March 2007	17:54–0:43 (+1 d)	mostly clear
TG	9 March 2007	7:25–13:53	cirrus (7–11 km)
TG	11 March 2007	16:22–2:06 (+1 d)	clear
TG	12 March 2007	8:44–15:45	clear
TG	12 March 2007	17:55–23:02	clear
TG	13 March 2007	9:15–14:03	clear
TG	13 March 2007	18:21–8:04 (+1 d)	clear
BC	15 March 2007	15:14–23:09	clear

sity of New York at Stony Brook, and operated on the Testa Grigia site by the Istituto Nazionale di Geofisica e Vulcanologia (Fiorucci et al. (2008));

- vertical profiles of water vapor concentration and temperature measured with the University of Basilicata Raman lidar system (BASIL) installed at Breuil-Cervinia (Di Girolamo et al (2004) Di Girolamo (Marchese));
- vertical profiles of water vapor concentration and temperature measured with Vaisala RS92k radiosondes launched from Breuil-Cervinia (Miloshevich et al. (2004)).

On 15 March, the REFIR-PAD was transferred down to Breuil-Cervinia to perform simultaneous co-located measurements with the sensors there installed, in particular the BASIL lidar and the Fourier transform infrared (FTIR) ABB Bomem spectroradiometer Serio et al (2004).

More information on the whole set of measurements and on the comparison with the FTIR/ABB spectroradiometer can be found in Bhawar et al. (2008).

The main REFIR-PAD level 1 data product is the calibrated downwelling spectral radiance, measured in the 100–1100 cm^{-1} spectral range, even if, for ground-based measurements, atmospheric water vapor absorption sets a low-frequency limit to the useful range to about 250–350 cm^{-1} . The level 1 data analysis, including calibration issues and uncertainty characterization, is treated elsewhere (Bianchini et al. (2008)).

During the ECOWAR campaign, the instrument was operated only in visually clear sky conditions, so the only type of cloud that is of some concern in the analysis of REFIR-PAD data is thin/subvisible cirrus. Values of PWV as low as less than 0.5 mm were detected, with a typical value of about 2 mm and peaks of 3–4 mm. In figure 2 two measured spectra are shown, in two extreme cases, 0.5 mm and 3 mm of PWV.

Different condition were detected even in terms of water vapor variability, with days of extremely stable atmospheric conditions with a constant PWV over hours, and days of

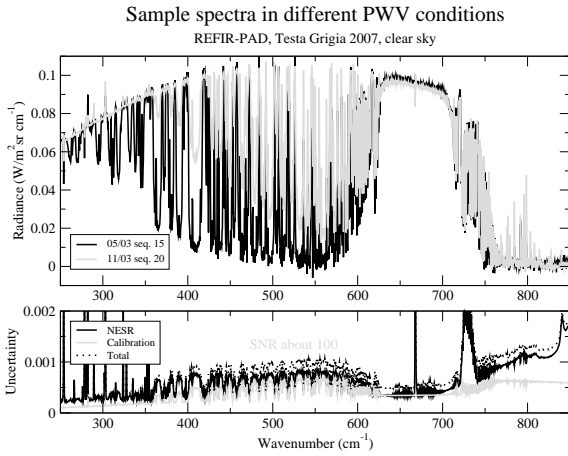


Fig. 2. Two REFIR-PAD calibrated downwelling radiance spectra acquired in different atmospheric conditions: 0.5 mm of PWV (black curve) and 3 mm of PWV (grey curve). Measurement uncertainty is shown in the bottom panel: random (NESR), systematic (calibration) and total.

strong variability in which the REFIR-PAD capability of continuous measurement with high temporal resolution was put to test.

3 Atmospheric variables retrieval

The level 2 analysis of the calibrated spectral radiances has been performed through the best fitting of an atmospheric forward model with respect to a chosen subset of atmospheric parameters, including 1 to 3 levels on which the water vapor and temperature profiles are interpolated, cloud extinction coefficient, and instrumental parameters like lineshape correction and frequency calibration factors. The latter will be treated in section 4, while cloud parameterization is described in section 5.

The forward model used in the analysis is the Line-By-Line Radiative Transfer Model (LBLRTM) from AER Inc. (Clough et al. (2005); Shephard et al. (2009)). The model choice has been driven by a number of features that are needed for the REFIR-PAD data analysis and are provided by LBLRTM:

- An up-to-date spectroscopic database (AER v. 2.2) including HITRAN 2004 and successive updates (Rothman et al. (2005), Gordon et al. (2007))
- MT_CKD v. 2.4 self- and foreign-broadened water vapor and CO₂ continua (Mlawer et al. (2009))
- Modeling of CO₂ line coupling and updates to CO₂ continuum and lineshape according to Niro et al. (2005)

The fitting is obtained through a chi square minimization routine without a-priori constraints on the parameters, apart

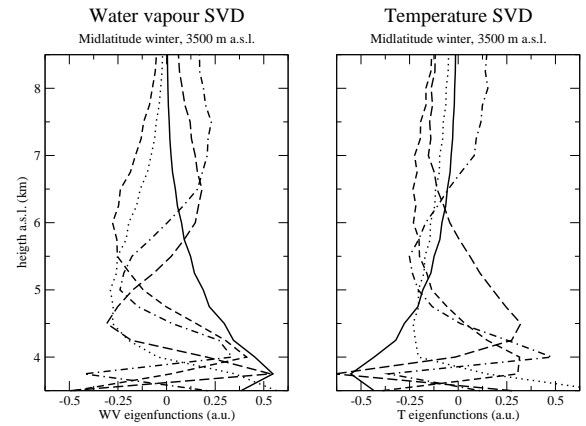


Fig. 3. Weighting functions for water vapor and temperature obtained from REFIR-PAD measured downwelling radiance spectra.

physical upper and lower limits on some of them to avoid anomalous behavior of the fitting routine and convergence problems. These limits are anyway orders of magnitude away from actual fitting results and do not provide a source of external information to bias the results.

Among the atmospheric variables that show signatures in the REFIR-PAD operating range, we concentrate our attention on water vapor and temperature, so the actual spectral range that is used in the analysis is a sub-interval of the REFIR-PAD operating band, extending from about 400 to 850 cm⁻¹. In this region we have the far-infrared to detect water vapor rotational band, the CO₂ v₂ band to provide temperature sensitivity and a part of the atmospheric transparency window to provide continuum and clouds.

The choice of the atmospheric parameters to be used in the fit must take into account the low vertical resolution obtained with the vertical sounding geometry, that in the zenith observation case is further reduced due to the fact that the denser atmospheric layers appear first in the line of sight, reducing the sensitivity to upper layers.

Weighting functions, obtained from the singular value decomposition (SVD) of water vapor and temperature Jacobians, are shown in figure 3. The measurement sensitivity to these parameters decreases rapidly with height and is significant only in an interval of about 3-4 km above ground. The vertical resolution also decreases with height, since the weighting functions get smoother at higher altitudes.

The baseline choice for the vertical profile analysis is to fit a water vapor and temperature value at 1 km above ground, and a second point at 3 km above ground. Levels of the profiles between the two fitted points are interpolated (logarithmically for water vapor and linearly for temperature), while levels above and below fitted points are obtained rescaling the mid-latitude winter standard atmospheric profiles accordingly to the fitted values.

The possibility of fitting 3 and 4 levels per profile, adding one or two near ground level for both water vapor and temperature, thus exploiting the higher information content of the lower levels that can be seen in figure 3, has also been explored.

Moreover, a fitting with only one parameter per profile (i. e. just rescaling standard profiles) has been used in section 6 to estimate uncertainty on the total water column without being affected by correlation between fitted points.

It should be noted that the use of two fitted parameters per profile provides improved PWV values with respect to simple rescaled profiles due to better fitting of the actual atmospheric vertical structure, while the variation between PWV values obtained with 3 and 4-point fitting with respect to 2-point fitting, if present, is well within uncertainty. Correlation between fitted points instead, increases and can cause profile instabilities. For this reason the use of more than 4 fitted parameters per profile appears to be difficult without the use of a-priori constraints.

Fitting times have been estimated on an Intel Xeon E5504 2GHz, obtaining about 30 minutes for the 1-point fitting, 50 minutes for the 2-point and 80 minutes for the 3-point.

4 Instrumental parameters fitting

A subset of the fitted parameters is used to take into account systematic effects due to the instrument, these parameters are:

- A frequency scale calibration factor
- An apodization effect on the instrumental line shape (ILS)

As described in (Bianchini et al. (2008)), frequency calibration of REFIR-PAD spectra is performed calculating the reference laser frequency through the use of atmospheric line centers. It is possible anyway that the laser frequency varies both due to laser diode aging and extreme thermal excursions as can be experienced during measurement campaigns. To avoid performing a calibration on a per-spectrum basis, as could be required in certain cases, a frequency shift factor has been included in the fitted parameters. This factor does not affect in any way the retrieval of atmospheric variables since is almost completely uncorrelated with them.

Another effect that can derive from thermal excursions is the interferometer misalignment. The loss of signal due to misalignment is well taken care of in the radiometric calibration procedure (see Bianchini et al. (2008)), but the ILS variations that are associated to misalignment must be taken into consideration in the level 2 analysis. The simplest way to model this effect is to assume a linear decrease in the fringe contrast with the variation of path difference, i. e. a trapezoidal apodization function. This translates to an ILS that is a linear combination of *sinc* and *sinc*² components. The

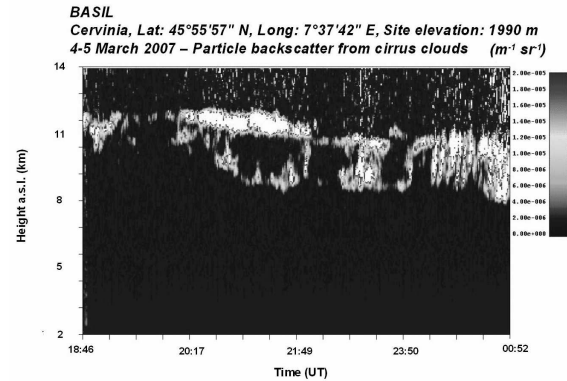


Fig. 4. Backscatter plot acquired from the BASIL lidar at Cervinia on the night of the 4th of March, 2007. Cirrus clouds at about 9-11 km are present during the whole acquisition period.

percentage of pure *sinc* component is thus fitted as a separate parameter to provide lineshape correction for misalignment. Even in this case the correlation with atmospheric parameters is low and can be neglected.

5 Treatment of cirrus cloud

While REFIR-PAD measurements are generally performed in clear sky conditions, it is possible that a cloud cover appears during a measurement run. Of particular interest is the case of a thin, possibly subvisible, cirrus.

This kind of cloud is not easily detected visually, moreover appears at altitudes that are well above the measurement sensitivity range identified in section 3 for the water vapor and temperature profiles. This opens the possibility to perform fitting, and provide an accurate measurement of the atmospheric variables, also in presence of thin clouds.

The simple cloud model included in the LBLRTM software is derived by the LOWTRAN5 routines (Kneizys et al. (1980)) and provides modeling for standard and subvisible cirrus. A single cloud layer can be identified by cloud bottom (CB), layer thickness and extinction coefficient expressed in km^{-1} at $0.55 \mu\text{m}$.

Only extinction coefficient is fitted, since fitting results are not dependent on cloud geometry if CB is higher than the water vapor/temperature sensitivity range. In fact, the latter, as shown in section 3, is 3-4 km above ground, and cirrus generally situates at higher altitudes.

In figure 4, as an example, is shown a plot of the backscatter ratio for the night of the 4th of March, 2007 as measured by the BASIL lidar in Cervinia. In the plot a cirrus layer at the altitude of about 9-11 km is clearly visible.

In figure 5 is shown the analysis of REFIR-PAD spectra acquired in the same day, performed without cloud modeling (thick solid line) and with a modeled cloud layer of 2 km of

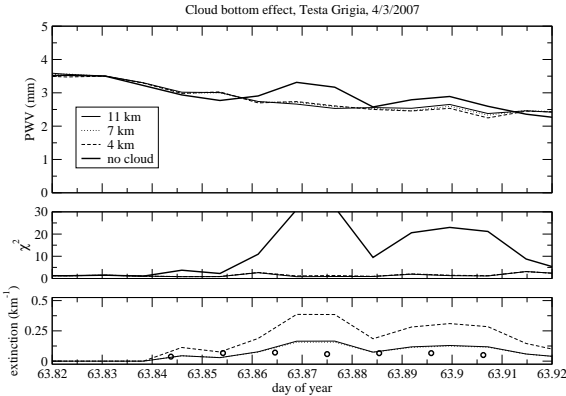


Fig. 5. Effect of different cloud parameterization on fitting results: A subvisible cirrus cloud layer 2 km thick with cloud bottom at 4 km (dashed line), 7 km (dotted line) and 11 km (solid line) has been used. Results obtained without clouds (thick solid line) are also shown. In the bottom panel, cloud extinction as measured by the BASIL lidar is also shown (as circles) for reference.

thickness and CB heights of 4, 7 and 11 kilometers (dashed, dotted and solid lines respectively). It is clearly visible that a fitting process without cloud modeling gives wrong, overestimated, PWV values (top panel) when cloud optical density is not negligible. The effect is even more evident in the χ^2 plot (center panel).

If we look at the bottom panel of figure 5, in which the retrieved cloud extinction coefficient is shown, we see also that there is no difference between the retrievals performed with CB at 7 and 11 kilometers, this because, as explained before, the modeled cloud layer is above the water vapor/temperature sensitivity region. The curve corresponding to a CB of 4 km instead gives greatly overestimated values.

As a reference, cloud extinction as measured by the BASIL lidar is also shown in the bottom panel of figure 5 (as circles), and provides a reasonable agreement with the REFIR-PAD retrieved values, considering the not exact spatial coincidence of the two measuring stations.

6 PWV measurement error

Due to some parameter correlation, the errors on the fitted atmospheric variables obtained from this analysis depends on the number of points fitted per profile. However correlation does not affect the accuracy on the measurement of PWV column since the correlation generally induces some degree of profile instability, in the form of oscillations, but that does not alter the retrieved total water column. This can be seen from the relatively small adjustments that occur in PWV retrieval using a different number of fitted parameters in the atmospheric profiles (figure 6).

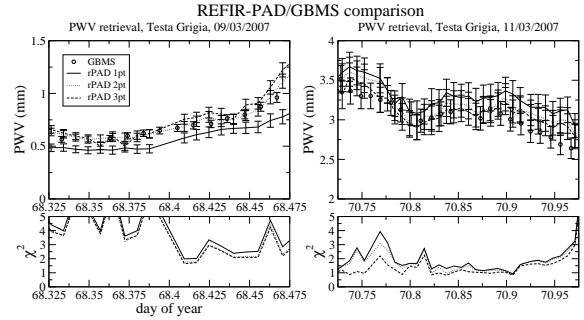


Fig. 6. Total precipitable water vapor (PWV) measured from REFIR-PAD retrieved from spectra acquired on March 9th and 11th, 2007. Chi square values and retrieved cloud extinction are also shown.

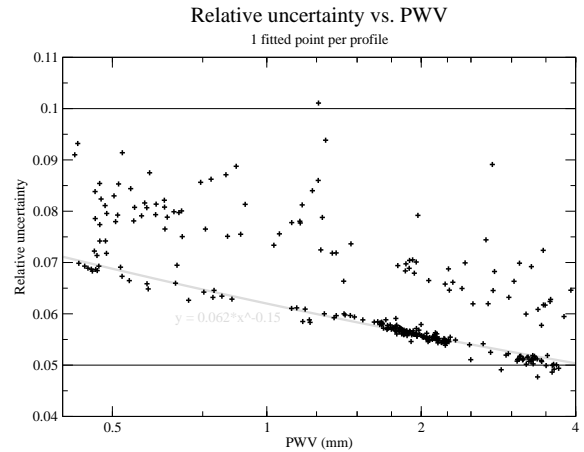


Fig. 7. Relative error on PWV, as obtained from 1-point fitting, plotted versus PWV itself to show relation between the two quantities.

A better estimate of the actual error on PWV can thus be obtained from the relative uncertainty on water profile when fitting a single parameter per profile, i. e. just rescaling the initial guess. In figure 7 is shown a plot of the relative uncertainty obtained with this method vs. the retrieved PWV. Values are always below 10%, the most of them being between 5% and 7%.

It should be noted that most of the points appear also to be situated on a line corresponding to a power law ($y = 0.062 \cdot x^{-0.15}$), while outliers are well explained with excess noise due to external causes (wind, for example, since the instrument was installed outside the research station).

Effects coming from the correlation between water vapor parameter and the other fitted parameters in the 1-point per profile analysis used to assess PWV error has been estimated as negligible. As shown in section 4, instrumental parameters are uncorrelated with atmospheric variables. The effect of the error on temperature profile rescaling (also included in

the 1-point analysis), has been estimated and resulted at least an order of magnitude lower than the error from water vapor fitting, so it can also be neglected.

7 Results and validation

PWV values retrieved from the analysis of REFIR-PAD spectra have been validated through the comparison with the values obtained from the GBMS instrument, operated at Testa Grigia near REFIR-PAD.

The GBMS measures atmospheric emission spectra in the interval between 7.7 and 9.3 cm^{-1} with a maximum time resolution of 10 s . During the ECOWAR campaign measurements were averaged over a time intervals of 15 minutes, that is about the same acquisition time that is needed for a REFIR-PAD spectrum. The conversion of the micro-wave radiances to PWV is described in de Zafra et al. (1983).

The spatial coincidence between the GBMS and the REFIR-PAD instruments is rather good, being only a few tens of meters of distance between them. However it must be taken into account that while the REFIR-PAD operates in a zenith-looking observation geometry, the GBMS observes the atmosphere in a more or less horizontal line of sight, directed towards the North.

In figure 6 is shown a comparison between the PWV values obtained from the GBMS (circles) and the values from REFIR-PAD (1-point fit: solid line, 2-points: dotted line, 3-points: dashed line). Two cases are considered, a rather high (about 3 mm) and a low (0.5 mm) water vapor conditions. The accuracy and time resolution of the two instruments is comparable and the results agree within the errors, for the 2- and 3-points fit. It should be noted that the 1-point fit has a detectable offset from the GBMS value, showing that the use of more profile points adds information to the results.

In figure 8 is shown a scatter plot of all the REFIR-PAD PWV measurements, in the 2-points fitting case, vs. coincident GBMS values. Even in this case the agreement is good within the error, and no significant bias is present.

To assess the information on vertical water vapor profile that can be obtained from REFIR-PAD spectra, a comparison has been made with the BASIL lidar system, that is capable to perform vertical soundings of water vapor and temperature through the rotational Raman Lidar technique in the UV, backscatter at 355 , 532 and 1064 nm , and particle extinction and depolarization at 355 and 532 nm .

Measurements are performed both in day-time and night-time. For a time resolution of 5 minutes and a vertical resolution of 150 m , day-time measurement uncertainty at 2 km altitude is typically 5% for the particle backscattering coefficient (at all wavelengths), 20% for the particle extinction coefficient, 10% for water vapor mixing ratio and 2 K for temperature. The nighttime measurement uncertainty at 2 km is typically 2% for the particle backscattering coefficient,

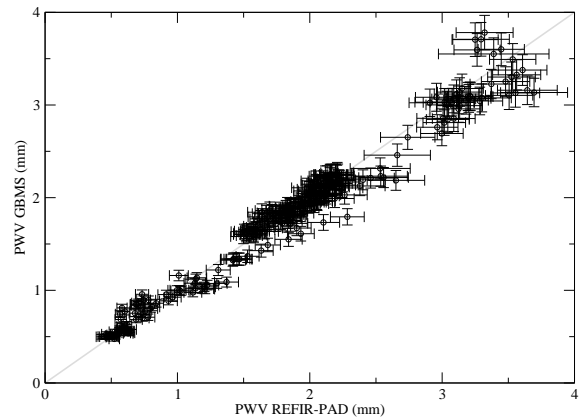


Fig. 8. PWV measured from REFIR-PAD plotted vs. PWV measurements performed in coincidence by the GBMS radiometer.

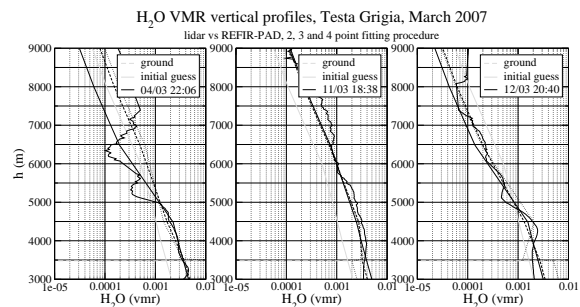


Fig. 9. Water vapor vertical VMR profiles obtained from REFIR-PAD data through the 2-points (solid line), the 3-points (dashed line) and the 4-points (dotted line) retrieval processes compared with coincident profiles measured by the BASIL lidar.

10% for particle extinction coefficient, 5% for water vapor mixing ratio and 1 K for temperature.

The horizontal distance between the REFIR-PAD and BASIL measurement sites is about 5 km , so considering that both have a vertical observation geometry, we can expect a good coincidence between the measurements.

In figure 9 is shown a comparison between three different lidar water vapor profiles acquired in different days of the campaign, and the corresponding REFIR-PAD retrieved profiles in the 2-, 3- and 4-point fit cases.

Due to the low vertical resolution, the REFIR-PAD retrieved profile is not able to reproduce the vertical structure present in the leftmost panel, while in the case of more smooth profiles (center and right panels), the agreement is better, and can be also seen the slight improvement that is obtained using three profile points instead of two. The use of 4 fitting points does not provide sensible improvement in the agreement with lidar profiles, since the resolution increase is obtained near ground, where the REFIR-PAD measurements

are sensitive to boundary layer effects, that are not seen in the lidar sounding.

8 Conclusions

In this paper we have demonstrated the capability of the REFIR-PAD instrument to provide, besides the level 1 calibrated downwelling radiance spectra, also a wealth of atmospheric parameters that are obtained through level 2 analysis of the atmospheric radiances.

The main level 2 product is the precipitable water vapor, that is measured with a time resolution of about 15 minutes, and an accuracy between 5 and 7%.

Information about the vertical structure of water vapor and temperature is also obtained, along with cloud extinction in case of thin, high altitude clouds (cirrus).

These capabilities, along with the characteristics of ruggedness and simplicity of operation coming from the compact and uncooled design of the instrument, make REFIR-PAD an ideal tool for the continuous and possibly remote-operated monitoring of the atmosphere from high-altitude ground station.

Acknowledgements. The authors want to acknowledge Francesco Castagnoli, of IFAC-CNR for on-site technical support during the ECOWAR measurement campaign

References

- R. Bhawar, G. Bianchini, A. Bozzo, M. R. Calvello, M. Cacciani, M. Carlotti, F. Castagnoli, V. Cuomo, P. Di Girolamo, T. Di Iorio, L. Di Liberto, A. di Sarra, F. Esposito, G. Fiocco, D. Fuà, G. Grieco, T. Maestri, G. Masiello, G. Muscari, L. Palchetti, E. Papandrea, G. Pavese, R. Restieri, R. Rizzi, F. Romano, C. Serio, D. Summa, G. Todini, and E. Tosi, “Spectrally Resolved Observations of Earth’s Emission Spectrum in the H₂O Rotation Band”, *Geophys. Res. Lett.*, **35**, L04812, doi: 10.1029/2007GL032207 (2008).
- G. Bianchini, L. Palchetti, B. Carli, “A wide-band nadir-sounding spectroradiometer for the characterization of the Earth’s outgoing long-wave radiation”, *Sensors, Systems and Next-generation Satellites XII*, edited by R. Meynart, S. P. Neeck, H. Shimoda, Proceedings of the SPIE, **6361**, 63610A (2006).
- G. Bianchini, L. Palchetti, A. Baglioni, F. Castagnoli, “Far-infrared spectrally resolved broadband emission of the atmosphere from Morello and Gomito mountains near Florence”, *Remote Sensing of Clouds and the Atmosphere XII*, edited by A. Comerón, K. Schäfer, J. R. Slusser, R. H. Picard, A. Amodeo, Proceedings of the SPIE, **6745**, 674518 (2007).
- G. Bianchini and L. Palchetti, “Technical Note: REFIR-PAD level 1 data analysis and performance characterization”, *Atmos. Chem. Phys.*, **8**, 3817–3826 (2008).
- S.A. Clough, M.J. Iacono, and J.L. Moncet, “Line-by-line calculations of atmospheric fluxes and cooling rates: Application to water vapor”, *J. Geophys. Res.*, **97**, 15761–15785, (1992).
- S. A. Clough, M. W. Shephard, E. J. Mlawer, J. S. Delamere, M. J. Iacono, K. Cady-Pereira, S. Boukabara, and P. D. Brown, “Atmospheric radiative transfer modeling: a summary of the AER codes, Short Communication”, *J. Quant. Spectrosc. Ra.*, **91**, 233–244 (2005).
- R. L. de Zafra, A. Parrish, P. M. Solomon, and J. W. Barrett, “A quasi continuous record of atmospheric opacity at $\lambda = 1.1$ mm over 34 days at Mauna Kea observatory”, *Int. J. Infrared Millimeter Waves*, **4**, 757–765 (1983).
- P. Di Girolamo, R. Marchese, D. N. Whiteman, and B. B. Demoz, “Rotational Raman Lidar measurements of atmospheric temperature in the UV”, *Geophys. Res. Lett.*, **31**, L01106, doi:10.1029/2003GL018342 (2004).
- M.G. Divakarla, C.D. Barnet, M.D. Goldberg, L.M. McMillin, E. Maddy, W. Wolf, L. Zhou, and X. Liu, “Validation of Atmospheric Infrared Sounder temperature and water vapor retrievals with matched radiosonde measurements and forecasts”, *J. Geophys. Res.*, **111**, D09S15 (2006)
- W.P. Elliott, and D.J. Gaffen, “On the Utility of Radiosonde Humidity Archives for Climate Studies”, *Bull. Amer. Meteor. Soc.*, **72**, 1507–1520 (1991).
- M.N. England, R.A. Ferrare, S.H. Melfi, D.N. Whiteman, and T.A. Clark, “Atmospheric Water Vapor Measurements: Comparison of Microwave Radiometry and Lidar”, *J. Geophys. Res.*, **97(D1)**, 899–916 (1992).
- I. Fiorucci, G. Muscari, C. Bianchi, P. Di Girolamo, F. Esposito, G. Grieco, D. Summa, G. Bianchini, L. Palchetti, M. Cacciani, T. Di Iorio, G. Pavese, D. Cimini, R.L. de Zafra, “Measurements of low amounts of precipitable water vapor by millimeter wave spectroscopy: An intercomparison with radiosonde, Raman lidar, and Fourier transform infrared data”, *J. Geophys. Res.*, **113**, doi: 10.1029/2008jd009831 (2008).
- I. E. Gordon, L. S. Rothman, R. R. Gamache, D. Jacquemart, C. Boone, P. F. Bernath, M. W. Shephard, J. S. Delamere, and S. A. Clough, “Current updates of the water-vapor line list in HITRAN: A new Dietfor air-broadened half-widths”, *J. Quant. Spectrosc. Ra.*, **108**, 389–402, doi:10.1016/j.jqsrt.2007.06.009 (2007).
- J.T. Kiehl and K.E. Trenberth, “Earth’s Annual Global Mean Energy Budget”, *B. Am. Meteor. Soc.*, **78**, 197–208, (1997).
- F. X. Kneizys, E. P. Shettle, W. O. Gallery, J. H. Chetwynd, Jr., L. W. Abreu, J. E. A. Selby, R. W. Fenn, and R. A. McClatchey, “Atmospheric Transmittance/Radiance: Computer Code LOWTRAN 5”, *Environmental Research Papers no. 697, AFGL-TR-80-0067*, Air Force Geophysics Laboratory (1980).
- L.M. Miloshevich, A. Paukkunen, H. Vömel, and S.J. Oltmans, “Development and Validation of a Time-Lag Correction for Vaisala Radiosonde Humidity Measurements”, *J. Atmos. Oceanic Technol.*, **21**, 1305–1327 (2004).
- E. J. Mlawer, D. C. Tobin, and S. A. Clough, “A Revised Perspective on the Water Vapor Continuum: The MT-CKD Model”, *J. Quant. Spectrosc. Ra.*, in preparation (2009).
- F. Niro, K. Jucks, and J.-M. Hartmann, “Spectral calculations in central and wing regions of CO₂ IR bands, IV: Software and database for the computation of atmospheric spectra”, *J. Quant. Spectrosc. Ra.*, **95**, 469–481 (2005).
- L. Palchetti, A. Barbis, J. E. Harries, D. Lastrucci, “Design and mathematical modelling of the space-borne far-infrared Fourier transform spectrometer for REFIR experiment”, *Infr. Phys. & Tech.*, **40**, 367–377 (1999).
- L. Palchetti, C. Belotti, G. Bianchini, F. Castagnoli, B. Carli, U.

- Cortesi, M. Pellegrini, C. Camy-Peyret, P. Jeseck, and Y. Té, “Technical note: First spectral measurement of the Earth’s upwelling emission using an uncooled wideband Fourier transform spectrometer”, *Atmos. Chem. Phys.*, **6**, 5025–5030 (2006).
- L. Palchetti, G. Bianchini, B. Carli, U. Cortesi, and S. Del Bianco, “Measurement of the water vapour vertical profile and of the Earth’s outgoing far infrared flux”, *Atmos. Chem. Phys. Discuss.*, **7**, 17741–17767 (2007).
- R. Rizzi, B. Carli, J. E. Harries, J. Leotin, C. Serio, A. Suter, B. Bizzarri, R. Bonsignori, and S. Peskett, “Mission objectives and instrument requirements for the (REFIR) Radiation Explorer in the Far-Infrared mission: an outline after the end of phase B0”, in *Current Problems in Atmospheric Radiation*, W. L. Smith and Y. M. Timofeyev, eds., Proc. of Int. Radiation Symp. (IRS) 2000, pp. 567–570 (2001).
- L. S. Rothman, D. Jacquemart, A. Barbe, C. D. Benner, M. Birk, L. R. Brown, M. R. Carleer, C. Chackerian, K. Chance, L. H. Coudert, V. Dana, V. M. Devi, J.-M. Flaud, R. R. Gamache, A. Goldman, J.-M. Hartmann, K. W. Jucks, A. G. Maki, J.-Y. Mandin, S. T. Massie, J. Orphal, A. Perrin, C. P. Rinsland, M. A. H. Smith, J. Tennyson, R. N. Tolchenov, R. A. Toth, J. Vander Auwera, P. Varanasi, and G. Wagner, “The HITRAN 2004 molecular spectroscopic database”, *J. Quant. Spectrosc. Ra.*, **96**, 139–204 (2005).
- C. Serio, F. Esposito, G. Masiello, G. Pavese, M. R. Calvello, G. Grieco, V. Cuomo, H. L. Buijs, and C. B. Roy, “Interferometer for ground-based observations of emitted spectral radiance from the troposphere: evaluation and retrieval performance”, *Appl. Opt.*, **47**, 3909–3919 (2008).
- M. W. Shephard, S. A. Clough, V. H. Payne, W. L. Smith, S. Kireev, and K. E. Cady-Pereira, “Performance of the line-by-line radiative transfer model (LBLRTM) for temperature and species retrievals: IASI case studies from JAIVEx”, *Atmos. Chem. Phys.*, **9**, 7397–7417 (2009).
- A. Sinha and J. E. Harries, “Water vapour and greenhouse trapping: The role of far infrared absorption”, *Geoph. Res. Lett.*, **22**, 2147–2150 (1995).
- H. Vömel, H. Selkirk, L. Miloshevich, J. Valverde-Canossa, J. Valdés, E. Kyrö, R. Kivi, W. Stolz, G. Peng, and J.A. Diaz, “Radiation Dry Bias of the Vaisala RS92 Humidity Sensor”, *J. Atmos. Oceanic Technol.*, **24**, 953–963 (2007).

Bibliography

Austin, J., R.R. Garcia, J. M. III Russel, S. Solomon, and A. F. Tuck, *On the atmospheric photo-chemistry of nitric acid*, J. Geophys. Res., 91, 5477–5484, 1986.

Bekki, S., M.P. Chipperfield, J.A. Pyle, J.J. Remedios, S.E. Smith, R.G. Grainger, A. Lambert, J.B. Kumer, J.L. Mergenthaler, *Coupled aerosol-chemical modeling of UARS HNO₃ and N₂O₅ measurements in the Arctic upper stratosphere*, J. Geophys. Res., 102, 8977–8984, 1996.

Bhawar, R., G. Bianchini, A. Bozzo, M. Cacciani, M.R. Calvello, M. Carlotti, F. Castagnoli, V. Cuomo, P. Di Girolamo, T. Di Iorio, L. Di Liberto, A. di Sarra, F. Esposito, G. Fiocco, D. Fuà, G. Grieco, T. Maestri, G. Masiello, G. Muscari, L. Palchetti, E. Papandrea, G. Pavese, R. Restieri, R. Rizzi, F. Romano, C. Serio, D. Summa, G. Todini, E. Tosi, *Spectrally resolved observations of atmospheric emitted radiance in the H₂O rotation band*, Geophys. Res. Lett., 35, L04812, doi:10.1029/2007GL032207, 2008

Bianchini, G., L. Palchetti, and B. Carli, *A wide-band nadir-sounding spectroradiometer for the characterization of the Earth's outgoing long-wave radiation*, Proc. SPIE Int. Soc. Opt. Eng., 6361, 63610A, 2006

Bianchini, G., L. Palchetti, G. Muscari, I. Fiorucci, P. Di Girolamo, and T. Di Iorio, *Water vapor sounding with the far infrared REFIR-PAD spectroradiometer from a high-altitude ground-based station during the ECOWAR campaign*, submitted to Atmos. Chem. Phys, 2010.

Brasseur G., and S. Solomon, *Aeronomy of the middle atmosphere*, D. Reidel, Dordrecht, Holland, 1984.

Brasseur, G., J. Orlando, and G. Tyndall, *Atmospheric Chemistry and Global Change*, Oxford University Press, New York, Oxford, 2nd ed., ISBN-0-19-510521-4, 1999.

Buehler S.A., P. Eriksson, T. Kuhna, A. von Engelna, C. Verdesa, *ARTS, the atmospheric radiative transfer simulator*, Journal of Quantitative Spectroscopy & Radiative Transfer, 91 65–93, 2005.

Callis, L. B., and J. D. Lambeth, *NO_y formed by precipitating electron events in*

1991 and 1992: Descent into the stratosphere as observed by ISAMS, *Geophys. Res. Lett.*, 25, 1875–1878, 1998.

Chandrasekhar, S., *Radiative transfer*, Dover publications, New York, 1960.

Coe H., B.J. Allan and J. M. C. Plane, *Retrieval of vertical profiles of NO₃ from zenith sky measurements using an optimal estimation method*, *J. Geophys. Res.*, 107 (D21), 4587, doi:10.1029/2002JD002111, 2002.

Connor B. J., A. Parrish, J.-J. Tsou, and M. P. McCormick, *Error analysis for the ground-based microwave ozone measurements during STOIC*, *J. Geophys. Res.*, 100 (D5), 9283–9291, 1995.

Corradini S., M. Cervino, *Aerosol extinction coefficient profile retrieval in the oxygen A-band considering multiple scattering atmosphere. Test case: SCIAMACHY nadir simulated measurements*, *Journal of Quantitative Spectroscopy & Radiative Transfer*, 97 354-380, 2006.

Dessler, A.: *The Chemistry and Physics of Stratospheric Ozone*, International Geophysics Series, Academic Press, Cornwall, IX, 214 pp., UK, 2000.

de Zafra, R. L., *The ground-based measurements of stratospheric trace gases using quantitative millimeter wave emission spectroscopy*, in *Diagnostic tools in atmospheric physics*, Proceedings of the international school of physics “Enrico Fermi”, pp. 23-54, Società italiana di fisica, Bologna, 1995.

de Zafra, R. L., V. Chan, S. Crewell, C. Trimble, and J. M. Reeves, *Millimeter wave spectroscopic measurements over the South Pole: 3. The behavior of stratospheric nitric acid through polar fall, winter, and spring*, *J. Geophys. Res.*, 102, 1399–1410, 1997.

de Zafra, R. L., and S. P. Smyshlyaev, *On the formation of HNO₃ in the Antarctic mid-to-upper stratosphere in winter*, *J. Geophys. Res.*, 106, 23,115–23,125, 2001.

de Zafra, R. L., and G. Muscari, *CO as an high-altitude tracer of dynamics in the polar stratosphere and mesosphere*, *J. Geophys. Res.*, 109 (D06105), doi:10.1029/2003JD004099, 2004.

Di Biagio C., G. Muscari, A.G. di Sarra, I. Fiorucci, R.L. de Zafra, M. Cacciani, P. Eriksen, and D. Fuà, *the 2009 major stratospheric warming observed by lidar and millimeter-wave spectrometer at Thule (76.5° N, 68.8° W)*, submitted to *J. Geophys. Res.*, 2010.

Di Girolamo, P., R. Marchese, D. N. Whiteman, and B. B. Demoz , *Rotational Raman lidar measurements of atmospheric temperature in the UV*, Geophys. Res. Lett., 31, L01106, doi:10.1029/2003GL018342, 2004

Eriksson P., C. Jiménez, S. A. Buehler, *Qpack, a general tool for instrument simulation and retrieval work*, Journal of Quantitative Spectroscopy & Radiative Transfer, 91 47-64, 2005.

Fiorucci I., G. Muscari, C. Bianchi, P. Di Girolamo, F. Esposito, G. Grieco, D. Summa, G. Bianchini, L. Palchetti, M. Cacciani, T. Di Iorio, G. Pavese, D. Cimini, and R. L. de Zafra , *Measurements of low amounts of precipitable water vapor by mm-wave spectroscopy: an intercomparison with radiosonde, Raman Lidar and FTIR data*, Journal of Geophysical Research, 113, D14314, doi:10.1029/2008JD009831, 2008.

Fiorucci I., G. Muscari, C. Bianchi, P. Di Girolamo, F. Esposito, G. Grieco, D. Summa, G. Bianchini, L. Palchetti, M. Cacciani, T. Di Iorio, G. Pavese, D. Cimini, and R. L. de Zafra, *An intercomparison of precipitable water vapor measurements obtained during the ECOWAR field campaign*, Proceedings of the International Radiation Symposium (IRC/IAMAS), vol.1100, pp.135-138, doi:10.1063/1.3116932, 2009.

Garcia, R. R., and S. Solomon, *A new numerical model of the middle atmosphere, 2, Ozone and related species*, J. Geophys. Res., 99, 12,937– 12,951, 1994.

Gille, J. C., and J. M. Russell, *The Limb Infrared Monitor of the Stratosphere: Experiment description, performance, and results*, J. Geophys. Res., 89, 5125– 5140, 1984.

Gille J. C., J.M. Russell, P.L. Bailey, E.E. Remsberg, L.L. Gordley, W.F.J. Evans, H. Fischer, B.W. Gandrud, A. Girard, J.E. Harries, S.A. Beck, *Accuracy and precision of the nitric acid concentrations determined by the Limb Infrared Monitor of the Stratosphere experiment on Nimbus 7*, J. Geophys. Res., 89, 5179–5190, 1984.

Gordy, W., and R. L. Cook, *Microwave Molecular Spectra*, Wiley Interscience, New York, 1970.

Hanson D R, A. R. Ravishankara and S. Solomon *Heterogeneous nucleation of sulfuric acid aerosols A: framework or model calculation*, Geophys Res., 99, 3615-3629, 1994.

Hoogen R., V.V. Rozanov, and J. P. Burrows, *Ozone profiles from GOME satellite data: description and first validation Algorithm*, J. Geophys. Res., 104 (D7), 8263-

8280,1999.

Janssen, M.A., ed., *Atmospheric remote sensing by microwave radiometry*, John Wiley and sons, New York, 1993.

Kawa S. R., J. B. Kumer, A. R. Douglass, A. E. Roche, S. E. Smith, F. W. Taylor, and D. J. Allen, *Missing chemistry of reactive nitrogen in the upper stratospheric polar winter*, *Geophys. Res. Lett.*, 22, 2629–2632, 1995

Kondo, Y., T. Sugita, L. J. Salawitch, M. Koike, and T. Deshler *Effects of Pinatubo aerosols on atmospheric NO*, *J. Geophys Res.* 102, 1205-1213, 1997.

Kuntz M., G. Kopp, H. Berg, G. Hochschilda, and R. Krupa, *Joint retrieval of atmospheric constituent profiles from ground-based millimetre-wave measurements: C10, HNO₃, N₂O, and O₃*, *J. Geophys Res.* 104, (D11) 13,981-13,992, 1997.

Lary D.J., M. P. Chipperfield, J. A. Pyle, W. A. Norton and L. P. RiishØjgaard, *Three-dimensional tracer initialization and general diagnostics using equivalent PV latitude-potential-temperature coordinates*. *Q. J. R. Meteorol. Soc.*, 121, pp. 187-210, 1995.

Lefèvre F., G. P. Brassour, I. Folkins, A. K. Smith, and P. Simon, *Chemistry of the 1991-1992 stratospheric winter: Three-dimensional model simulations*, *J Geophys Res.*, 99, 8183-8195,1994.

Livesey N. J., W. G. Read, L. Froidevaux, J.W. Waters, M.L. Santee, H.C. Pumphrey, D.L. Wu, Z. Shippony, and R.F. Jarnot, *the UARS Microwave Limb Sounder version 5 data set: theory, characterization, and validation*, *J. Geophys. Res.*, 119 (D13), 4378, doi:10.1029/2002JD002273, 2003.

Livesey N. J., W. V. Snyder, W. G. Read, P.A. Wagner, *Retrieval algorithms for the EOS Microwave Limb Sounder (MLS)*, *IEEE Trans. Geosci. Remote Sens.*, 44, 1144-1155, 2006.

McDonald, M., R. L. de Zafra, and G. Muscari, *Millimeter wave spectroscopic measurements over the South Pole: 5. Morphology and evolution of HNO₃ vertical distribution, 1993 versus 1995*, *J. Geophys. Res.*, 105, 17,739– 17,750, 2000.

Michelsen H. A., C.R. Webster, G.L. Manney, D.C Scott, J.J. Margitan, R.D. May, F.W. Irion, M.R. Gunson, J.M.Russell, C.M. Spivakosvsky, *Maintenance of high HCl/Cly and NOx/NOy in the Antarctic vortex: A chemical signature of confinement during spring*, *J. Geophys. Res.*, 104, 26,419– 26,436, 1999.

- Molina, L. T., and M. J. Molina, *Production of Cl₂O₂ from the self-reaction of the ClO radical*, J. Phys. Chem., 91, 433-436, 1987.
- Murcrey D.G., T.G. Kayle, F.H. Murcrey and W.J. Williams, *Nitric acid and nitric oxide in the lower stratosphere*, Nature 218 78-79, doi: 10.1038/218078a0, 1968
- Muscari, G., M. L. Santee, and R. L. de Zafra, *Intercomparison of stratospheric HNO₃ measurements over Antarctica: Ground-based millimeter-wave versus UARS/MLS version 5 retrievals*, J. Geophys. Res., 107(D24), 4809, doi:10.1029/2002JD002546, 2002.
- Muscari, G., A. G. di Sarra, R. L. de Zafra, F. Lucci, F. Baordo, F. Angelini, and G. Fiocco, *Middle atmospheric O₃, CO, N₂O, HNO₃, and temperature profiles during the warm Arctic winter 2001–2002*, J. Geophys. Res., 112, (D14304), doi:10.1029/2006JD007849, 2007.
- Muscari G., C. Cesaroni, C. Bianchi, R. L. de Zafra, T. Di Iorio, I. Fiorucci, D. Fuà, V. Romaniello and E. Zuccheretti, *Millimeter wave spectroscopic measurements of stratospheric and mesospheric constituents over the Italian Alps: stratospheric ozone*, Annals of Geophysical, vol.50 N. 3, 2007.
- Nagahama T., H. Nakane, Y. Fujinuma, M. Ninomiya, H. Ogawa, and Y. Fukui, *Ground-based millimeter-wave observations of ozone in the upper stratosphere and mesosphere over Tsukuba*, Earth Planets Space, 51, 1287–1296, 1999.
- Natarajan, M., E.E. Remsberg, L.E. Deaver, J.M. Russell, *Anomalous high levels of NO_x in the polar upper stratosphere during April, 2004: Photochemical consistency of HALOE observations*, Geophys. Res. Lett., 31, L15113, doi:10.1029/2004GL020566, 2004.
- Newman, P. A., E. R. Nash, S. R. Kawa, S. A. Montzka, and S. M. Schauffler, *When will the Antarctic ozone hole recover?*, Geophys. Res. Lett., 33, L12814, doi:10.1029/2005GL025232, 2006.
- Orsolini Y. J., G. L. Manney, M. L. Santee, and C. E. Randall, *An upper stratospheric layer of enhanced HNO₃ following exceptional solar storms*, Geophys. Res. Lett., 32, L12S01, doi:10.1029/2004GL021588, 2005
- Parrish A., B.J. Connor, J.J. Tsou, I.S. Mc Dermid and W.P. Chu, *Ground-Based Microwave Monitoring of Stratospheric Ozone*, J. Geophys. Res., 97, (D2), 2541-2546, 1992.

Parrish, A., R.L. de Zafra, P.M. Solomon, and J.W. Barrett, *A ground-based technique for millimeter wave spectroscopic observations of stratospheric trace constituents*, Radio Sci., 23(2), 106-118, 1988.

Petkie, D. T., P. Helminger, R. A. Butler, S. Albert, and D. L. F. C., *The millimeter and submillimeter spectra of the ground and excited ν_9 , ν_8 , ν_7 and ν_6 vibrational states of HNO_3* , J. Mol. Spectrosc., 218, 127–130, 2003.

Randall, C. E., D. E. Siskind, and R. M. Bevilacqua, *Stratospheric NO_x enhancements in the southern hemisphere vortex in winter/spring of 2000*, Geophys. Res. Lett., 28, 2385–2388, 2001.

Rodgers, C.D., *Retrieval of atmospheric temperature and composition from remote measurements of thermal radiation*, Rev. Geophys. and Space Phys. 14 (4), 609-624, 1976.

Rodgers, C. D., *Characterization and error analysis of profiles retrieved from remote sounding measurements*, J. Geophys. Res., 95, 5587-5595, 1990.

Rodgers, C. D., *Inverse method for atmospheric sounding*, New York: World Scientific Publishing Pte LTd, 2000.

Rodriguez J. M., M. K. W. Ko, and N. D. Sze, *Role of heterogeneous conversion of N_2O_5 on sulphate aerosols in global ozone losses*, Nature, 352, 134-137, 1991.

Rothman L.S., et al., *The HITRAN 2008 molecular spectroscopic database*, Journal of Quantitative Spectroscopy and Radiative Transfer, 110 (9-10), pp. 533-572, 2009.

Rowe, P. M., L. M. Miloshevich, D. D. Turner, and V. P. Walden, *Dry bias in Vaisala RS90 radiosonde humidity profiles over Antarctica*, J. Atm. Oceanic Technol., doi:10.1175/2008JTECHA1009.1, 2008

Santee, M. L., A. Tabazadeh, G. L. Manney, R. J. Salawitch, L. Froidevaux, W. G. Read, and J. W. Waters, *UARS Microwave Limb Sounder HNO_3 observations: Implications for Antarctic polar stratospheric clouds*, J. Geophys. Res., 103, 13,285–13,313, 1998.

Santee M. L., G. L. Manney, L. Froidevaux, W. G. Read, and J. W. Waters, *Six years of UARS Microwave Limb Sounder HNO_3 observations: Seasonal, interhemispheric, and interannual variations in the lower stratosphere*, J. Geophys. Res., 104, (D7) 8225–8246, 1999.

Santee, M., G. Manney, N. Livesey, and W. Read, *Three-dimensional structure and*

evolution of HNO₃ based on UARS Microwave Limb Sounder measurements, J. Geophys. Res., 109, D15306, doi:10.1029/2004JD004578, 2004.

Santee, M., A. Lambert, W. Read, N. Livesey, R. Coeld, D. Cuddy, W. Daffer, B. Drouin, L. Froidevaux, R. Fuller, R. Jarnot, B. Knosp, G. Manney, V. Perun, W. Snyder, P. Stek, R. Thurstans, P. Wagner, J. Waters, G. Muscari, R. de Zafra, J. Dibb, D. Fahey, P. Popp, T. Marcy, K. Jucks G. Toon, R. Stachnik, P. Bernath, C. Boone, K. Walker, J. Urban, and D. Murtagh, *Validation of the Aura Microwave Limb Sounder HNO₃ Measurements*, J. Geophys. Res., 112, D24S40, doi:10.1029/2007JD008721, 2007.

Siskind, D. E., G. E. Nedoluha, C. E. Randall, M. Fromm, and J. M. Russell III, *An assessment of Southern Hemisphere stratospheric NO_x enhancements due to transport from the upper atmosphere*, Geophys. Res. Lett., 27, 329–332, 2000.

Schneider, J., F. Arnold, J. Curtius, B. Sierau, H. Fischer, P. Hoor, F.G. Wienhold, U. Parchatka, Y.C. Zhang, H. Schlager, H. Ziereis, C. Feigl, J. Lelieveld, H.A. Scheeren, O. Bujok, *the temporal evolution of the ratio HNO/NO in the Arctic lower stratosphere from January to March 1997*, Geophys. Res. Lett., 26, 1125–1128, 1999.

Schoeberl M.R., L.C. Sparling, *Trajectory model in Diagnostic Tools in Atmospheric Physics: Enrico Fermi Course CXVI*, edited by G. Fiocco and G. Visconti, pp.289-305, North-Holland, New York, 1995.

Schoeberl M.R., A.R. Douglass, E. Hilsenrath, P.K. Barthia, R. Beer, J.W. Waters, M.R. Gunson, L. Froidevaux, J.C. Gille, J.J. Barnett, P.F. Levelt, P. DeCola, *Overview of the EOS Aura Mission*, IEEE Trans. Geosci. Remote Sens., 44, 1066-1074, 2006b.

Solomon, S., P. J. Crutzen, and R. G. Roble, *Photochemical coupling between the thermosphere and the lower atmosphere: 1. Odd nitrogen from 50 to 120 km*, J. Geophys. Res., 87, 7206–7220, 1982.

Solomon, S., R.W. Portmann, R.W. Sanders, J.S. Daniel, W. Madsen, B. Bartram, E.G. Dutton, *On the role of nitrogen dioxide in the absorption of solar radiation*, J. Geophys. Res., 104 (D10) 12047-12058, 1999.

Solomon, S., J. Barrett, B. Connor, S. Zoonematkermani, A. Parrish, A. Lee, J. Pyle, and M. Chipperfield, *Seasonal observations of chlorine monoxide in the stratosphere over Antarctica during the 1996-1998 ozone holes and comparison with SLIMCAT three-dimensional model*, J. Geophys. Res., 105 (D23), 28,979–29,001,

2000.

Swinbank R., A. O'Neill, *A Stratosphere-troposphere data assimilation system*, Mon. Weather Rev., 122, 686-702, 1994.

Tabazadeh, A., R. P. Turco, K. Drdla, M. Z. Jacobsen, and O. B. Toon, *A study of type I polar stratospheric cloud formation*, Geophys. Res. Lett., 21, 1619-1622, 1994a.

Tabazadeh, A., R. P. Turco, and M. Z. Jacobsen, *A model for studying the composition and chemical effects of stratospheric aerosols* J. Geophys Res., 99, 12,897-12,914, 1994b.

Tabazadeh, A., O. B. Toon, and P. Hamill, *Freezing behaviour of stratospheric sulfate aerosols inferred from trajectory studies*, Geophys Res. Lett., 22, 1725-1728, 1995.

Tabazadeh, A., and O. B. Toon, *The presence of metastable HNO₃/H₂O solid phases in the stratosphere inferred from ER 2 data*, J. Geophys Res., 101,9071-9078, 1996.

Tabazadeh A, O. B. Toon, B. L. Gary, J. T. Bacmeister, and M. R. Schoeberl, *Observational constraints on the formation of type Ia polar stratospheric clouds*, Geophys Res. Lett., 23, 2109-2112, 1996.

Twomey, S., *Introduction to the Mathematics of Inversion in Remote Sensing and Indirect Measurements*, Dev. Geomathematics, vol. 3, Elsevier, New York, 1977

Twomey, S., B. Herman, and R. Rabinoff, *An extension of the Chahine method of inverting the radiative transfer equation*, J. Atmos. Sci., 34, 1085– 1090, 1977.

Urban J., M. Pommier, D. P. Murtagh, M. L. Santee, and Y. J. Orsolini *Nitric acid in the stratosphere based on Odin observations from 2001 to 2009 – Part 1: A global climatology*, Atmos. Chem. Phys., 9, 7031–7044, 2009.

WMO *Antarctic Ozone Bulletin*, 4, 2003.

WMO *Greenhouse Gas Bulletin*, 3, 2007.